GEORG-AUGUST-UNIVERSITÄT GÖTTINGEN

II. Physikalisches Institut

Measurement of the Top Quark Mass in the $\mu\mu$ and $e\mu$ Channel via the Neutrino Weighting Method using Data taken with the DØ Detector

von

Isa Heinze

In this thesis a measurement of the top quark mass in the dimuon channel and the electron-muon ($e\mu$) channel is presented with a dataset of about 1216 pb^{-1} (dimuon channel) and about 1780 pb^{-1} ($e\mu$ channel). The data were taken with the DØ detector at Fermilab in Chicago in proton-antiproton collisions at a center-of-mass energy of $\sqrt{s} = 1.96$ TeV. For the mass measurement the neutrino weighting method was used. The result is:

$$m_{top,RunIIb,combined}^{corrected} = 187.3 \pm 7.3 \text{ GeV}$$

Post address:
Friedrich-Hund-Platz 1
37077 Göttingen
Germany

II. Physikalisches Institut
Georg-August-Universität Göttingen
August 2008

GEORG-AUGUST-UNIVERSITÄT

GÖTTINGEN

II. Physikalisches Institut

Measurement of the Top Quark Mass in the $\mu\mu$ and $e\mu$ Channel via the Neutrino Weighting Method using Data taken with the DØ Detector

von

Isa Heinze

Dieser Forschungsbericht wurde als Diplomarbeit von der Fakultät für Physik der Georg-August-Universität zu Göttingen angenommen.

Angenommen am:	29. August 2008
Referent:	Prof. Quadt
Korreferent:	Prof. Klute

Contents

1. Introduction

The idea of the whole world being built from indivisible particles is old. Already the ancient Greek philosophers introduced this concept. One of the most famous ones was Democritus who first introduced the word *atomos* which is Greek and means uncutable or indivisible. The word *atom* has its origin in this word. First, this theory was a purely philosophical one. It took hundreds of years until it was proven scientifically that matter consists of discrete units and the atom was discovered, which first was thought to be the discrete unit of matter people were looking for. Since J.J. Thompson's cathode ray experiments it is known that this is not true, that there is a subatomic structure. The atom consists of electrons and a nucleus (which was discovered by Rutherford) which, as is known today, consists of protons and neutrons. Protons and neutrons again consist of quarks and gluons. As far as it is known today, quarks and electrons have no internal structure and are therefore somehow these indivisible particles the Greek philosophers had in mind.

These particles along with leptons and gauge bosons are predicted and described in the standard model of elementary particle physics. This is a very precise theory and describes the results of experiments well. However, it is not a theory describing everything. For example gravity is not included. But people are working on a theory which unifies all four fundamental forces: the strong interaction, the weak interaction, the electromagnetic interaction and gravity.

The standard model of elementary particle physics predicts the so called Higgs boson which has not yet been found. But a lot of effort is put into proving the existence of the Higgs boson, the last particle predicted by the standard model which has not been found yet. To get constraints on the mass of the Higgs boson it is important to measure the mass of the top quark as precisely as possible because the physics of these two particles is closely related.

In this thesis a top quark mass measurement in the dimuon and $e\mu$ channel is presented. For this analysis data taken with the DØ Detector at Fermilab near Chicago are used. In the second chapter a brief overview on the standard model of elementary particle physics as well as its extensions is given. Also some basic aspects of hadron collider physics are described. After that the focus is put on the production, decay and the properties of the top quark. In the third chapter Fermilab's accelerator chain and the DØ detector are described. The fourth chapter of this thesis deals with the analysis itself. It is divided into two parts. The first one deals with the dimuon selection for the dataset taken between summer 2006 and summer 2007. In the second part the mass measurement of the top quark in the dimuon channel and the $e\mu$ channel with the neutrino weighting method is presented. In the last chapter the results are summarized and an outlook is given.

2. Physics

In this chapter the standard model in general will be introduced as well as the most important possible extensions to it. After that a detailed review on the top quark, its production at hadron colliders, its decay channels and its properties will be given. In an additional section some aspects of hadron collider physics are discussed.

2.1. The Standard Model of Elementary Particle Physics

The standard model of elementary particle physics describes elementary particles and their interactions. There are six quarks that are known as well as six leptons. These particles are grouped into three families or generations [1, 2, 3, 4] (see Figure 2.1). The up (u) quark and the down quark (d) are the two lightest quarks. They build, together with the electron (e) and the electron neutrino (ν_e) the first generation. All matter surrounding us is built of particles of the first generation. Two up quarks and one down quark build a proton, one up quark and two down quarks build a neutron. Protons and neutrons built atomic nuclei and together with electrons in the shell they build atoms. The electron was the first elementary particle which was found.
In the second generation the next heavier particles can be found: the charm quark (c), the strange quark (s), the muon (μ) and the muon neutrino (ν_μ). The muon is a minimum ionizing particle which means, that it hardly interacts with matter. In nature muons are produced in the atmosphere when high-energetic protons coming from space interact with the matter in the atmosphere.
The third generation contains the heaviest particles which are known today: the top quark (t), the bottom quark (b) and as leptons the tau (τ) and the light-weight tau neutrino (ν_τ). Due to their high masses they were discovered last. The properties of the top quark are described in Section 2.2. Some basic properties of the top quark and all other elementary particles are given in Table 2.1. For each of these particles an antiparticle exists. Antiparticles have the same properties as the particle except for the inner quantum numbers which have exactly the opposite sign.
Despite the quarks and leptons the standard model also describes interactions between these particles. Each interaction has its own gauge bosons.

	Quarks			Leptons		
Generation	Name	Mass	Charge	Name	Mass	Charge
1	up	$1.3 - 3.0$ MeV	$+\frac{2}{3}e$	electron neutrino	< 460 eV	0
	down	$3 - 7$ MeV	$-\frac{1}{3}e$	electron	0.511 MeV	$1e$
2	charm	1.25 ± 0.09 GeV	$+\frac{2}{3}e$	muon neutrino	< 0.19 MeV	0
	strange	95 ± 25 MeV	$-\frac{1}{3}e$	muon	105.7 MeV	$1e$
3	top	172.4 ± 0.7 GeV	$+\frac{2}{3}e$	tau neutrino	< 18.2 MeV	0
	bottom	4.20 ± 0.07 GeV	$-\frac{1}{3}e$	tau	1776.9 ± 0.2 MeV	$1e$

Table 2.1.: Some properties of quarks and leptons [5].

The electromagnetic interaction's gauge boson is the massless photon (γ). This interaction has an influence on charged particles only. The weak interaction, which is responsible for the β-decay has three massive gauge bosons: W^+, W^- and Z. The gauge bosons for the strong interaction are the massless gluons (g). This force holds together the quarks in hadrons. Gravity is not included in the standard model but the influence on elementary particles is low due to their low mass.

While leptons can exist freely this is not possible for quarks. For this reason the color charge was introduced [1]. Possible color charges are red, blue and green. Only particles with a white color can exist unbound. There are two possibilities how to realize this. Either three quarks build a bound state (baryons) such that each color charge appears once. This gives a white color. Or a quark and an antiquark build a bound state (mesons) where the quark carries a color and the antiquark the corresponding anticolor, which gives a white color again. The gluons carry both, a color and an anticolor at the same time.

The last particle predicted by the standard model is the Higgs boson [6, 7]. Originally the standard model did not describe the masses of the gauge bosons. To solve this the Higgs field was introduced. Particles interact with the Higgs field which produces the mass. The Higgs boson is the only particle predicted by the standard model which has not been discovered yet.

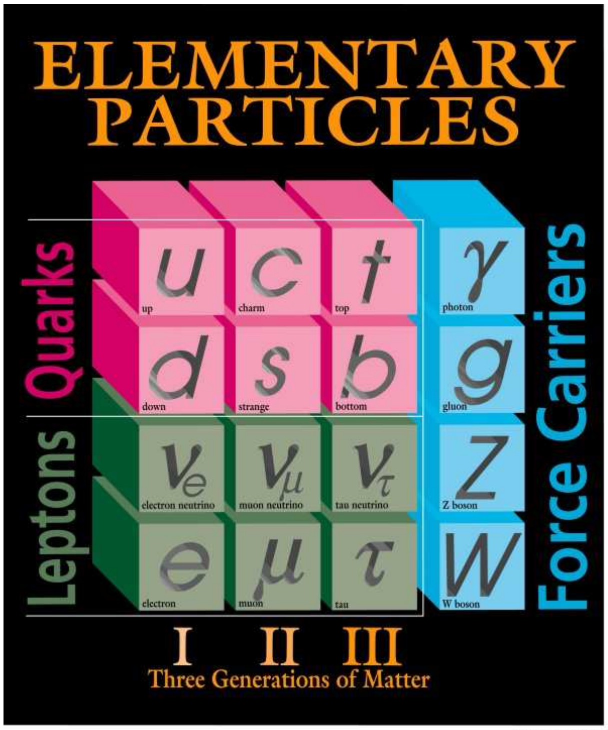

Fermilab 95-759

Figure 2.1.: Overview over particles described in the standard model.

Although the standard model describes results from experiments well it has limitations. A variety of theories beyond the standard model were developed. One of these theories is the supersymmetry [8]. Supersymmetry describes a symmetry between fermions and bosons. Every fermion has a boson as a supersymmetric partner and every boson has a fermion as a supersymmetric partner. There has not been any evidence for supersymmetry yet which leads to the conclusion that the supersymmetric partners (if they exist) are heavy. If their masses were of the same order as the masses of the particles they would have been discovered already.

Supersymmetry can for example unify the gauge couplings, solve the hierarchy problem and also supersymmetric particles are candidates for dark matter which is expected to be in the universe [9].

A big goal of particle physics is to find a theory of everything in which all four fundamental forces (strong interaction, weak interaction, electromagnetic interaction, and gravity) are unified. The electromagnetic interaction is already a unification of the electric interaction and the magnetic interaction. The unified force of electromagnetic and weak interaction is called electroweak force. A theory in which the unification of the electroweak and strong force is described is called "Grand Unified Theory" (GUT), but it has not been found yet.

The unifications, except the one of electric and magnetic force (which takes place at low energies), take place at high energies as can be seen in Figure 2.2.

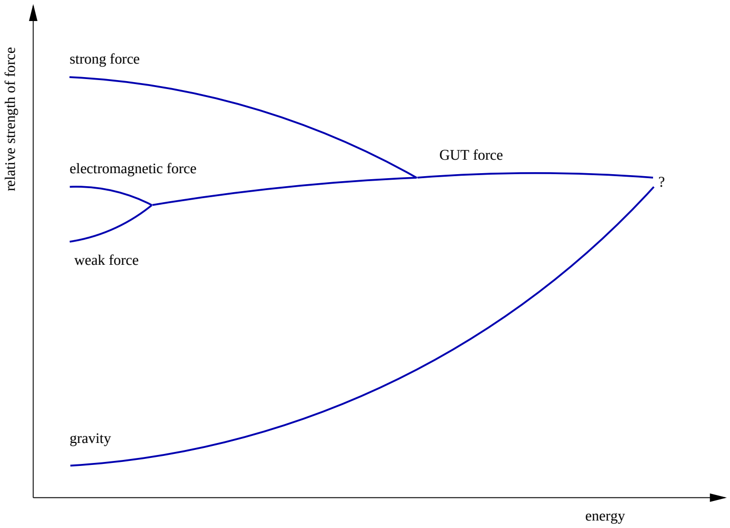

Figure 2.2.: Unification of forces.

2.2. The Top Quark: Production, Decay, and Properties

The top quark, discovered in 1995 [10, 11], is the elementary particle with the highest mass, which is known today. Currently the world average of the top quark mass[1] is [12] (see Figure 2.3)

$$m_{top} = 172.4 \pm 0.7 \text{ (stat.)} \pm 1.0 \text{ (syst.) GeV.} \tag{2.1}$$

Due to its high mass it was the last quark that was discovered.

At Fermilab's Tevatron top-antitop ($t\bar{t}$) pair production is dominant. $t\bar{t}$ can be produced either via quark-antiquark ($q\bar{q}$) annihilation or via gluon fusion. Which production channel is dominant depends on the energy of the colliding particles. At the Tevatron the $q\bar{q}$ annihilation is the dominant channel (85%) [13]. At the Large Hadron Collider (LHC) at CERN in Geneva most $t\bar{t}$ pairs will be produced via gluon fusion. The leading order Feynman graphs for the production channels are displayed in Figure 2.4. The theoretical prediction of the production cross section at next-to-leading order and at a center-of-mass energy of 1.96 TeV for a top quark mass of 175 GeV is [14]

$$\sigma_{theo} = 6.77 \pm 0.42 \text{ pb.} \tag{2.2}$$

---

[1] $\hbar = c = 1$

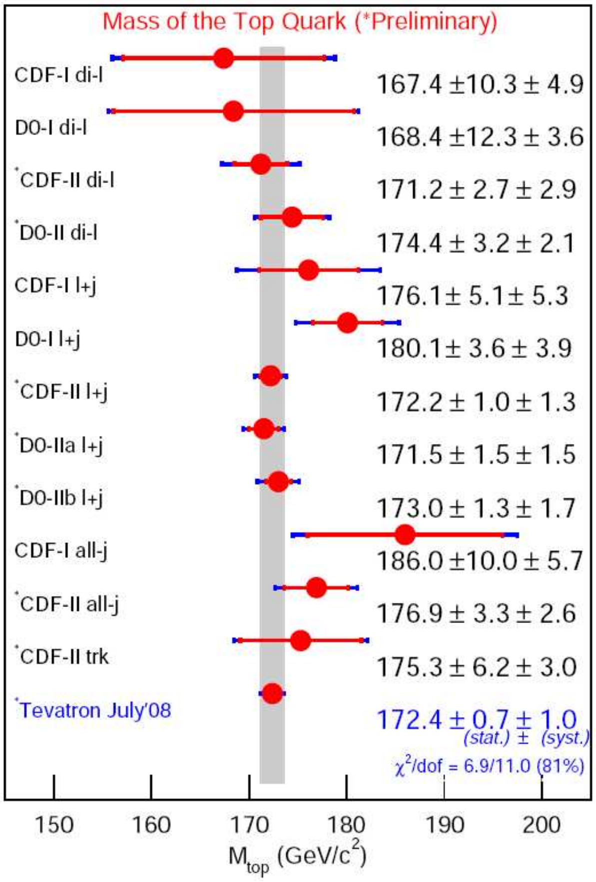

Figure 2.3.: Combination of all top quark mass measurements. In the last line the world average is given [12].

The most precise DØ measurement [15] gives a value of

$$\sigma_{measured} = 7.42 \pm 0.53 \text{ (stat.)} \pm 0.46 \text{ (syst.)} \pm 0.45\text{(lumi.) pb} \tag{2.3}$$

for a top quark mass of $m_{top} = 175$ GeV, which shows a good agreement with the theoretical value. Top quarks can not only be produced in pairs via the strong interaction but also as single top quarks via the weak interaction [16]. However, there has not yet been a discovery of single top quark production, but evidence has been found [17]. The leading order Feynman graphs for single top quark production can be found in Figure 2.5.

The theoretically predicted cross section for single top quark production at a center-of-mass energy of 1.96 TeV for a top quark mass of $m_{top} = 175$ GeV is smaller than for top quark pair production. However, the order of magnitude is the same for top quark pair production an single top quark production. From this one can conclude that the strong interaction and the weak interaction are of the same order of magnitude as well. The theoretical values are [18]

$$\begin{aligned} \sigma_{theo}^{t-channel} &= 1.08 \pm 0.06 \text{ pb} \\ \sigma_{theo}^{s-channel} &= 0.49 \pm 0.02 \text{ pb} \\ \sigma_{theo}^{Wt-channel} &= 0.13 \pm 0.03 \text{ pb} \end{aligned} \tag{2.4}$$

The measured value is [17]

$$\sigma_{measured} = 4.7 \pm 1.3 \text{ pb.} \tag{2.5}$$

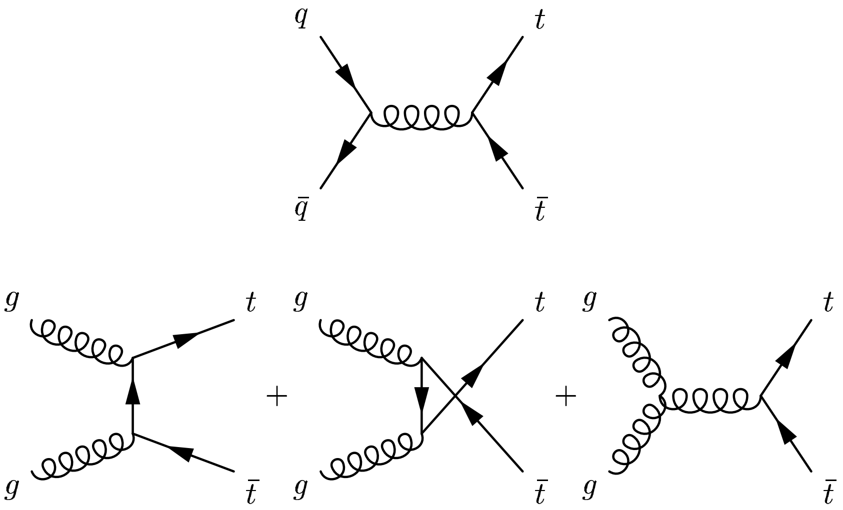

Figure 2.4.: Production channels of top-antitop pairs. Top: $q\bar{q}$ annihilation. Bottom: gluon fusion

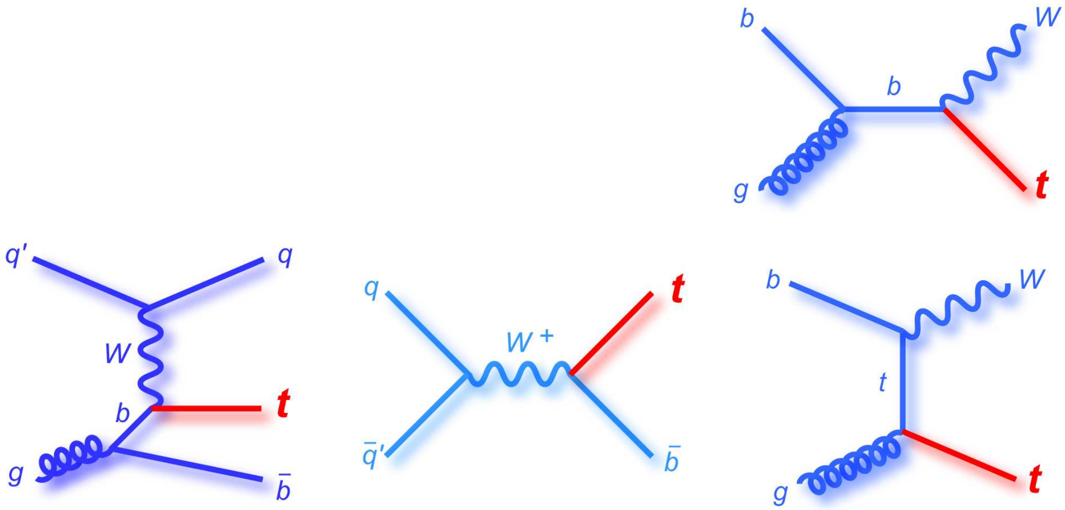

Figure 2.5.: Feynman graphs for single top quark production. Left: t-channel, middle: s-channel, right: Wt-channel.

Only the t-channel and the s-channel were used. This is in agreement with the theoretical value. Due to its high mass the top quark has a short life time of about $0.5 \cdot 10^{-25}$ sec [13]. It decays before hadrons containing top quarks can be built. This gives a unique opportunity to study quarks which are not bound to other quarks. It allows to examine quantities like the spin correlation in top quark pairs [19].

Nearly 100% of all top quarks decay into a bottom quark and a W boson. This is due the fact that the element V_{tb} of the CKM (Cabibbo-Kobayashi-Maskawa) quark mixing matrix is nearly one. In Equation 2.6 the CKM matrix is given. The values come from a global fit to the standard model using all available measurements and the assumption that there are exactly three quark generations [20].

$$
\begin{aligned}
V_{CKM} &= \begin{pmatrix} V_{ud} & V_{us} & V_{ub} \\ V_{cd} & V_{cs} & V_{cb} \\ V_{td} & V_{ts} & V_{tb} \end{pmatrix} \\
&= \begin{pmatrix} 0.97419 \pm 0.00022 & 0.2257 \pm 0.0010 & 0.00359 \pm 0.00016 \\ 0.2256 \pm 0.0010 & 0.97334 \pm 0.00023 & 0.0415^{+0.0010}_{-0.0011} \\ 0.00874^{+0.00026}_{-0.00037} & 0.0407 \pm 0.0010 & 0.999133^{+0.000044}_{-0.000043} \end{pmatrix}
\end{aligned}
\tag{2.6}
$$

The W boson decays either into two quarks or into a charged lepton and its corresponding neutrino. Regarding $t\bar{t}$ pairs this gives three different types of decay channels. In case of the all jets channel both W bosons decay into quarks which build jets in the detector. In the semileptonic channel one W boson decays into leptons the other one into quarks. Finally in the dilepton channel both W bosons decay into leptons. In Figure 2.6 the Feynman graph for the electron-muon ($e\mu$) channel is shown. In the analysis described in Section 6 only the $e\mu$ channel and the dimuon $\mu\mu$ channel are used. The ee channel is currently investigated by the DØ Top Group and not presented in this thesis.

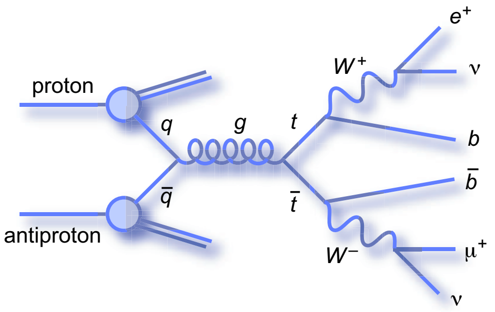

Figure 2.6.: Feynman graph for the electron-muon channel.

With simple combinatorics one can estimate how many percent of $t\bar{t}$ pairs decay in which channel at tree level. In case that both W bosons decay into an electron and an electron neutrino, there is only one possibility. In case one W boson decays into an electron and electron neutrino, the other one in a muon and muon neutrino, there are two possibilities. Either the W^+ or the W^- can decay into the muon. This gives two possibilities. The calculation is the same for the other dilepton channels. In the semileptonic channel either the W^+ or W^- decays into quarks. Now, one has to keep in mind, that the electric charge has to be the same before and after the decay. So not every combination of quarks can appear in the decay. Additionally, W bosons can not decay into top quarks and bottom quarks because they are too heavy. This leads to the following possibilities: $\overline{u}d$, $\overline{c}s$ for a charge of $-1e$ and $u\overline{d}$, $c\overline{s}$ for a charge of $+1e$. Taking this and the three possible color charges into account, there is a total of twelve combinations for semileptonic channels. Regarding the all jets channel now, there is a total of four possible quark combinations and a total of nine color combinations. This leads to $4 \times 9 = 36$ possibilities how $t\bar{t}$ pairs can decay hadronically.

As can be seen in the pie chart (Figure 2.7) most $t\bar{t}$ pairs decay in the all jets channel but only very few in the dilepton channel. However, the background in the all jets channel is high, while it is lower in the other channels. Additionally, the backgrounds of the dilepton channel are understood very well, which is an advantage of the dilepton channel over the other decay channels. The advantage of semileptonic channel is a good signal-to-background ratio. The

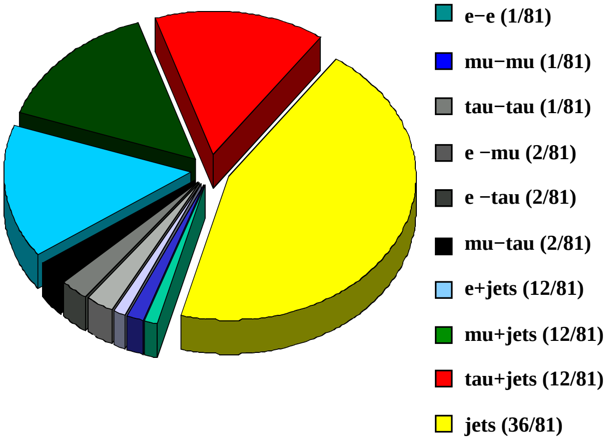

Figure 2.7.: This pie chart shows how many $t\bar{t}$ pairs decay in which channel at tree level.

main background in the dilepton channels is the $Z \to ll$ process as well as the $WW \to 2l + 2jets$ process. Additional backgrounds come from other diboson processes. A disadvantage of the dilepton channel is that in the final state two neutrinos are present. They cannot be measured in the detector. This leads to a kinematic underconstrained system. However, there are ways to deal with such systems. One of these methods, the neutrino weighting method, is the topic of this thesis. It is important to measure the top quark mass in all three channels to check that the results for all three channels are consistent. A top quark mass measurement in the $\mu\mu$ and $e\mu$ channel is presented in this thesis.

As already indicated, the physics of the Higgs boson and the top quark is closely related. In Figure 2.8 the W boson mass is plotted against the top quark mass. The green region shows where the Higgs boson was not excluded, the lines show constant Higgs boson masses. Two ellipses are shown which represent the 68% confidence level for two measurements. The first indirect measurement (dashed line) was done at LEP1 and SLD. The second one drawn with a solid line shows a measurement done with LEP2 and at the Tevatron. The ellipse with the solid line hardly touches the green region, which would mean the Higgs boson is excluded. But the ellipse shows the 1σ region only. The 2σ ellipse, which is not shown in the plot, would extend into the green region significantly.

2.3. Hadron Collider Physics

There are several possibilities which particle types can be brought to collisions in a collider. All of them have their advantages and disadvantages. For example electrons and positrons can be brought to collision, as was done at LEP at CERN. The advantage is, that in this case elementary particles are brought to collision. That means the energy of the interacting particles is known exactly. But the possible center-of-mass energies for ring colliders are restricted because the losses due to synchrotron radiation are high. Synchrotron radiation is produced when charged particles are accelerated. It is emitted tangentially to the trajectory. In ring colliders such an acceleration is performed at any time because the particles move on circular trajectories. The losses of energy due to synchrotron radiation increase with increasing energy and decreases with increasing particle masses. The energy which is lost per turn is given by

$$\Delta E \propto \left(\frac{E}{m}\right)^4 \frac{1}{R}, \tag{2.7}$$

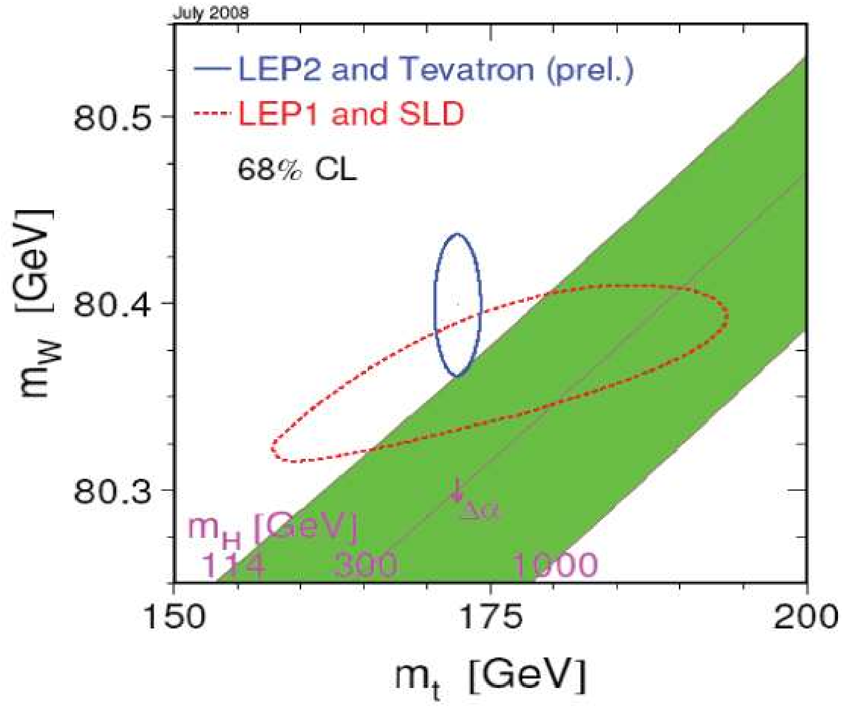

Figure 2.8.: This plot shows the W boson mass plotted against the top quark mass [21]. The lines represent constant Higgs boson masses. The ellipses show the 68% confidence level of measurements: LEP1 and SLD (dashed line), LEP2 and Tevatron (solid line).

where m is the mass of the particle, E its energy and R the radius of the circular trajectory. Electrons and positrons have a low mass, which results in high losses.
The advantage of hadrons (e.g. protons and antiprotons as used at the Tevatron) is that they have a much higher mass. That is why the losses due to synchrotron radiation are not as high in hadron colliders. This leads to much higher possible center-of-mass energies in hadron colliders. The maximum energy is limited by the magnetic fields needed to keep the particles on a circular trajectory.
A disadvantage of hadron colliders is, that hadrons are not elementary particles. They consist of gluons and quarks which interact in collisions. The initial energy of the incoming hadron is known precisely. But the energy of each parton (quark or gluon) is not known. They carry a fraction x of the proton or antiproton momentum, where x is called Bjorken x. If a proton would consist of only one quark, x would be exactly one, if it would consist of three quarks, but no gluons, the Bjorken x would be $\frac{1}{3}$. But in protons also gluons and sea quarks are present which gives a continuous distribution of x (see Figure 2.9). The center-of-mass energy of a parton interaction is then given by

$$\sqrt{s} = \sqrt{(x_1 p_1 + x_2 p_2)^2}, \tag{2.8}$$

where x_1 and x_2 denote the Bjorken x of parton 1 and 2, respectively, and p_1 and p_2 the momenta of the two partons.

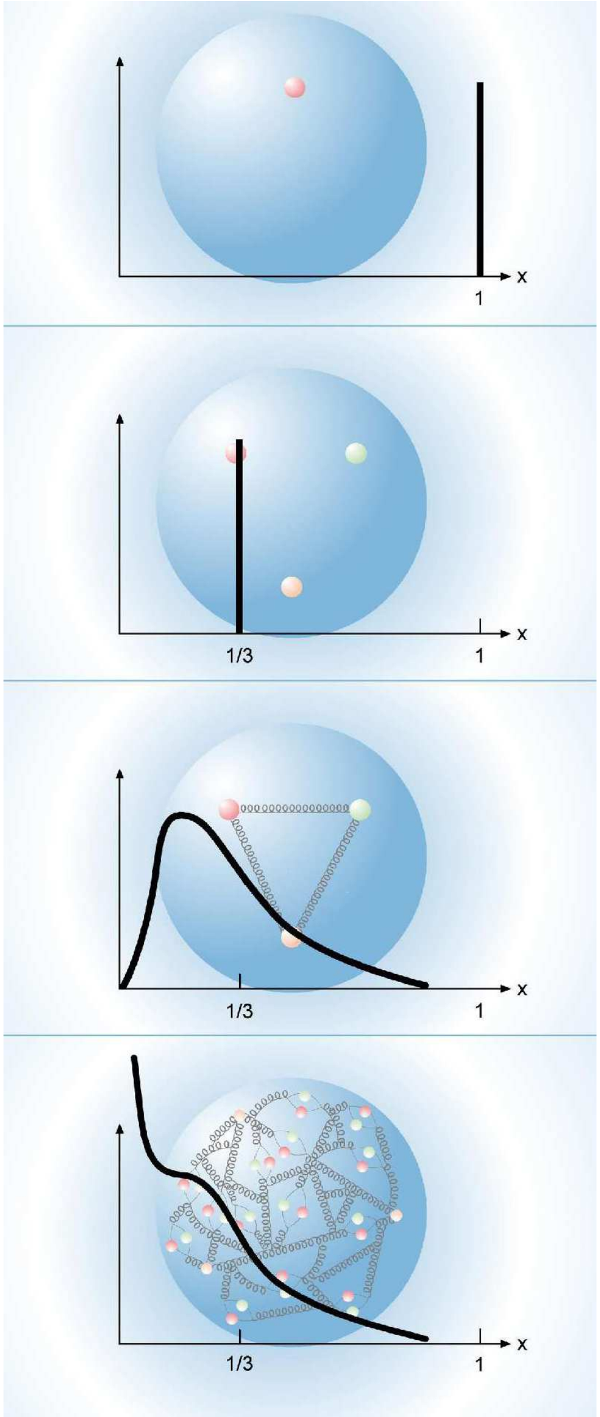

Figure 2.9.: These plots show how the distributions of the Bjorken x would look like for different models. Uppermost plot: Proton consists of exactly one quark. Second plot: Proton consists of exactly three quarks. Third plot: Proton consists of three quarks and three gluons. Lowermost plot: Sea quarks are present in the proton.

The energies of the incoming partons are not known. This problem is circumvented by introducing quantities called transverse energy (E_T) and transverse momentum (p_T) which are calculated from the components perpendicular to the beam axis. Before interaction the hadrons do not move perpendicular to the beam axis, only along the beam axis:

$$p_x = p_y = 0; p_z \neq 0.$$

The same is true for the quarks in the hadrons. So

$$p_T = \sqrt{(p_x)^2 + (p_y)^2} = 0$$

is known before the interaction. Due to momentum conservation the sum of the p_Ts of all particles in the final state must be zero as well. E_T is defined analogously. Another quantity, which is important especially in the analysis presented in this thesis, is the missing transverse energy ($\not{E}_T$). The E_T is calculated after the interaction. It is expected to be zero due to the law of conservation. If this is not the case, energy is missing. This missing fraction is called $\not{E}_T$. $\not{E}_T$ is often produced by neutrinos in the final state which cannot be seen in the detector but it can also be caused by detector resolution effects.

A variable which is going to be mentioned in this thesis several times is H_T. It is the sum of the p_T of the muon with the highest p_T and the p_T of the leading jet (jet with the highest p_T) and the next-to-leading (jet with the second highest p_T) jet, so the jets with the highest p_T and second highest p_T. If only one jet is in the event, only the p_T of this jet is added, if there is no jet at all, nothing is added.

Another important quantity in collider physics is the luminosity.

$$L = f \cdot \frac{N_1 N_2}{4\pi\sigma_x\sigma_y}, \tag{2.9}$$

where N_i is the number of particles in the two bunches crossing each other, f is the bunch crossing frequency and $\sigma_{x,y}$ gives the size of the bunches in x- and y-direction. The higher the luminosity the more interactions take place. To achieve a higher luminosity one either puts more particles in each bunch or increases the crossing rate. It is also possible to focus the beam very well so that it gets a smaller diameter which makes an interaction more likely.

3. Experimental Setup

The Fermi National Accelerator Laboratory (Fermilab) is located near Chicago. It was founded in 1967 with the original name National Accelerator Laboratory. Later in 1974 it was renamed in Enrico Fermi's honor [22, 23].

Building the Linac started in 1968 and one year later, in 1969, the Main Ring was started to be built. Three years later the first 200 GeV beam passed the Main Ring. The Tevatron (originally named Energy Doubler) started operating in 1983. In the same year they started building the Antiproton Source. The first collisions of protons and antiprotons were observed in 1985 at one of the two collider experiments: CDF (Central Detector Facility). The other collider experiment is called DØ. In Run I between 1992 and 1996 the Tevatron was operated at a center-of-mass energy of 1.8 TeV and an integrated luminosity of 125 pb^{-1} per experiment was collected. This were enough data to discover the top quark. During the shutdown after Run I the main injector was added to allow more collisions in the Tevatron. Run II started in 2001 and is still ongoing. The energy of the Tevatron was increased to 1.96 TeV. Currently an integrated luminosity of about 4 fb^{-1} has been collected in Run II. Figure 3.1 shows the development of the integrated luminosity in Run II. In this plot the shutdowns can be seen where the integrated luminosity does not rise for several months. The most important shutdown was the one in 2006 when some important detector upgrades were done. For details on the upgrades see Section 3.4. The time before this shutdown is called Run IIa. Currently Run IIb is ongoing. The data taken in Run IIa is referred to as Run IIa dataset, the dataset taken in Run IIb is called Run IIb dataset. The Run IIb datset is divided into two parts. The first part was taken before the shutdown in 2007 and therefore called Run IIb preshutdown dataset. The dataset taken after the shutdown is called Run IIb postshutdown dataset.

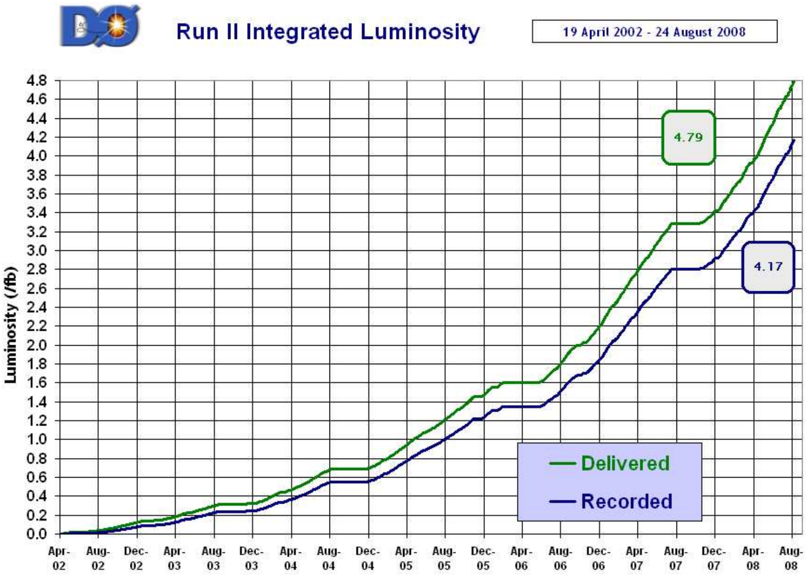

Figure 3.1.: Delivered and recorded integrated luminosity in Run II.

The Tevatron is currently the accelerator with the highest center-of-mass energy on earth which is taking data. It will carry on taking data through 2010. During these years several discoveries were made at the Tevatron such as the bottom quark (1977), the top quark (1995) and the first direct observation of the tau neutrino (2000).
However, a new accelerator, the Large Hadron Collider (LHC), which is a proton-proton collider, is built at CERN in Geneva. It will start running in September 2008. This collider has a higher center-of-mass energy of 14 TeV. The main goals for this accelerator is to find the Higgs boson and supersymmetric particles.

3.1. Fermilab's Accelerator Chain

Before colliding in the Tevatron, the protons and antiprotons pass a whole chain of accelerators which will be described in this chapter [24]. In Figure 3.2 all accelerators are depicted. The direction of motion of protons and antiprotons is indicated by black and gray arrows, respectively.

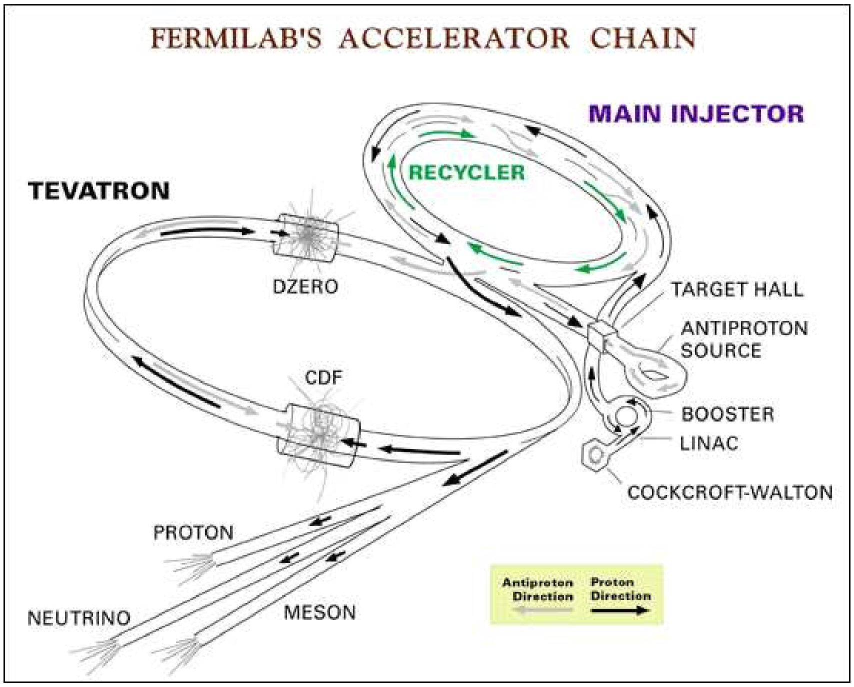

Figure 3.2.: Fermilab's accelerator chain. The direction of motion is indicated as black (protons) and gray (antiprotons) arrows.

Protons are easy to produce because they are the nuclei of hydrogen. In a first step the hydrogen is ionized (H^-) and accelerated to 750 keV in the Cockcroft-Walton preaccelerator. The acceleration is performed by a static electric field. The high voltage needed for this is produced with a Cockcroft-Walton generator.
In the linear accelerator (Linac) the energy of the ions is increased to 400 MeV. The Linac is about 150 m long. It consists of several tubes assembled in a line. Their charge is changed at a frequency so that the ions are accelerated. After that the electrons are removed by a carbon foil, so that only protons are left.
These protons are accelerated to 8 GeV in the Booster, the first circular accelerator in the chain.

The particles are kept on circular trajectories by magnets. This way they pass the electric fields for acceleration several times, which is an advantage over linear accelerators, in which each field can be passed only once. The protons pass the Booster about 20,000 times until they have the desired energy.

After that the protons are accelerated to 150 GeV in the Main Injector, which is a circular accelerator, but larger than the Booster. Besides accelerating the protons the Main Injector performs other important tasks. It produces protons with an energy of 120 GeV for the antiproton production. These protons are directed to the antiproton source which mainly consists of a nickel target. The protons produce secondary particles, antiprotons are among them. They are focused and stored in the Accumulator Ring until a sufficient number is collected. The antiprotons are then accelerated to 150 GeV in the Main Injector.

From here both protons and antiprotons are injected into the Tevatron where the collisions take place. The Tevatron is a circular accelerator of about 6.4 km circumference. After both protons and antiprotons are in the Tevatron (protons are injected first) they are accelerated to 0.98 TeV which results in a center-of-mass energy of 1.96 TeV. Finally the protons and antiprotons are brought to collision. These collisions are observed with the detectors CDF and DØ. The DØ detector is described in detail in Section 3.2.

When the antiprotons are not needed in the Tevatron, they are stored in the Recycler which is located in the same tunnel as the Main Injector until they are reinjected. This is done because antiprotons are difficult to produce and therefore precious.

The protons are not only used for the collider experiments but also for fixed target experiments and for tests in the Tevatron.

3.2. The DØ Detector in Run IIa

Detectors for collider experiments usually have a similar structure. Closest to the beam pipe and therefore closest the interaction point a vertex detector and a tracking system can be found. They have to be built from radiation hard materials. Usually silicon is used for the innermost part. This system is enclosed by a magnet. Its field forces charged particles on bent trajectories. This allows a determination of their charge and momentum. After that the electromagnetic and the hadronic calorimeter can be found. The task of the electromagnetic calorimeter is to determine the energy of electrons and photons. They interact with matter rather strongly. That is why this is done as close to the interaction point as possible. Electrons and photons deposit nearly all of their energy in the electromagnetic calorimeter, they build so-called electromagnetic showers. If an electron enters the calorimeter, it emits a photon, the photon decays into a electron-positron pair. These can emit more photons. Analog things happen when a photon hits the calorimeter. Hadrons deposit their energy in the hadronic calorimeter and build so-called hadronic showers or "jets". They are produced by inelastic hadron scattering. Mostly pions are produced, but also electromagnetic components can be found.

Beyond the calorimeters another magnet and the muon chambers can be found. Muons hardly interact with matter (so called minimum ionizing particles), so they are, next to neutrinos, the only particles that are able to leave the detector. That is why muons are measured in the outer part of the detector.

Neutrinos interact with matter even less than muons. They escape the detector without being seen. Instead missing transverse energy $\not{E}_T$ is measured (see Section 2.3).

To describe the position where a particle is observed in the detector usually the pseudorapidity

$$\eta = -\ln\left(\tan\left(\frac{\theta}{2}\right)\right) \tag{3.1}$$

is used, where θ is the angle between the beam axis and the trajectory of the particle. Regions with small $|\eta|$ are called central regions, regions with large $|\eta|$ are called forward regions.
As a second variable the angle φ is used. This is started counting at one side of the detector, then going up, going down on the other side and up again to the initial position. The top of the detector is $\varphi = \frac{\pi}{2}$, the bottom is $\varphi = \frac{3\pi}{2}$.
Figure 3.3 shows the DØ detector. It has a length of about 20 m and a height of about 14 m. The subdetectors are indicated in different colors.

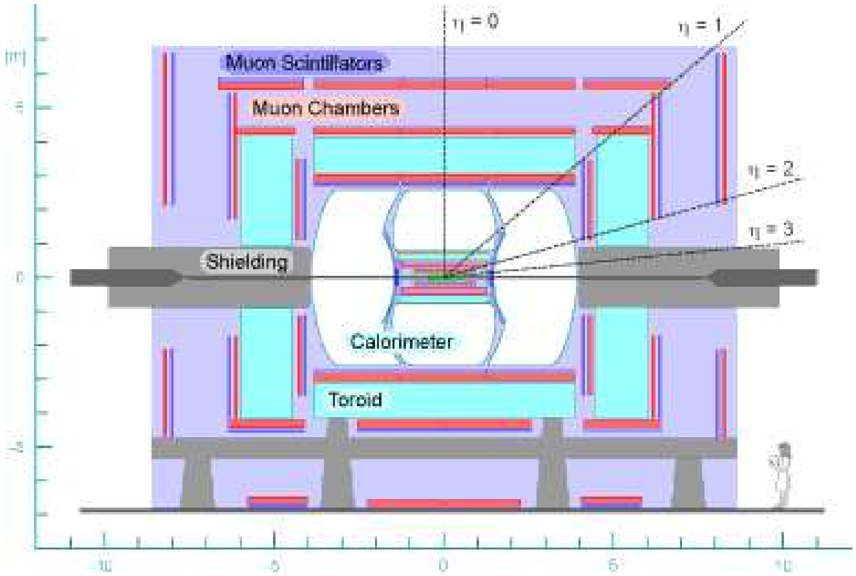

Figure 3.3.: Side view of the DØ detector. Some sample values for η are indicated with dashed lines.

In this chapter a detailed overview of the DØ detector as it was used in Run IIa will be given starting with the inner part of the detector and going to the outer part [25]. After that the trigger system will be discussed. In the last part the upgrades for Run IIb are described.

3.2.1. The Tracking System

The Silicon Microstrip Tracker

As already mentioned closest to the beam pipe the central tracking system can be found. It consists of the silicon microstrip tracker (SMT) and the central fiber tracker (CFT). They are surrounded by the solenoid providing a magnetic field of 2T.
A drawing of the tracking system can be found in Figure 3.4. The SMT is located closest to the beam pipe and has two tasks: vertexing and tracking. It consists of barrels intersected with disks in the barrel region and disks in the forward region as can be seen in Figure 3.5. There are six barrels with four layers each. The intersecting disks are called F-disks. A total of twelve F-disks can be found, half of them being directly attached to the barrel modules. The other six disks are located at both ends of the SMT, three on each side. The centers of the

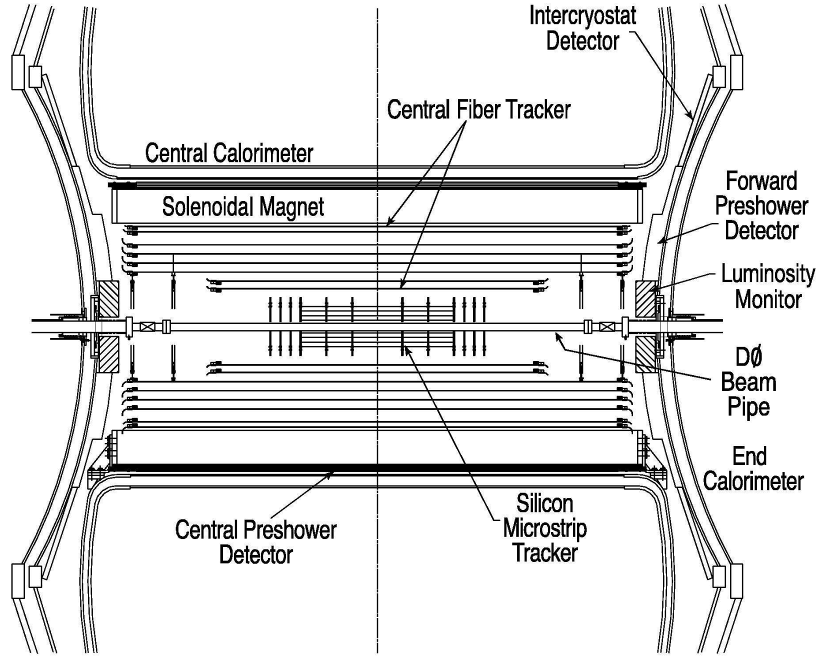

Figure 3.4.: The central tracking system of the DØ detector.

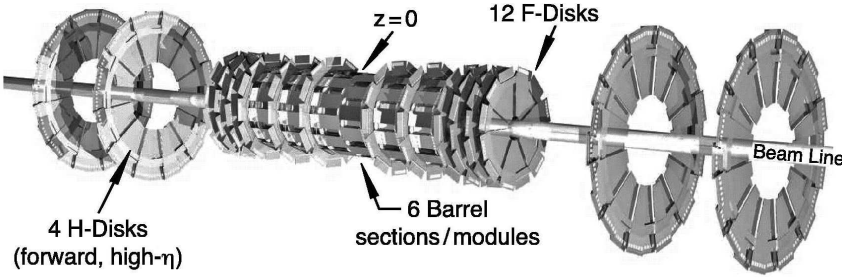

Figure 3.5.: The silicon microstrip tracker (SMT).

barrels can be found at a $|z|$ of 6.2 cm, 19.0 cm and 31.8 cm. The centers of the F-disks are at $|z| = 12.5$ cm, 25.3 cm, 38.2 cm, 43.1 cm, 48.1 cm, 53.1 cm. Additionally, four large so-called H-disks can be found in the far forward region at $|z| = 100.4$ cm and $|z| = 121.0$ cm.
This part of the detector has to be cooled to a temperature of -10 °C.

The Central Fiber Tracker

The SMT is surrounded by the CFT. It consists of scintillating fibers mounted on eight support cylinders. As can be seen in Figure 3.4, the inner two layers are shorter than the outer six ones to have room for the H-disks of the SMT. The inner two cylinders have a length of 1.66 m and the others 2.52 m. The fibers including their cladding have a diameter of 835 μm. The radii of the cylinders range from 20 cm to 52 cm. On each cylinder two doublet layers of fibers are mounted. The fibers of the first doublet layer are orientated parallel to the beam axis (axial layers). The fibers of the second doublet layer are mounted with a stereo angle of $+3°$ or $-3°$ (stereo layer). This is necessary to determine the position where a particle passed the detector because the fibers are only read out at one end. At this end of the fiber a clear fiber waveguide is attached to lead the light emitted in the scintillating fiber to the photon counters for readout. The signal of the axial layer is used for the fast and hardware-based Level 1 trigger (for triggers see Section 3.3). The Level 3 trigger uses the signal of the whole CFT. To be able to make a precise measurement the fibers had to be placed accurately, with a shift of less than 200 μm.

The Solenoid Magnet

The SMT as well as the CFT are surrounded by the solenoid magnet which was designed to allow a momentum measurement of charged particles. It has a length of 2.73 m and a diameter of 1.42 m. The size is limited by the amount of space available between the central tracking system and the calorimeter cryostat, because the magnet was added after Run I [26]. It has a nearly uniform field of about 2 T over nearly the whole volume as can be seen in the center of Figure 3.8 which shows the magnetic field of the solenoid magnet and the toroid magnets (which are going to be described later). The solenoid is wound with two layers of superconducting cable. Two different types of conductor are used to reach a higher uniformity of the central field. This is done by using a wider conductor in the central part and a narrower conductor for the other parts, so that the number of windings around the solenoid is increased.

3.2.2. The Calorimeter System

The Preshower Detector

The purpose of the preshower detector is to enhance the electron identification and the background rejection. The preshower detector is used as tracking detector as well as calorimeter to improve the matching of tracks and calorimeter showers. Furthermore it can be used to correct the energy measurements for losses in the solenoid, cables and support structures.
The preshower detector consists of two parts: the central preshower detector (CPS) and the forward preshower detector (FPS). Both CPS and FPS are made of triangular scintillator strips. The advantage of this shape and the arrangement (Figure 3.6) is the fact that there is no uncovered space through which particles might escape undetected. Most particles pass at least two strips. This allows a precise position measurement.

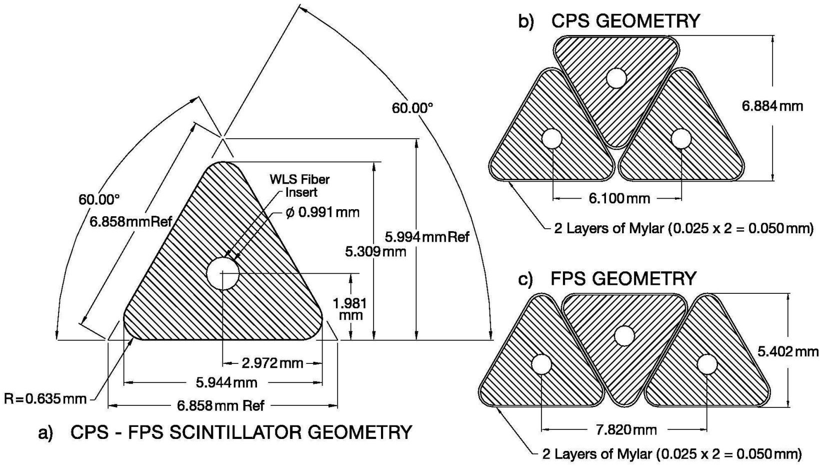

Figure 3.6.: The preshower scintillator strips and their arrangement.

The CPS is located between the solenoid and the central calorimeter and covers a region of

$|\eta| < 1.3$. It consists of three cylindrical layers: one axial layer and two stereo layers. The stereo layers are mounted with angles of 23.774° and 24.016°.
The two FPS detectors, one for each side, are mounted on the cryostat of the end calorimeters. They cover the region of $1.5 < |\eta| < 2.5$. Each consists of two layers with two sublayers. This provides four readout layers in total for each FPS. The strips in the sublayers have a stereo angle of 22.5° with respect to each other. The two layers are separated by a lead-stainless-steel absorber. Charged particles will leave a small ionizing signal in the first layer. Then they will shower in the absorber and will leave a cluster of energy in the second layer.

The Calorimeters

The calorimeter system, shown in Figure 3.7, consists of four parts: the central calorimeter, two end calorimeters and the intercryostat detector.

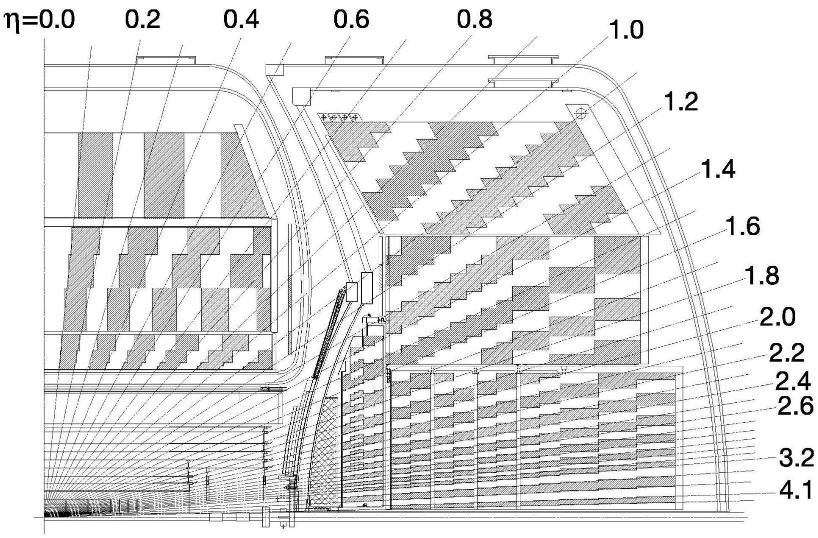

Figure 3.7.: Side view of one quarter of the calorimeter system. The system consists of the central calorimeter and the end calorimeter as well as the intercryostat detector which is located in the gap between the two cryostat vessels which contain the central calorimeter and the end calorimeter.

The calorimeters are designed to measure the energy of electrons, photons and jets, identify particles and determine the transverse energy balance in an event. Each calorimeter consists of an electromagnetic section, a fine hadronic section and a coarse hadronic section, where the electromagnetic section can be found closest to the interaction region and the coarse hadronic section in the outer part of the calorimeter. The active medium is liquid argon. The absorber plates are made from three different materials. In all electromagnetic sections they are made from depleted uranium. The absorber plates in the fine hadronic section are made from uranium-niobium alloy. In the central calorimeter the plates of the coarse hadronic section consist of copper, in the end calorimeter of stainless steel. Each of the three calorimeter has its own cryostat. Within the cryostats the temperature is kept at 90 K. The central calorimeter covers a region of $|\eta| \lesssim 1.0$ while the end calorimeter covers the region up to $|\eta| \approx 4.0$.

The Intercryostat Detector

Due to the gap between the calorimeter cryostats the calorimeters do not cover $0.8 < |\eta| < 1.4$ completely. That is why the intercryostat detector (ICD) was mounted on the outer surface of the end calorimeter cryostats. It covers $1.1 < |\eta| < 1.4$. The remaining space between the cryostats is needed for cables leading to the central tracking system.

The ICD consists of scintillating tiles in light aluminum boxes. Each tile is divided into twelve subtiles which are optically isolated from one another. The subtiles are connected to wavelength shifting fibers for readout.

3.2.3. The Muon System

The Toroid Magnets

Besides the solenoid magnet which was described in Section 3.2.1 the detector has a second system of magnets, the toroid magnets, in the outer part. It is part of the muon system. The toroid magnets allow a stand-alone muon momentum measurement. This improves the matching with central tracks and the resolution of muons with high momentum.

The inner radius of the central toroid is about 318 cm and the outer radius about 427 cm. The toroid covers a region of $|\eta| \lesssim 1$. It is divided into three parts to allow access to the inner part of the detector. The center bottom part is fixed to the detector while the other two parts can be moved perpendicular to the beam axis. The toroid consists of 20 coils with ten windings each.

The end toroid magnets have an inner radius of about 92 cm and an outer radius of about 426 cm. They consist of eight coils with eight windings each.

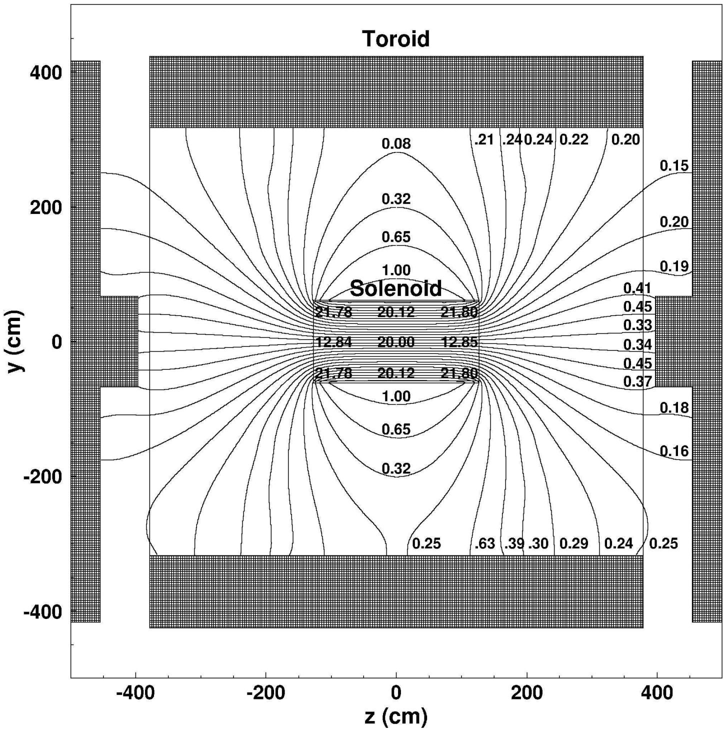

Figure 3.8.: The magnetic field provided by solenoid magnet and toroid magnets.

This magnet provides a field of about 1.8 T. The whole magnetic field produced by solenoid and toroid is shown in Figure 3.8.

The Muon Detectors

The muon system consists of a central muon detector and forward muon detectors. The system consists of drift tubes and scintillation counters which can be seen in Figures 3.9 and 3.10, respectively.

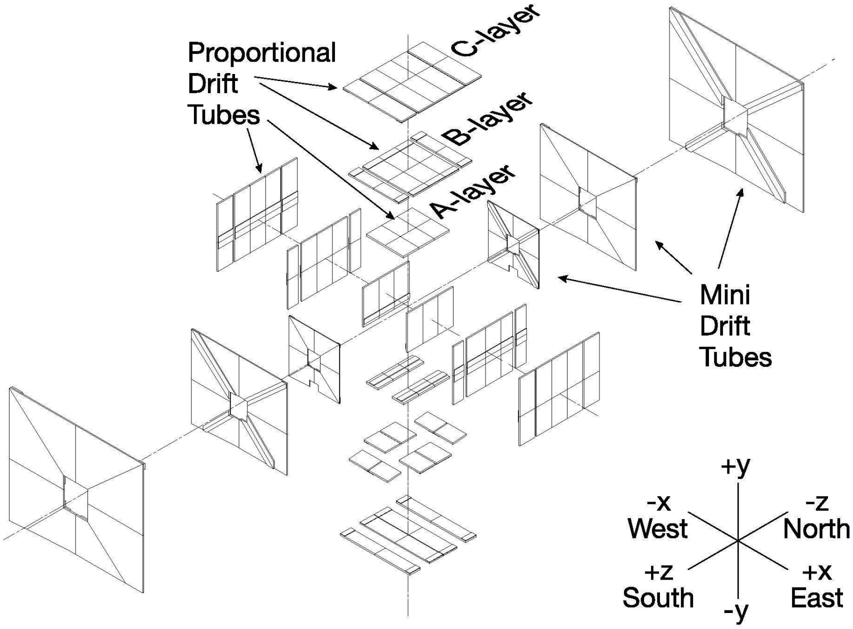

Figure 3.9.: Muon drift chamber system of the DØ detector.

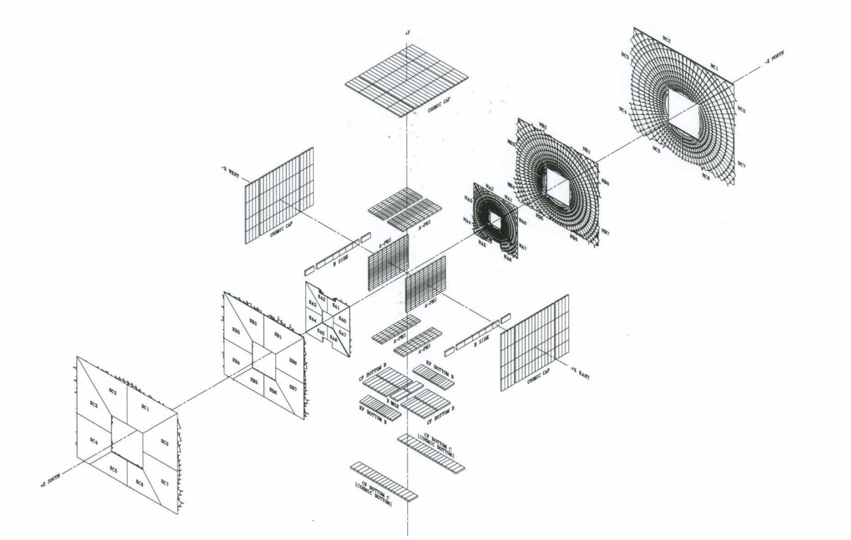

Figure 3.10.: Muon scintillation counter system of the DØ detector.

The central muon system covers $|\eta| \lesssim 1$ and consists of the toroid magnets which were described previously, drift chambers, cosmic cap, cosmic bottom and Aϕ scintillation counters.

There are tree layers of drift chambers which are called layer A, layer B and layer C, where layer A is the innermost layer and layer C the outermost. As can be seen in Figure 3.3 layer A is located inside the toroid magnet while the other two are located outside the magnet. This allows to measure muons with low energy which cannot pass the toroid magnet. The drift chambers are made of proportional drift tubes (PDTs) made from aluminum.

The cosmic cap and the cosmic bottom scintillators are attached to the top, sides and bottom of the C-layer of PDTs (or B-layer in places where no C-layer is installed). The cosmic caps were installed during Run I. The cosmic bottom was added for Run II. They are made of fast scintillation counters and help associating muons in the PDTs with a bunch crossing and this way reducing cosmic background.

The Aϕ scintillation counters cover the layer A of PDTs. They help identifying muons, triggering on muons and reject backscattering.

The forward muon system covers the region $1.0 \lesssim |\eta| \lesssim 2.0$. It consists of four parts. The forward toroid magnet as described before, and for tracking there are three layers of Mini Drift Tubes (MDTs) (layers A, B and C), for triggering three layers of scintillation counters (layers A, B, C) and shielding (see Figure 3.3).

The MDTs have good resolution and radiation hardness. Layer A of MDTs is installed closest to the interaction point within the toroid magnets, layers B and C outside the toroid magnets. The longest tubes can be found in the C-layer with a length of 5.8 m.

The three layers of trigger scintillation counters are installed in the detector similarly to the MDTs; layer A can be found inside the toroid magnet, the other two outside the magnet. They are made to provide a good timing resolution, a good background rejection and muon detection efficiency.

The shielding finally can be found around the beam pipe extending from the calorimeter cryostat to the wall of the collision hall as can be seen in Figure 3.3. The task of the shielding is to reduce the background which is produced by beam halo and by remains of protons and antiprotons that interact with the beam pipe or the quadrupole magnets of the Tevatron.

3.2.4. The Forward Proton Detector

The forward proton detector (FPD) was installed to measure protons and antiprotons which are scattered at small angles. The detectors consist of scintillating fibers. Each FPD is housed in a Roman Pot which again is housed in a chamber made from stainless steel. These chambers are called castles. There is a total of 18 Roman Pots in six castles. The arrangement can be seen in Figure 3.11.

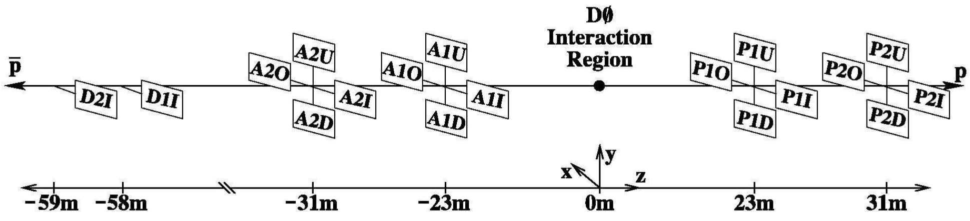

Figure 3.11.: Position of the forward proton detector.

3.2.5. The Luminosity Monitor

The luminosity monitor (LM) is located in front of the end calorimeter cryostat between the beam pipe and the forward preshower detector at $|z| = 140$ cm (Figure 3.3). It covers a region of $2.7 < |\eta| < 4.4$ and consists of plastic scintillation counters. The subdetector was installed to determine the luminosity at the interaction point at DØ. It detects inelastic collisions of protons and antiprotons and measures beam halo rates as well as the z position of the primary vertex. This subdetector is exposed to high radiation which mainly comes from the collisions of protons and antiprotons.

3.3. The Trigger

Due to the high bunch crossing rate and therefore high interaction rate it is necessary to have a good and fast trigger to discriminate between interesting events and events that can be rejected.

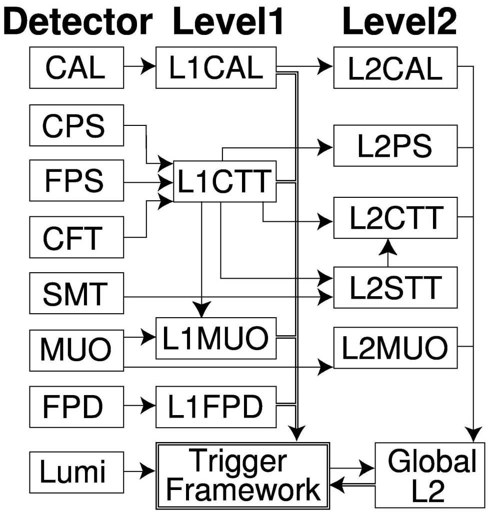

Figure 3.12.: Overview over the trigger used at DØ.

An overview over the trigger system used at DØ is shown in Figure 3.12. It has three levels. The Level 1 trigger (L1) is completely hardware based and has an accept rate of about 2 kHz. Level 2 (L2) has both a hardware component, and a software component while the Level 3 trigger (L3) is software based only. L2 and L3 have accept rates of about 1 kHz and 50 Hz, respectively. The output of L3 is written to tape. In the following sections these levels will be described in more detail.

3.3.1. Level 1 Trigger

The L1 trigger looks at every event and decides whether to let it pass or to reject it. This must be done within 3.5 μs or less.

The L1 calorimeter trigger (L1Cal) receives information directly from the calorimeter and looks for energy deposits higher than the programmed value. The L1 central track trigger (L1CTT) gets information from the axial layers of the CFT as well as from the preshower detectors. It looks for charged particles and reconstructs their tracks. Additionally, it matches tracks and clusters in the CPS. The L1 muon trigger (L1Muo) gets its information from the muon system and from the L1CTT. It looks for hits in the muon chambers and matches tracks to these hits. Finally there is the L1 forward proton detector trigger (L1FPD). It triggers on events in which outgoing particles pass one or more of the detectors. However, events with many hits are rejected to reduce beam halo background.

In the end the information from L1Cal, L1CTT, L1Muo as well as L1FPD is sent to the trigger framework (TFW). Here a decision is made whether the event is examined further or not.

3.3.2. Level 2 Trigger

The L2 trigger consists of preprocessors for each subdetector and a global processor (L2Global). The preprocessors get information from the L1 trigger as can be seen in Figure 3.12 and form physics objects. The L2 calorimeter trigger (L2Cal) gets information from L1Cal. It identifies electrons, photons, and jets and calculates the $\not{E}_T$ for each event. The L2 muon system (L2Muo) receives information from the L1Muo and directly from the detector. It is designed to improve the quality of muon candidates. The L2 preshower preprocessor (L2PS) gets information from the L1CTT and provides a good background rejection as well as a discrimination between electrons and photons. The L2STT uses data from the SMT for pattern recognition. It also uses L1CTT information to reconstruct tracks found with the CFT with high precision. The L2STT is capable of determining impact parameters of tracks and therefore tagging decay products of long-lived particles. The L2CTT finally gets information from the L1CTT and the L2STT.

The L2 global processor looks for correlations in signatures in the whole detector system and selects events. The decision is based on the physics objects created by the L2 preprocessors. It also receives information about L1 trigger decisions from the TFW.

3.3.3. Level 3 Trigger and the Data Acquisition System

The Level 3 trigger (L3) rejects additional events to reduce the number of events and the rate that is written to tape. It performs an event reconstruction and its decision is based on physics objects and their relationship. The muon scintillator hits and the hits in the wire chambers inside and outside the toroid are used to reconstruct parts of the muon tracks. Cosmic muon background is reduced. This is made possible because L3 is able to provide a good separation between out of time hits (hits which cannot be matched to a bunch crossing) and hits produced by a muon coming from a proton-antiproton collision. Tracking is performed by fitting a circle to the hits in the CFT. The L3 trigger can also calculate the position of the vertex in three dimensions.

The data acquisition system transports the data from the readout crates to the L3 farm nodes. An overview of the data and information flow is shown in Figure 3.13. The single board computers (SBCs) in the crates send the data to the L3 farm nodes. The event builder (EVB) process on the farm nodes collects all parts of the event and builds a complete event. After the L3 farm nodes finished processing the events, they send them to the online host system, where they are written to tape.

3.4. Detector and Trigger Upgrades for Run IIb

The DØ Detector was upgraded in the shutdown 2006 between Run IIa and Run IIb. Basically the setup is as described in Section 3.2 and Section 3.3. However, some changes have been done.

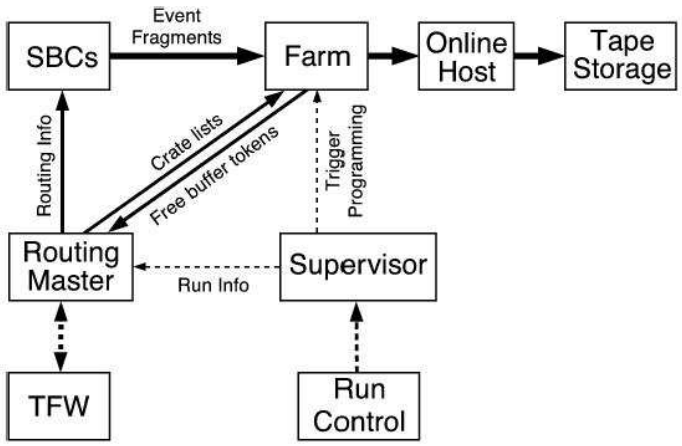

Figure 3.13.: Schematic view of the DAQ system. Data and information flows are displayed as arrows.

- A new innermost layer for the SMT was installed, which is called Layer 0 [27, 28]. The existing detector gave constraints on the design of Layer 0 because it had to fit into it. A picture of this layer is shown in Figure 3.14. It consists of one layer built from a radiation hard material. This is necessary to avoid damages due to the strong radiation close to the interaction region. The sensors are mounted at a distance of 17 mm from the center of the beam pipe. The advantage of the new layer is a better impact parameter resolution.

- Compared to Run IIa in Run IIb higher instantaneous and integrated luminosities are available. To cope with these higher luminosities the trigger system is required to have a higher background rejection efficiency. The following trigger subsystems were upgraded [29]:
  - **L1 calorimeter trigger.** A digital filter was introduced to improve the rejection of pile-up effects. Additionally, a new algorithm was introduced to improve the trigger performance.
  - **L1 central track trigger.** To improve the resolution of the L1CTT the CFT doublet layers are treated as singlet layers.
  - **New Level 1 system.** A new Level 1 system to match energy clusters in the calorimeter with central tracks was added.
  - **L2 processors.** The processors were replaced to deliver more computing power.
  - **L2 silicon track trigger.** The L2STT had to be expanded due to the additional layer 0 of the SMT.

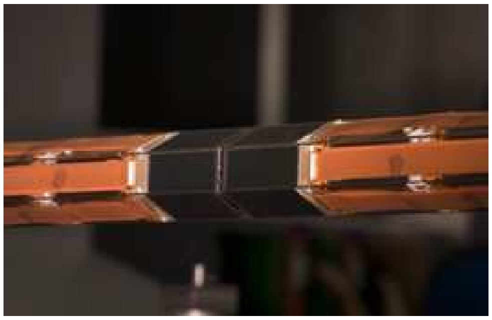

Figure 3.14.: Layer 0 before being installed in the DØ Detector during the shutdown in 2006.

4. Particle Identification and Data Reconstruction

In this chapter the data reconstruction process will be described briefly in the first part. In the second part particle identification criteria are described.

4.1. Data Reconstruction

The reconstruction of data is necessary because the raw data, as they were taken with the detector, only contain hit information, energies and trigger information. To analyze the data, physics objects like muons, electrons and jets have to be reconstructed.
The data reconstruction process consists of several steps. As a first step tracks, electromagnetic and hadronic energy clusters and the $\not\!\!E_T$ of the events are reconstructed. To identify particles criteria as described in Section 4.2 are used. As a next step skims are produced. Skims are preselections with very loose requirements. All available skims can be found on the web page of the Common Samples Group [30].

4.2. Particle Identification

Identification criteria are used to discriminate between different type of particles in the detector. For this the behavior of the particles in the detector is taken into account. Each particle has its own signature which makes it possible to discriminate between them (see Figure 4.1).

- **Photons:** Deposit their energy mainly in the electromagnetic calorimeter.
- **Electrons:** Leave a track in the central tracking system and deposit their energy mainly in the electromagnetic calorimeter.
- **Muons:** Leave a track in the central tracking system, deposit some energy in the calorimeter (but are not stopped by it as the electrons are) and are detected in the muon chambers in the outer part of the detector.
- **Quarks and Gluons:** Cannot exist unbound and build hadrons. Charged hadrons leave tracks in the tracker. All hadrons deposit all of their energy in the electromagnetic and the hadronic calorimeter. They are reconstructed as jets.
- **Neutrinos:** Cannot be detected with the DØ detector. They are measured as missing transverse energy.

An overview over all criteria is given in this following.

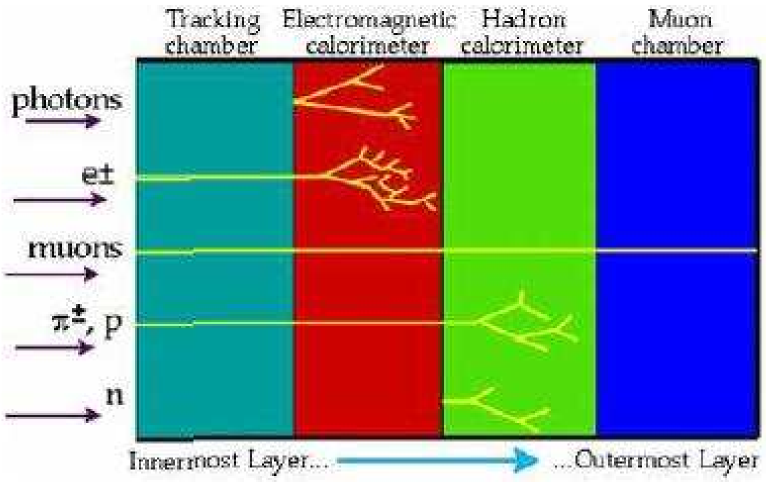

Figure 4.1.: Different particles in a typical detector as used in collider experiments.

4.2.1. Jets

Quarks and gluons can only exist in bound states, they build hadrons. Thus quarks and gluons are measured in the hadronic section of the calorimeter. Charged hadrons additionally leave a track in the tracking system. Quarks and gluons are reconstructed as jets with a cone algorithm [31, 32]. It is unlikely to have no charged particles in a jet. That is why jets without associated tracks are expected to come from noise which is not produced by particles.

Jet candidates also include electrons and photons. They have to be removed. Hadrons deposit their energy not only in the hadronic calorimeter, but also in the electromagnetic calorimeter. Electrons and photons might not only deposit their energy in the electromagnetic calorimeter, but also in the hadronic calorimeter. However, it is expected that electrons and photons deposit their energy mainly in the electromagnetic calorimeter, while a significant fraction of the energy of hadrons is deposited in the hadronic section of the calorimeter. To discriminate between hadrons and other particles the electromagnetic fraction f_{EM} is introduced. This number is the energy fraction deposited by a particle in the electromagnetic calorimeter. If $f_{EM} < 0.05$ hardly any energy is deposited in the electromagnetic calorimeter and the jet is likely to be produced by noise. If, on the other hand, the electromagnetic fraction is very high ($f_{EM} > 0.95$), it is likely the energy deposition was produced by an electron or a photon. However, the lower limit slightly depends on the position where the jet was measured in the detector. This is due to gaps in the electromagnetic calorimeter in the intercryostat region.

Next to the electromagnetic fraction a coarse hadronic fraction CHF is introduced. It denotes the energy fraction deposited in the coarse hadronic calorimeter. Jets with a high CHF are likely to be noise jets. Basically, the coarse hadronic fraction is required to be smaller than 0.4. However, as the limit for f_{EM}, this limit depends on the η region.

An additional criterion is the removal of hot cells and hot towers. These are calorimeter cells or combinations of calorimeter cells (calorimeter towers) in which energy is deposited without relation to any events.

Finally, a cross check is done to make sure the energy measured with the precision readout matches the energy read out by the L1 trigger (see Section 3.3). For this the variable

$$L1_{ratio} = \frac{p_T^{L1readout}}{p_T^{precision\ readout}} \tag{4.1}$$

is defined. The value of this variable should be somewhere between larger than 0.1 – 0.5, depending on p_T and η.
The measured energy of jets might not be the same as the energy the parton initially had. That is why the jet energy scale (JES) correction is applied. This correction takes into account the response of the calorimeter and underlying events.
Another important correction is the correction for muons. Muons do not deposit all of their energy in the calorimeter as the other particles do. So if there is a muon in the jet, the jet energy has to be corrected. For this the p_T of the muon track is used.

4.2.2. Electrons

Electrons can be seen in the detector in two places. Due to their electric charge they leave tracks in the central tracking system. They deposit their energy mainly in the electromagnetic calorimeter, but a small fraction might also be deposited in the hadronic section. To discriminate between electrons and other particles several criteria are applied [33].
The electromagnetic clusters are built from cells in the electromagnetic calorimeter as well as from the innermost layer of the hadronic calorimeter. The transverse energy of a cluster is required to be at least 1.5 GeV. A large fraction of the energy ($f_{EM} \geq 0.9$) is expected to be deposited in the electromagnetic calorimeter. Furthermore, electrons (and photons) are expected to produce narrow showers. That is the reason why it is required that at least 40% of the energy must be deposited in the most energetic tower. Also the shower shape is examined and compared to a typical shower produced by an electron. To perform this comparison seven observables are used: the total electromagnetic energy, the z position of the vertex, the transverse width of the shower in φ, and four electromagnetic energy fractions. These observables are correlated. The inverse covariance matrix of the shower, the so-called H-matrix, is compared to the H-matrix of a typical electron. The χ^2 should be smaller than 50.
Additionally, electromagnetic clusters are supposed to be isolated in the calorimeter. For electrons a track with $p_T \geq 5$ GeV is required to be matched to the electromagnetic cluster.
To further discriminate between electrons and other particles and to reduce background the so-called electron likelihood is used [34]. For this likelihood a variety of variables is taken into account including the electromagnetic fraction f_{EM}, the ratio of transverse energy from the calorimeter system and transverse momentum from the tracking system, the transverse track momentum and the number of tracks close to the candidate. Additionally, the χ^2 for the comparison between the two H-matrices and the χ^2 of the track match and the distance of closest approach (DCA) is used, which is the distance between the track of the candidate and the primary vertex in the transverse plane. The likelihood has to be larger than 0.85.

4.2.3. Muons

To identify muons the muon system and the inner tracking system are used [35], because muons leave tracks in both the inner tracking (SMT and CFT, see Section 3.2.1) system and the muon chambers. They also deposit a small fraction of their energy in the calorimeter.
In the muon system hits in all three layers are required. Muon tracks detected in the muon chambers are matched to central tracks. The distance of closest approach is used as well. If

SMT hits are present the upper limit of the DCA is lower (< 0.02 cm) than in the absence of SMT hits (< 0.2 cm).
The central track has to be of medium quality, meaning, that the DCA criteria has to be fulfilled and the χ^2_{track} is smaller than 4.
Cosmic Muons are rejected by using timing information. Only those muons are accepted, which arrive within a few nanoseconds around the expected time of arrival of muons coming from an interaction during a bunch crossing. Further reduction of the cosmic muon background is achieved by the (DCA) criteria.

4.2.4. Neutrinos

Neutrinos themselves cannot be detected directly with the DØ detector. But there is the possibility of detecting them indirectly via the measurement of the missing transverse energy $\not{E}_T$ [36]. The missing transverse energy $\not{E}_T$ is calculated from the electromagnetic calorimeter and the fine hadronic calorimeter. The coarse hadronic calorimeter is not used because the noise in this section is high. Using it would lead to a wrong energy measurement. Instead the $\not{E}_T$ is corrected for the energy fraction deposited in the hadronic calorimeter belonging to reconstructed jets. The missing transverse energy has to be corrected for muons as well because these particles do not deposit their whole energy in the calorimeter. Without this correction the calculated $\not{E}_T$ would be too high.

5. Monte Carlo Simulation

To simulate most of the possible processes which could appear in a proton-antiproton collision event generators are used. In the analysis presented in this thesis the event generators called ALPGEN [37] and PYTHIA [38] are used. However, other event generators exist as well. ALPGEN generates events on parton level but does not simulate the hadronization of the partons. Hadronization can be simulated by combining ALPGEN with a shower generator. PYTHIA uses a parton shower ansatz to simulate partons. The hadronization is simulated by a string fragmentation model. ALPGEN and PYTHIA can be combined so that instead of PYTHIA's parton shower ansatz the matrix element ansatz is used. This leads to a better description of the topology of high p_T jets.

To avoid double counting of jets an MLM matching [39, 40] is performed. Monte Carlo samples are generated for each exclusive parton multiplicity individually. Jets from parton showers are matched to the initial partons. If the number of partons differs from the number of reconstructed jets, the event is rejected.

The creation of such simulated events (in the following called Monte Carlo events or only Monte Carlo) is done in several steps.

As a first step events are generated randomly according to the standard model. Simulation of the collision, the physics process as well as gluon radiation and the decay of particles are included.

Hard interactions between partons are calculated with perturbative QCD using leading order Feynman graphs. The parton momenta come from parton density functions (pdfs) (CTEQ6L1) [41]. Initial and final state radiation is calculated based on models which were found empirically. These Monte Carlo events are events how they would look like without the detector detecting them. However, the particles in the final state interact with the matter of the detector. To compare Monte Carlo events to data events the detector has to be simulated as well, which is done with a GEANT simulation [42, 43]. The simulation of the DØ detector consists of two parts. One part simulates the interactions of particles with the detector and the responses of the detector. Here it has to be taken into account that not only particles from the collision produce hits. The so called underlying events have to be taken into consideration as well. Underlying events can have different sources such as multiple hard interactions in a bunch crossing, pile-up, interactions of proton and antiproton remnants and noise hits. Multiple interactions per bunch crossing often appear at high luminosities. Pile-up is an effect caused by residual energies from the previous bunch crossing.

The other part of the detector simulation takes the geometry of the detector into account. This way lower acceptances in the bottom hole and the IC region are simulated. The effect can be seen in plots showing the φ distribution of muons. Muons were simulated randomly, so the distribution is expected to be flat. After detector simulation the number of muons drops in the region around $\varphi = \frac{3\pi}{2} \approx 4.7$ (see Figure 5.1). This is the bottom hole which is not covered with muon detectors. However, muons can still be reconstructed in this region using the central tracking system and the calorimeter.

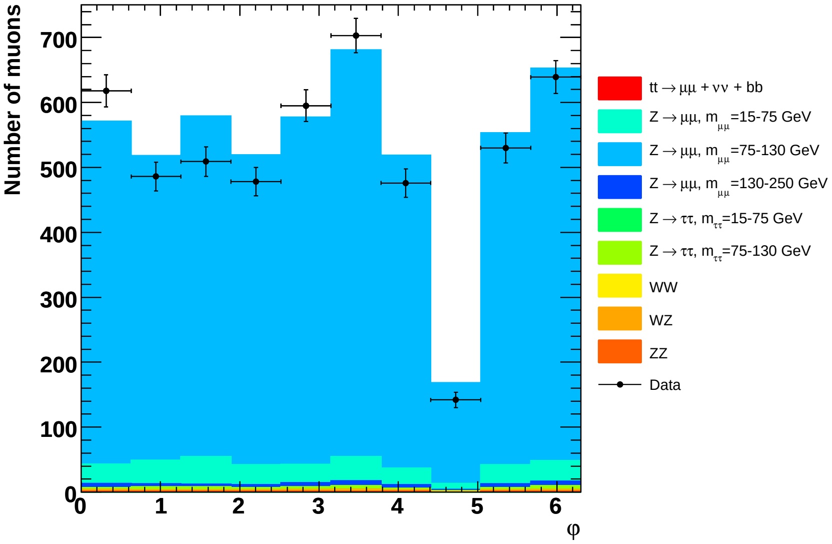

Figure 5.1.: The φ distribution of muons in the one jet inclusive plot (all events with at least one jet are taken into account for this plot) is shown. As dots with error bars Run IIb data are shown, in different colors the Monte Carlo Simulation (after the detector simulation) is shown. The bottom hole around $\varphi \approx 4.7$ can be seen easily. The integrated luminosity is 1216 pb^{-1}.

6. Analysis

This chapter describes the analysis. It is divided into two main parts. In the first part the dimuon selection will be presented for the Run IIb preshutdown dataset as well as the Run IIa dataset. While the selection for the Run IIa dataset is described very briefly, the emphasis lies on the selection for the Run IIb dataset. First an overview over the selection will be given and the determination of the fake muon background is presented. To show the agreement between data and Monte Carlo comparison plots are shown after various steps of the selection. Also the Run IIb selection for the $e\mu$ channel is presented briefly.

In the second part the mass measurement of the top quark with the neutrino weighting method in the $\mu\mu$ and $e\mu$ channels is presented. First the method itself will be described as well as the ensemble testing. After that the results for the two channels are presented as well as the combination of both channels.

6.1. The Datasets

6.1.1. Data

The Run IIa dataset contains all data taken until the shutdown in 2006. During this shutdown the DØ Detector was upgraded, see Section 3.4. The Run IIb preshutdown data were taken between summer 2006 and summer 2007. The two datasets have about the same size, about 1069 pb^{-1} in the Run IIa dataset and about 1216 pb^{-1} in the Run IIb preshutdown dataset. Thus similar results are expected for the selections of the two datasets.

For the Run IIb dimuon selection a skim by the Common Samples Group is used [30]:

CSG_CAF_2MUhighpt_PASS2_p21.05.00_all_fixed2007.

For the skim very loose cuts were applied including the requirement that two high p_T muons were detected. At this point the high p_T is still low compared to the p_Ts required in the dimuon selection which will be described later.

Next to the Run IIb preshutdown dataset for the $e\mu$ selection also Run IIb postshutdown data were used (about 560 pb^{-1} [44]). These data were taken after the shutdown in 2007. So a higher integrated luminosity is available for this channel.

6.1.2. Monte Carlo Simulation

In the analysis Monte Carlo is used for two purposes: For comparison between data and Monte Carlo in the dimuon selection and to create a template in the neutrino weighting method (see Section 6.6.1). For the dimuon selection Monte Carlo events created with the ALPGEN [37] event generator were used for the Z background as well as the $t\bar{t}$ signal (generated for $m_{top} = 170$ GeV) while the PYTHIA [38] event generator was used for the diboson backgrounds. For the templates used in the top quark mass measurement, PYTHIA Monte Carlo was used. Monte Carlo for different generated top quark masses between 155 GeV and 200 GeV (in 5 GeV steps) were used for the dimuon channel while Monte Carlo for masses between 160 GeV and 190 GeV (in 5 GeV

steps) were used for the $e\mu$ channel.
The Monte Carlo for the Z processes is produced in three different mass bins (regarding the dimuon invariant mass): $15 - 75$ GeV, $75 - 130$ GeV and $130 - 250$ GeV. In Run IIa they were slightly different: $15 - 60$ GeV, $60 - 130$ GeV and $130 - 250$ GeV. For $Z \to \mu\mu$ all three mass ranges are used, for $Z \to \tau\tau$ only the two lowest ones, because for the highest mass range of this process the background is very small (see comparison plots in Appendix B and Figures 6.1 and 6.2). That is why this mass range is not used in the selection of Run IIb data. Additionally, Z Monte Carlo and $t\bar{t}$ Monte Carlo was generated for different parton multiplicities ranging from 0 light partons (lp) exclusive to 2 light parton inclusive for signal and from 0 light partons exclusive to 3 light partons inclusive for Z processes. Here "exclusive" means exactly the given number of light partons was generated. "Inclusive" means the given number or more partons were generated. The partons then build jets in the detector. The reason why Monte Carlo was generated separately in the described way is to get high statistics even in regions of the phase space where the cross section is small. The cross sections for the different mass ranges then are taken into account via a weight which is applied.
A list of all Monte Carlo samples used for the dimuon selection together with the cross sections for each of the channels is given in Table 6.1.

6.2. Dimuon Selection for the Run IIa Dataset

In the new selection for the Run IIb dataset the same cuts are applied as in the selection for the Run IIa dataset. The cuts are described below in Section 6.3.1. For both selections the same software was used but for the new selection the software version was newer. The difference between the two selections is that the Run IIb selection was done with a new software package called `vjets_cafe`, while the Run IIa selection was done with a software package called `top_cafe`. A second difference is, that in the Run IIa selection heavy flavor skimmed Monte Carlo was used to enrich the sample with such events containing charm and bottom quarks. That is why in the Run IIa comparison plots four additional background processes can be seen:

- $Z+ \to \mu\mu + c\overline{c}$
- $Z+ \to \mu\mu + b\overline{b}$
- $Z+ \to \tau\tau c\overline{c}$
- $Z+ \to \tau\tau b\overline{b}$

The new Run IIb code was modeled after the Run IIb code for the $e\mu$ selection, which is briefly described in Section 6.4. Before applying the new Run IIb code on the Run IIb preshutdown dataset the code was extensively tested. This was necessary to make sure the code was doing the same as the Run IIa code, which is expected to be correct. The easiest way to perform these tests is to apply the new code on the Run IIa dataset. For this dataset a dimuon selection already existed using an old software version [45]. Therefore results were available to compare with. To perform this test several steps were done which are described in the following.
As a first step the original Run IIa code was run on Run IIa data with Run IIa software. It was possible to reproduce the results and the comparison plots looked reasonable. When the testing started there was no final version of the Run IIa dimuon selection available because work was still in progress. So the following comparisons were not done with the final version described in [45] but an earlier version. However, the differences between the version used and the final version are small and do not have a big effect. Some comparison plots for the version used for

Process	parton multiplicity	cross section in $\times 10^{-6}$ pb
$t\bar{t}$, $m_{top} = 170$ GeV	0lp excl	0.5180
$t\bar{t}$, $m_{top} = 170$ GeV	1lp excl	0.2093
$t\bar{t}$, $m_{top} = 170$ GeV	2lp incl	0.1037
$Z \rightarrow \mu\mu$, $m_{\mu\mu} = 15 - 75$ GeV	0lp excl	337.9767
$Z \rightarrow \mu\mu$, $m_{\mu\mu} = 15 - 75$ GeV	1lp excl	40.1158
$Z \rightarrow \mu\mu$, $m_{\mu\mu} = 15 - 75$ GeV	2lp excl	9.8624
$Z \rightarrow \mu\mu$, $m_{\mu\mu} = 15 - 75$ GeV	3lp incl	2.77433
$Z \rightarrow \mu\mu$, $m_{\mu\mu} = 75 - 130$ GeV	0lp excl	133.09553
$Z \rightarrow \mu\mu$, $m_{\mu\mu} = 75 - 130$ GeV	1lp excl	40.65737
$Z \rightarrow \mu\mu$, $m_{\mu\mu} = 75 - 130$ GeV	2lp excl	9.95123
$Z \rightarrow \mu\mu$, $m_{\mu\mu} = 75 - 130$ GeV	3lp incl	3.21468
$Z \rightarrow \mu\mu$, $m_{\mu\mu} = 130 - 250$ GeV	0lp excl	0.884557
$Z \rightarrow \mu\mu$, $m_{\mu\mu} = 130 - 250$ GeV	1lp excl	0.344855
$Z \rightarrow \mu\mu$, $m_{\mu\mu} = 130 - 250$ GeV	2lp excl	0.085412
$Z \rightarrow \mu\mu$, $m_{\mu\mu} = 130 - 250$ GeV	3lp incl	0.0454973
$Z \rightarrow \tau\tau$, $m_{\tau\tau} = 15 - 75$ GeV	0lp excl	337.9767
$Z \rightarrow \tau\tau$, $m_{\tau\tau} = 15 - 75$ GeV	1lp excl	40.1158
$Z \rightarrow \tau\tau$, $m_{\tau\tau} = 15 - 75$ GeV	2lp excl	9.8624
$Z \rightarrow \tau\tau$, $m_{\tau\tau} = 15 - 75$ GeV	3lp incl	2.77433
$Z \rightarrow \tau\tau$, $m_{\tau\tau} = 75 - 130$ GeV	0lp excl	133.09553
$Z \rightarrow \tau\tau$, $m_{\tau\tau} = 75 - 130$ GeV	1lp excl	40.65737
$Z \rightarrow \tau\tau$, $m_{\tau\tau} = 75 - 130$ GeV	2lp excl	9.95123
$Z \rightarrow \tau\tau$, $m_{\tau\tau} = 75 - 130$ GeV	3lp incl	3.21468
$WW \rightarrow ll\nu\nu$		1.259712
$WZ \rightarrow lljj$		0.251504448
$WZ \rightarrow lll\nu$		0.100349838
$ZZ \rightarrow lljj$		0.120543552
$ZZ \rightarrow llll$		0.01451411

Table 6.1.: List of all Monte Carlo samples, which were used for the Run IIb dimuon selection, and the cross sections for each process.

the comparisons are shown in Figures 6.1 and 6.2, and also in Appendix B. Here “inclusive” now means the given number of jets was reconstructed.
After that step was successful the software was updated to the new versions for the Run IIb analysis. The selection was repeated with the Run IIa code and the Run IIa dataset. The results were compared to the results from the previous step. However, the result could not be reproduced exactly with the new software version. Examining the cut flows and the efficiencies of the cuts it turned out that differences were observed in the $\not\!\!E_T$ calculation and the $\not\!\!E_T$ significance (an explanation of the $\not\!\!E_T$ significance calculation can be found in Section 6.3.1) calculation. There had been changes in the code calculating these variables. These differences are small. To give an example one of the events not being selected with Run IIa software due to the $\not\!\!E_T$ significance cut was selected with Run IIb software. With the Run IIb software this event had an $\not\!\!E_T$ significance of 5.00386 which is only slightly over the limit of 5. To examine how big the differences in the two software versions are, the $\not\!\!E_T$ significances were printed out for some of the events left in both

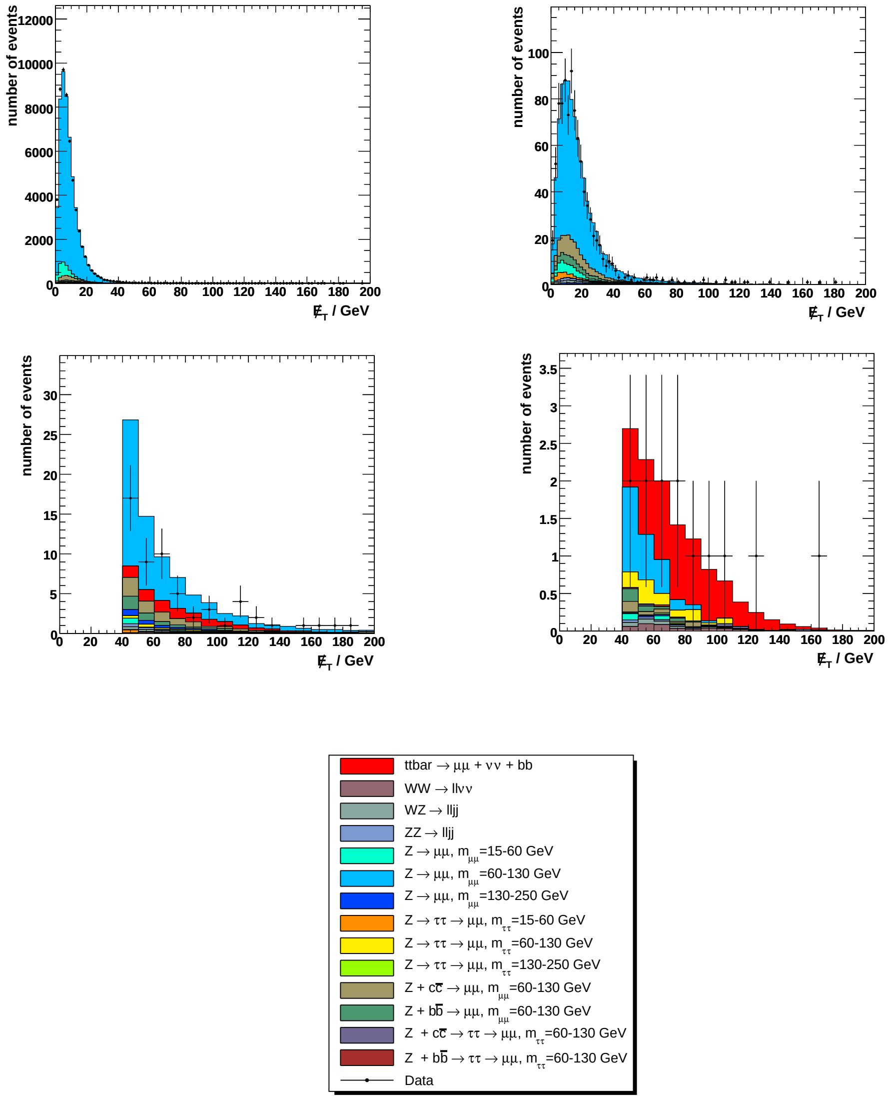

Figure 6.1.: Comparison plots showing the missing transverse energy for the following jet multiplicities: 0 jet inclusive (upper left plot), 2 jet inclusive (upper right plot), 2 jet inclusive after $\not{E}_T$ cut (lower left plot), 2 jet inclusive after all cuts (lower right plot). Run IIa data were used. The integrated luminosity is 1096 pb^{-1}.

versions. It turned out that differences ranged between 0.0007 and 0.0975, which are not that large differences. So the different number of selected events can be explained in the difference of the $\not{E}_T$ significance algorithm in the two software versions. The numbers for the $\not{E}_T$ significances and the differences are given in Table 6.2. After these results turned out to be reasonable and differences were understood the Run IIb code was used with the Run IIb software on Run IIa data to repeat the Run IIa selection. These results were compared to the results produced with the Run IIa code, Run IIb software and the Run IIa dataset. At this stage not only the number of events after various cuts was compared but also the values of several kinematic variables.

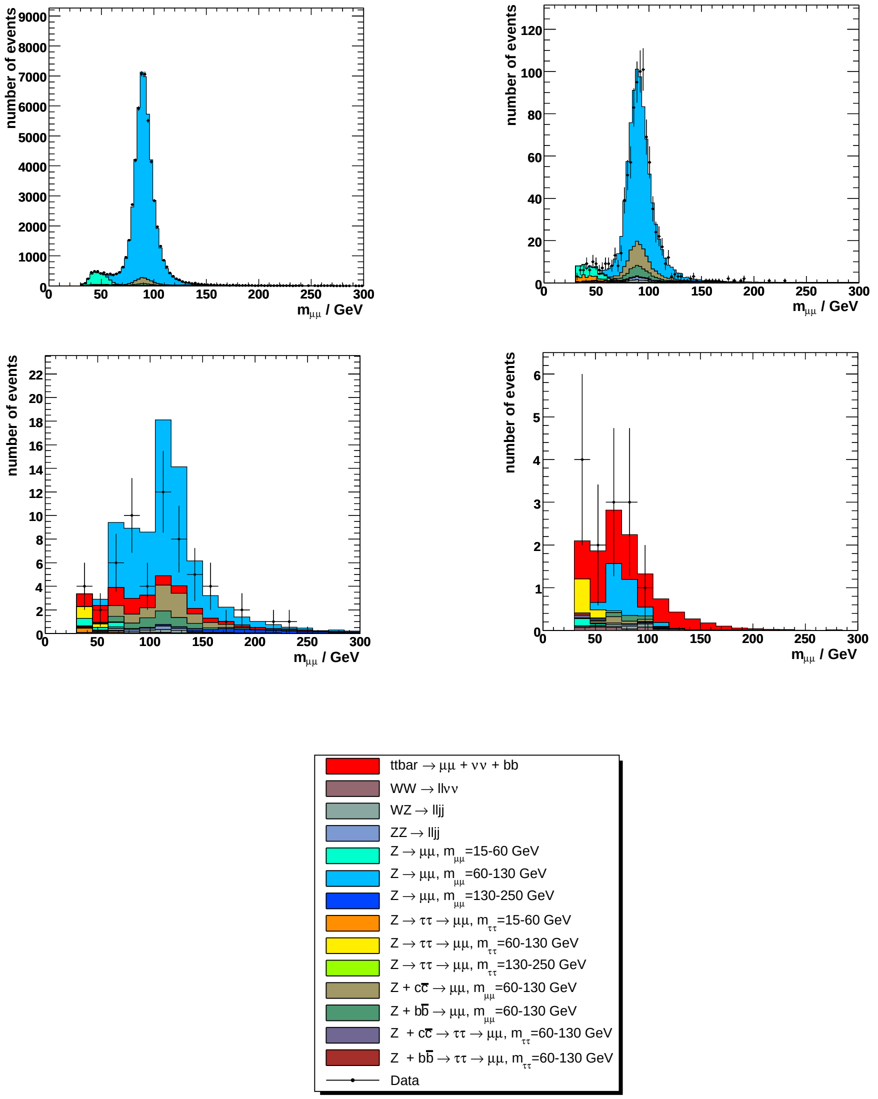

Figure 6.2.: Comparison plots showing the invariant dimuon mass for the following jet multiplicities: 0 jet inclusive (upper left plot), 2 jet inclusive (upper right plot), 2 jet inclusive after $\not\!\!E_T$ cut (lower left plot) and 2 jet inclusive after all cuts (lower right plot). Run IIa data were used. The integrated luminosity is 1096 pb^{-1}.

During this whole process several programming mistakes were found in the Run IIb code and the Run IIb software. The most important one was found in the $\not\!\!E_T$ significance algorithm (see Section 6.3.1). When comparing the efficiencies of this cut when using the old Run IIa software and the new Run IIb software a significant difference could be seen. With the Run IIb software the efficiency was about 10% while it was twice as high with the Run IIa software which led to the discovery of the mistake in the $\not\!\!E_T$ significance algorithm.

Some more programming mistakes were found in the selection code itself. At the beginning several additional events were found when using the new Run IIb code. Three of those events

Run Number	Event Number	$\not\!\!E_T$ significance using Run IIa software	$\not\!\!E_T$ significance using Run IIb software	|Difference|
210451	52746615	5.20045	5.21562	0.01517
203617	92145243	5.70112	5.68929	0.01183
208857	57048293	5.76461	5.76091	0.0037
204185	47294994	6.05855	6.00207	0.05648
194729	52983409	5.73574	5.72058	0.01516
175682	14649305	5.96597	5.92007	0.0459
206616	20036236	6.13875	6.04125	0.0975
204156	22975757	5.57673	5.61156	0.03483
205276	4549168	5.97096	5.93086	0.0401
213672	46600984	5.67879	5.65215	0.02264
213673	65182500	5.86994	5.81511	0.05483
214632	8844838	5.53843	5.44638	0.0925
193986	374796	5.55267	5.55197	0.0007

Table 6.2.: Events selected with the Run IIa code using Run IIa and Run IIb software. These events show small differences in the $\not\!\!E_T$ significance.

where due to the fact that in the new code jets from the intercryostat region where not removed in the very first version, which were removed in the old code for the Run IIa selection.
After this was fixed there were still differences in the jets used in the muon selection. This was discovered, because for three events only one muon was found that fulfilled all requirements (see Section 6.3.1), not two as was required. All available variables for the muons were compared in the new code and the old code. The values for the distance between muon and closest jet (dR(muon, closest jet)) was larger for some muons in the Run IIb code for three events:

- **run 210897, event 30105945:**
  leading muon, Run IIb code: dR(muon, closest jet) = 0.790982
  next to leading muon, Run IIb code: dR(muon, closest jet) = 1.44385
  leading muon, Run IIa code: dR(muon, closest jet) = 0.0463905
  next to leading muon, Run IIa code: dR(muon, closest jet) = 1.44385

- **run 178854, events 43267050:**
  leading muon, Run IIb code: dR(muon, closest jet) = 1.33717
  next to leading muon, Run IIb code: dR(muon, closest jet) = 1.06975
  leading muon, Run IIa code: dR(muon, closest jet) = 0.0694991
  next to leading muon, Run IIa code: dR(muon, closest jet) = 1.06975

- **run 196051, event 76064011:**
  leading muon, Run IIb code: dR(muon, closest jet) = 1.87275
  next to leading muon, Run IIb code: dR(muon, closest jet) = 1.86289
  leasing muon, Run IIa code: dR(muon, closest jet) = 1.66391
  next to leading muon, Run IIa code: dR(muon, closest jet) = 0.018076

Due to the isolation requirements only muons are selected that were not detected close to jets. All other variables were exactly the same in both codes. There was only one explanation: different jets were used for the muon isolation in the two codes which turned out to be true and

could be fixed.
However, it was possible to reproduce the Run IIa result (using Run IIb software) with the new Run IIb code except for two events. These two events were rejected when using the Run IIa code but were left with the Run IIb code, see Table 6.3. These differences are understood.
One of the two events was cut away in the Run IIb code when trigger matching was applied but was left with the Run IIa code. However, in the Run IIb code different triggers are used which explains the difference. In the Run IIa code the OR of the single muon triggers of trigger list versions v8 through v14 was used [45, 46], while for Run IIb preshutdown data the single muon trigger OR of a new triggerlist (version v15) was used. The OR means, that at least one of the triggers should accept the event. The triggers used in the Run IIa code and the Run IIb code are given in Table A.1. More on triggers can be found in Section 6.3.2. The second event was cut away in the Run IIb code due to the removal of luminosity block in which a part of the detector did not work properly. However, the lists of these luminosity blocks changed in the new software version.

Run Number	Event Number	
194068	19775580	
210451	52746615	*
203617	92145243	*
208857	57048293	*
204185	47294994	*
194729	52983409	*
167191	5718620	
175682	14649305	*
210371	32769425	
206616	20036236	*
204156	22975757	*
205276	4549168	*
211098	27229626	
213672	46600984	*
213673	65182500	*
214632	8844838	*
202850	*5060261*	
193986	*374796*	*

Table 6.3.: Events of the Run IIa dataset that are left with the Run IIb code and Run IIb software. The same events except the last two are also selected with the Run IIa code using Run IIb software. Those events marked with * are the 13 events that are selected in the original Run IIa selection.

To conclude, the differences between the Run IIa code and the Run IIb code are understood very well. Mainly the Run IIb code selects the same events as the Run IIa code. As a next step the Run IIb code was used with the Run IIb software to run on the Run IIb preshutdown dataset. This selection will be described in detail in Section 6.3.

6.3. Dimuon Selection for the Run IIb Preshutdown Dataset

6.3.1. Selection Cuts

As already explained in Section 2.2 in $t\bar{t}$ events two jets are expected as well as two muons, and two neutrinos. The neutrinos lead to a high missing transverse energy in the final state. The dimuon selection is now done to select those events out of all events that fit this pattern. In the following, the selection criteria used for the Run IIb preshutdown dimuon selection will be described. For the p17 dimuon selection the same cuts were applied (compare to the selection of Run IIa data [45]).
As already explained in Section 6.1.1 a skim of the Common Samples Group is used, which means, that very loose cuts on the p_T of the muons are already applied. Also, while data taking triggers are applied. This is necessary to decide which events should be written to tape (see Section 3.3).

- As a first step runs and luminosity blocks are removed, in which for some reason some part of the detector did not work properly. Additionally, a good event quality is required.
- A veto on standard electrons is done to be orthogonal to the $e\mu$ selection. For a standard electron the following requirements have to be fulfilled (see Section 4.2.2):
  - The electromagnetic fraction f_{EM} in the electromagnetic calorimeter is supposed to be larger than 0.9.
  - Isolated electromagnetic clusters.
  - A shower shape cut is done: $\chi^2 < 50$ (see Section 4.2).
  - p_T of the track is supposed to be larger than 5 GeV.
  - One track matched.
  - Electron likelihood > 0.85.
  - p_T of the electron is supposed to be larger than 15 GeV.
  - In the calorimeter electrons should not be detected in the forward region or in the intercryostat region: $|\eta_{cal}| < 1.1$ or $1.5 < |\eta_{cal}| < 2.5$.
- A standard selection for muons is performed. Muons have to fulfill the following requirements:
  - Muons which were detected in the bottom hole are rejected.
  - A veto on cosmic muons is done, because cosmic muons might fit the requirements for muons coming from a $t\bar{t}$ process. But cosmic muons cannot necessarily be matched to a bunch crossing. This information is used to veto cosmic muons.
  - Muons leave a track in the tracking system and are additionally detected in the muon system. It is required that a muon is matched to a track. For the track the following requirements are used:
    - $\chi^2_{track} < 4$.
    - for tracks with SMT hits: $|\mathrm{DCA}| < 0.02$ cm.
    - for tracks without SMT hits: $|\mathrm{DCA}| < 0.2$ cm.
  - All muons with a detector $|\eta|$ larger than 2 are rejected because only the region for $|\eta| < 2$ is covered by the tracking system and the muon system, as can be seen in Figure 3.3.

  - The muons are supposed to have a large transverse momentum. That is why all muons are rejected, that have a transverse momentum below 15 GeV. For the leading muon (muon with the highest p_T) a transverse momentum larger than 20 GeV is required.
  - Muons coming from a W decay are expected to be isolated. Thus all muons are rejected that are not isolated. For this two isolation requirements are used:
    - The muon should not be found in jets or close to jets. Thus the distance between muon and closest jet is required to be dR(muon,jet) > 0.5.
    - The muon should be isolated in the tracker. Within a cone around the track of the muon no additional high p_T tracks can be found ($etTrkConeScaledMin < 0.1$).
  - One muon is coming from the W^+ decay, the other one is coming from the W^- decay. Due to the conservation of electric charge the two muons in the final state of the top quark pair decay have to have opposite electric charges.
  - As a last step only events are selected that have at least two muons which fulfill all requirements.

- A standard jet selection is done with the following requirements:
  - Two high p_T jets are expected to be in the final state.
    - with jet energy scale correction: jet $p_T > 15$ GeV (see Section 4.2.1).
    - with jet energy scale correction and muon corrections: jet $p_T > 20$ GeV.
  - Jets in the forward region are rejected: $|\eta_{Det}| < 2.5$
  - For Monte Carlo jet smearing is applied (JSSR, [47])

- The following additional requirements involving jets are used:
  - The jet p_T (jet energy scale correction and muon corrections applied) of at least one jet has to be larger than 30 GeV.
  - Events with less than two jets fulfilling all requirements are rejected.

- A standard vertex selection is applied:
  - The primary vertex is required to lie within the tracking system. Therefore the $|z|$ position of the primary vertex should be smaller than 60 cm.
  - At least three tracks which are associated to the primary vertex have to exist.
  - The distance between the z of the primary vertex and the z of the muons should be smaller than one centimeter.

- Trigger selection, see Section 6.3.2.

- As already indicated a large missing transverse energy is expected due to the two neutrinos in the final state. By cutting on the missing transverse energy so that the $\not\!\!E_T$ is larger than 40 GeV a lot of background is rejected, because processes like $Z \rightarrow \mu\mu$ are not expected to have a large missing transverse energy.

- For further background rejection the $\not\!\!E_T$ significance algorithm is applied [48]. With this algorithm events with real $\not\!\!E_T$ are discriminated from events with mismeasured $\not\!\!E_T$, which can happen due to detector resolution effects. The energies of the objects in the event are fluctuated within the energy resolution and the $\not\!\!E_T$ resulting of this is calculated. A probability distribution for the $\not\!\!E_T$ is calculated which has a Gaussian form. For real missing transverse energy the width of the distribution tends to be smaller than for mismeasured missing transverse energy, although the measured missing transverse energy might be the same. The maximum of the distribution can be found close to the measured $\not\!\!E_T$. Two example probability distributions are shown in Figure 6.3 for real $\not\!\!E_T$ on the right hand side and for mismeasured $\not\!\!E_T$ on the left hand side. For mismeasured $\not\!\!E_T$ there is still a significant probability at $\not\!\!E_T = 0$. A likelihood is defined as

$$L = \log \frac{p(\not\!\!E_T = \text{max})}{p(\not\!\!E_T = 0)} = 2 \log \left(\frac{\not\!\!E_T}{2\sigma} \right)^2 , \tag{6.1}$$

where σ is the standard deviation of the probability distribution for the $\not\!\!E_T$. For real $\not\!\!E_T$ this likelihood should be larger than for mismeasured $\not\!\!E_T$. In Figure 6.4 two example likelihood distributions are shown. One can clearly see the differences between events with mismeasured $\not\!\!E_T$ (right hand side) and real $\not\!\!E_T$ (left hand side). For mismeasured $\not\!\!E_T$ the values of the likelihood are smaller than for events with real $\not\!\!E_T$.
In this selection the $\not\!\!E_T$ significance is required to be larger than 5. This way a large amount of Z background is rejected which is not expected to have a real large $\not\!\!E_T$.

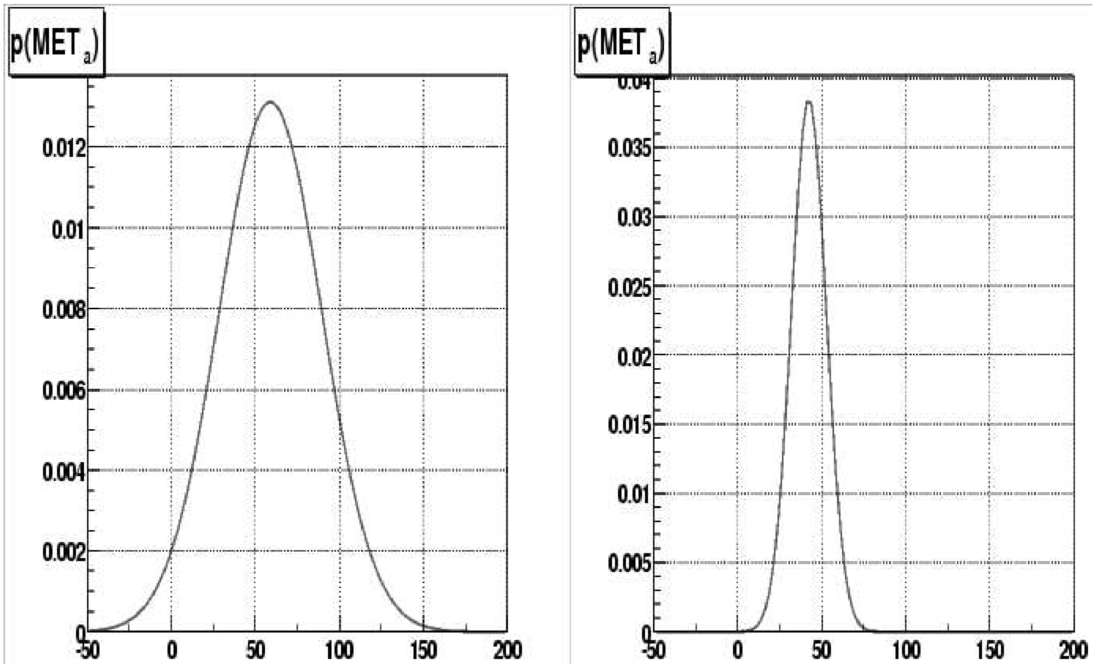

Figure 6.3.: Two examples for $\not\!\!E_T$ probability distributions are shown. The one on the left hand side is for mismeasured $\not\!\!E_T$. For $\not\!\!E_T = 0$ GeV the probability is different from zero. On the right hand side a distribution for real $\not\!\!E_T$ is shown. In this distribution the probability is almost zero at $\not\!\!E_T = 0$ GeV [48].

All cuts are also listed in the Tables 6.4 and 6.5, which contain the cut flows for each selection cut. For the $t\bar{t}$ Monte Carlo also the relative and overall efficiencies for each step of the selection are listed.

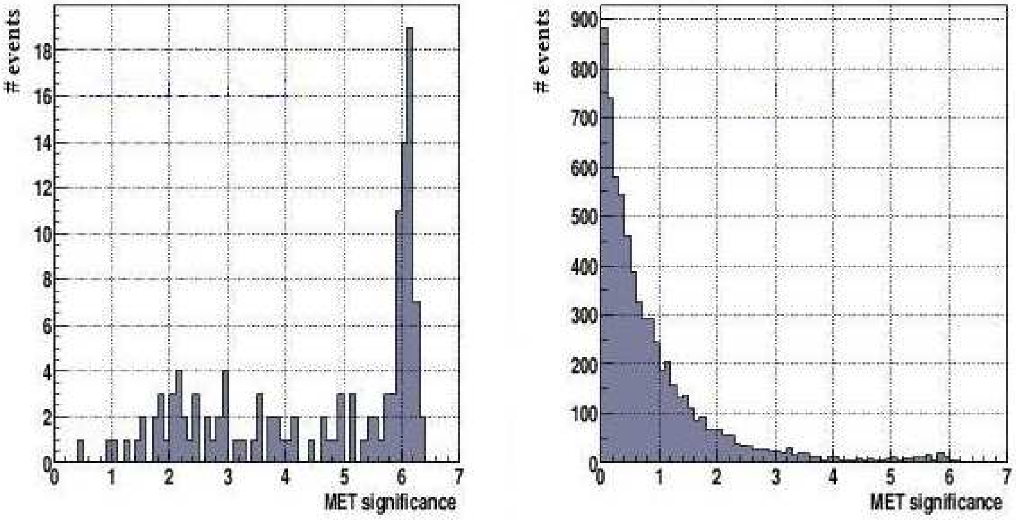

Figure 6.4.: $\not\!\!E_T$ likelihood distributions for mismeasured $\not\!\!E_T$ on the right hand side and for real $\not\!\!E_T$ on the left hand side. For real $\not\!\!E_T$ the distribution peaks at a high value, while the $\not\!\!E_T$ significances are smaller for mismeasured $\not\!\!E_T$ [48].

Selection	Events
Initial	99353
Remove bad runs and luminosity blocks	88679
Event quality	86093
Number of electrons ≤ 0	86036
muon selection: Muon out of bottom hole	86036
muon selection: Muon |detector eta| < 2.00	86036
muon selection: Muon quality is loose	86028
muon selection: Number of layers ≥ 0	86028
muon selection: Veto on cosmic muon	86028
muon selection: Matched with central track	86028
muon selection: Muon global fit chi square $< 4.000e+00$	86027
muon selection: DCA < 0.02 for nSMT > 0 and DCA < 0.2 for nSMT $= 0$	86027
muon selection: Muon pT ≥ 15 GeV	86026
muon selection: Track scaled isolation < 0.1	85833
muon selection: DeltaR(mu, jet) > 0.5	82732
muon selection: N muons ≥ 1	82732
muon selection: N muons ≥ 2	57515
Leading muon Pt > 20	55631
Invariant mass selection (opposite sign)	55216
Z of the first primary vertex (PV) < 60 cm	55216
N tracks for the first primary vertex ≥ 3	55216
dZ(muon, first PV) < 1 cm	54482
N jets ≥ 1	3321
N jets ≥ 2	733
$\not\!\!E_T \geq 40$ GeV	48
$\not\!\!E_T$ significance > 5	13

Table 6.4.: Cut flow for Run IIb data. Here “Initial” in the first line means the CSG sample was used as explained in Section 6.1.1.

6.3.2. Triggers

In the selection an OR of all single muon triggers (trigger version v15) is used, meaning that at least one of the single muon triggers must fire. The trigger efficiencies hardly show any

Selection	Events	Relative	Total
Initial	82607		
Remove bad runs and luminosity blocks	73773	89.3 ± 0.2 %	89.3 ± 0.1 %
Event quality	72597	98.4 ± 0.1 %	87.9 ± 0.2 %
Monte Carlo Scale Factor	72597	*0.1 ± 0.0*	
Luminosity reweighting:	72597	*1.2 ± 0.1*	
Beamweight	72597	*1.0 ± 0.1*	
Number of electrons ≤ 0	72521	99.9 ± 0.1 %	87.8 ± 0.2 %
muon selection: Muon out of bottom hole	72486	99.9 ± 0.1 %	87.7 ± 0.2 %
muon selection: Muon |detector eta| < 2.00	72480	99.9 ± 0.1 %	87.7 ± 0.2 %
muon selection: Muon quality is loose	71207	98.2 ± 0.1 %	86.2 ± 0.2 %
muon selection: Number of layers ≥ 0	71207	100.0 ± 0.0 %	86.2 ± 0.2 %
muon selection: Veto on cosmic muon	70495	99.0 ± 0.1 %	85.3 ± 0.2 %
muon selection: Matched with central track	69560	98.7 ± 0.1 %	84.2 ± 0.2 %
muon selection: Muon global fit chi square < 4.000e+00	68864	98.9 ± 0.1 %	83.4 ± 0.3 %
muon selection: DCA < 0.02 for nSMT > 0 and DCA < 0.2 for nSMT = 0	67633	98.2 ± 0.1 %	81.9 ± 0.2 %
muon selection: Muon pT $\geq$ 15 GeV	61682	91.2 ± 0.2 %	74.7 ± 0.2 %
muon selection: Track scaled isolation < 0.1	56258	91.2 ± 0.2 %	68.1 ± 0.2 %
muon selection: DeltaR(mu, jet) > 0.5	55214	98.2 ± 0.1 %	66.8 ± 0.2 %
muon selection: N muons ≥ 1	55214	100.0 ± 0.0 %	66.8 ± 0.2 %
muon selection: N muons ≥ 2	20114	36.4 ± 0.3 %	24.3 ± 0.2 %
Leading muon Pt > 20	19986	99.4 ± 0.1 %	24.2 ± 0.2 %
Muon Correction: mucorr	19986	*0.9 ± 0.1*	
Muon Correction: mutrack	19985	*0.9 ± 0.1*	
Invariant mass selection (opposite sign)	18826	94.2 ± 0.2 %	22.8 ± 0.2 %
Z of the first primary vertex < 60 cm	18639	99.0 ± 0.1 %	22.7 ± 0.2 %
N tracks for the first primary vertex (PV) ≥ 3	18627	99.9 ± 0.1 %	22.5 ± 0.2 %
dZ(muon, first PV) < 1 cm	18624	99.9 ± 0.1 %	22.5 ± 0.2 %
Triggerprobability	18624	*0.9 ± 0.1*	
after Trigger	18624	100.0 ± 0.0 %	22.5 ± 0.2 %
N jets ≥ 1	17412	93.5 ± 1.0 %	21.1 ± 0.2 %
N jets ≥ 2	13546	77.8 ± 0.4 %	16.4 ± 0.2 %
$\not\!\!E_T \geq 40$ GeV	10119	74.7 ± 1.0 %	12.2 ± 0.2 %
$\not\!\!E_T$ significance > 5	8801	86.9 ± 1.3 %	10.7 ± 0.2 %

Table 6.5.: Cut flow and the relative and overall efficiencies for signal Monte Carlo. The efficiencies are not corrected by the event weights. Corrected overall efficiency is 4.03 ± 0.76 %. Here, "Initial" in the first line means the CSG sample was used as described in section 6.1.1.

p_T dependence above the turn-on threshold. Therefore only the dependencies in η and φ are used. The trigger efficiencies for different trigger subversions are shown in figure 6.5. A list of all triggers can be found in the right column of Table A.1. Each of the triggers consist of one or more scripts for each trigger level. Each script contains the requirements for the muons such as the minimum p_T and in which subdetectors how many hits should haven been detected. One example is given in the following. The other triggers are similar. The descriptions for all triggers can also be found in [49].

MUHI1_TK12_TLM12:

- **L1:** Requires one muon, tight scintillator requirements, loose wire requirements, matched to CTT (central track trigger) track with $p_T > 13$ GeV.
- **L2:** The Or of two scripts is used:
  - One muon, medium quality, tight scintillator timing cut, $p_T > 3$ GeV.
  - One track found by STT (silicon track trigger) (good fit quality), $p_T > 20$ GeV.

- **L3:** Requires at least one loose muon with $p_T > 0$ GeV, at least one global track with $p_T > 12$ GeV using SMT and CFT, muon candidate with 12 GeV threshold matched to a loose central track.

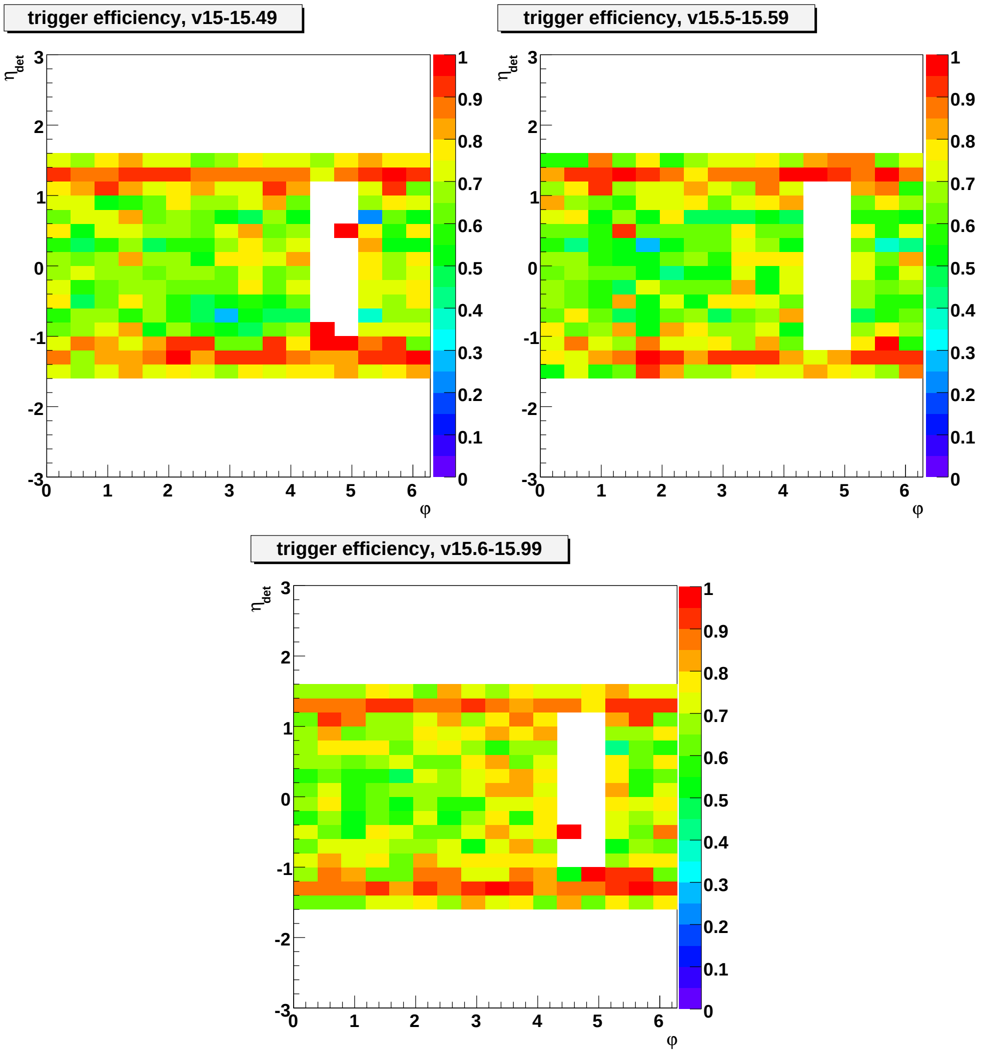
trigger efficiency, v15-15.49

trigger efficiency, v15.5-15.59

trigger efficiency, v15.6-15.99

Figure 6.5.: Trigger efficiencies for the OR of single muon triggers for three subversions of trigger version 15.

6.3.3. Corrections

The following corrections are applied:

- Z boson p_T reweighting. With the Z boson p_T reweighting the agreement between data and Monte Carlo is getting much better as can be seen in Figure 6.6 [50].
- Luminosity profile reweighting.
- Muon id efficiency correction [51] and jet id efficiency corrections [52].

- Trigger turn on corrections.
- Jet energy scale corrections of jets (see Section 4.2.1) [53, 54].
- Muon corrections of jets (see Section 4.2.1).

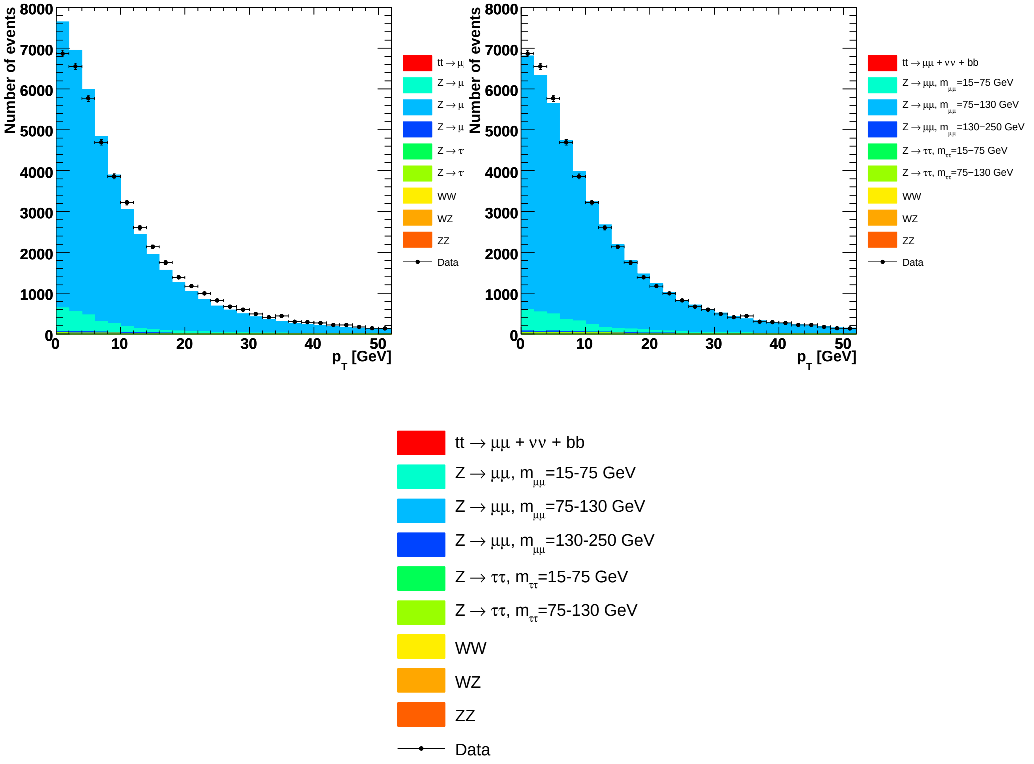

Figure 6.6.: Z boson p_T before (left) and after (right) p_T reweighting in the zero jet inclusive plots. The integrated luminosity for these plots is 1216 pb^{-1}.

6.3.4. Fake Muons

Fake muons are muons which are fake isolated. To determine the number of fake muons only data are used. It is done with the so-called matrix method [45]. Two samples are needed, a ”tight” one, for which the normal selection is used, and a ”loose” sample which is the normal selection where only one muon has to be isolated and there are no requirements for the other muon. As described in Section 6.3.1 a muon is isolated if the sum of the track p_Ts around the muon track is less than 10% of the muon track p_T, and if the muon is not found close to or within jets. In Figure 6.7 a scatter plot is shown which contains the values for these two criteria. The dashed lines indicate where cuts are made. All events left of the vertical dashed line ($dR(\text{muon, closest jet}) > 0.5$) are cut away as well as all events above the horizontal dashed line ($etTrkConeScaledMin < 0.1$).

In the loose sample there are N_L events left and in the tight sample N_T events. These numbers are related to the signal and background yields

$$N_L = N^{Z+top} + N^{W+QCD} \tag{6.2}$$

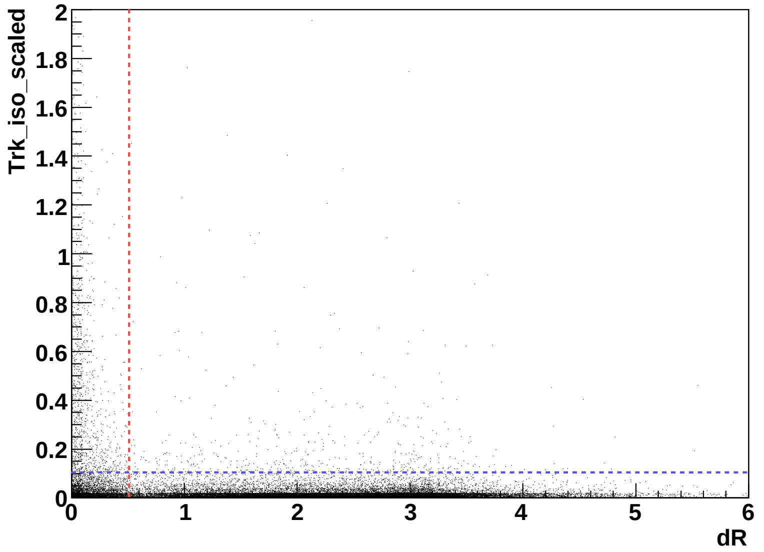

Figure 6.7.: Scatter plot showing the values for dR(muon, closest jet) and *etTrkConeScaled* for each event in data. The Run IIb selection was used, but no isolation criteria were used for the muons. The dashed lines indicate where isolation cuts are done.

and

$$N_T = \varepsilon_{sig} N^{Z+top} + f_\mu N^{W+QCD} \tag{6.3}$$

where ε_{sig} is the signal efficiency of the muon isolation cut and f_μ is the fake rate. N^{Z+top} is the number of events from Z-processes and $t\bar{t}$ events. All these events are expected to have two isolated muons in the final state. N^{W+QCD} is the number of events from QCD background and W-processes. These events are expected to have less than two isolated muons in the final state. With the equations given in equations 6.2 and 6.3 the number of fake muons can be calculated:

$$N_{fake} = f_\mu \frac{N_T - \varepsilon_{sig} N_L}{f_\mu - \varepsilon_{sig}}. \tag{6.4}$$

The only unknown parameters are ε_{sig} and f_μ which can be determined from the data sample. For the signal efficiency a sample enriched with Z events and $t\bar{t}$ events is used. This is done by a cut on the dimuon invariant mass. Only events with an invariant mass larger than 70 GeV and smaller than 110 GeV are used, which is the region around the Z peak at 90 GeV. For the signal efficiency ε_{sig} one defines a tag muon, which is the isolated leading muon. Then one looks for a second muon without any isolation criteria (probe muon) and counts in how many cases the second muon is isolated. Then the signal efficiency can be calculated by

$$\varepsilon_{sig} = \frac{N^{iso}_{probe}}{N^{iso}_{tag}}. \tag{6.5}$$

The fake rate f_μ is determined in a similar way. In this case a sample of events is used in which as few real isolated muons are present as possible. Only events are taken into account which have a dimuon invariant mass smaller than 70 GeV, which means the Z peak is cut off. Now a tag muon is defined as a nonisolated next-to-leading muon and the probe muon now as the leading muon without any isolation criteria. Then it is counted again in how many cases the second muon is isolated. The fake rate is then calculated with

$$f_\mu = \frac{N^{iso}_{probe}}{N^{noniso}_{tag}}. \tag{6.6}$$

This is done for different jet multiplicities.
The calculation of the signal efficiency and the fake rate is always done before the topological cuts ($\not\!\!E_T$ cut and $\not\!\!E_T$ significance cut). After the topological cuts statistics is too low to get a reliable result. For this reason in the two jet bin and after all cuts the values for f_μ and ε_{sig} determined without the last two cuts ($\not\!\!E_T$ cut and $\not\!\!E_T$ significance cut) are used to determine N_{fake} (see Table 6.6).
The results for signal efficiency, fake rate as well as N_{fake} are summarized in Table 6.6. Additionally, the number of events in the loose and in the tight sample are given. After all cuts the number of fake muons is

$$N_{fake} = 0.84 \pm 0.22.$$

Jet Multiplicity	f_μ	ε_{sig}	N_L	N_T	N_{fake}
0 jet incl	0.080 ± 0.012	0.892 ± 0.007	53266 ± 231	4435 ± 211	305.41 ± 62.90
1 jet incl	0.040 ± 0.009	0.830 ± 0.022	4691 ± 69	3315 ± 58	29.36 ± 8.76
2 jet incl	0.030 ± 0.004	0.746 ± 0.041	1109 ± 34	733 ± 28	3.99 ± 2.35
2 jet incl + topological cuts	0.030 ± 0.004	0.746 ± 0.041	44 ± 7	13 ± 4	0.84 ± 0.22

Table 6.6.: Results of fake rate determination for all jet multiplicities. f_μ is the fake rate, ε_{sig} the signal efficiency, N_L and N_T the number of events in the loose and tight sample, respectively, and N_{fake} the number of fake muons.

6.3.5. Comparison Plots and Event Yields

The dimuon selection is performed for data as well as Monte Carlo. Here the signal Monte Carlo needs special treatment. The code expects to have Monte Carlo for the dimuon channel only. In reality it is an inclusive sample, containing all dilepton channels. This would lead to an overall selection efficiency which is too low, which again would lead to a wrong $t\bar{t}$ production cross section. To avoid this at the beginning of the selection only those events are chosen which contain two muons coming from a W decay and where the W boson is coming from a top quark decay. Another possibility to get the correct cross section but without doing this step is to take into account the fact that an inclusive sample was used via the branching ratio.
The number of events left after selected cuts are listed in the yield table which can be found in Table 6.7, namely after all cuts but without cut on the number of jets and without $\not\!\!E_T$ cut and $\not\!\!E_T$ significance cut, after requiring at least two jets but no $\not\!\!E_T$ cut and $\not\!\!E_T$ significance cut, after all cuts but the $\not\!\!E_T$ significance cut and after all cuts. This table is a summary of the more detailed tables which can be found in Appendix C. The tables in the appendix also contain the efficiencies of the cuts. In Table 6.7 the second column shows the event yields for data, in the other columns the yields for Monte Carlo are given. In the fourth column the yields for the signal Monte Carlo are shown. As can be seen in the last line of this column about 7 events are expected to be $t\bar{t}$ events. In data, after all cuts 13 events are selected, which is close to the 12.67 events left for total Monte Carlo, as can be seen in the last line of Table 6.7. This leads to

an expected background of 5.45 events. All events and the most important kinematic variables are listed in Table 6.8. As can be seen in the table all events have two high p_T muons and at least two high p_T jets, a high $\not\!\!E_T$ and a $\not\!\!E_T$ significance larger than 5.

When comparing the yields for the $Z \rightarrow \mu\mu$ process and the yields for the signal process, which can be found in Appendix C, one can see that rather a lot of the signal is kept while the $Z \rightarrow \mu\mu$ background is reduced strongly. This is exactly what the selection should do and therefore is another proof that the code for the Run IIb dimuon selection is correct.

To get good statistics Monte Carlo are produced with much more events than there are in the data. To compare data and Monte Carlo Simulation the Monte Carlo has to be scaled to the data. The best way to do this is to scale it according to the integrated luminosity and the cross sections of each process. This method was used for the yield tables as well as the comparison plots. The cross sections for the background processes and the signal process are given in Table 6.1. However, there are other methods like normalizing to the Z peak. But the disadvantage is, that mistakes in the selection might not be discovered.

	Data	total MC	Signal Monte Carlo
inclusive	47738 ± 218	47205.30 ± 217.27	14.55 ± 3.81
1 jet excl	2572 ± 51	2662.98 ± 51.60	2.99 ± 1.74
2 jet incl	726 ± 27	575.47 ± 23.99	10.78 ± 3.28
2 jet after MET cut	45 ± 7	38.88 ± 6.24	8.03 ± 2.84
2 jet after topological cut	13 ± 4	12.67 ± 3.56	7.22 ± 2.69

Table 6.7.: Event yields for the dimuon selection for data, total Monte Carlo and signal Monte Carlo after various jet cuts as well as after the $\not\!\!E_T$ cut and the $\not\!\!E_T$ significance cut.

Run Number	Event Number	Leading Muon p_T in GeV	Second Muon p_T in GeV	number of jets	Leading jet p_T in GeV	Second jet p_T in GeV	$\not\!\!E_T$ in GeV	$\not\!\!E_T$ sig
229944	23887784	82.844	24.885	2	61.607	24.038	84.326	5.222
231051	492022	82.052	30.963	3	130.813	28.228	67.232	5.610
227011	25523259	66.230	25.026	2	46.629	35.361	74.231	5.757
224433	26062436	47.012	15.939	2	114.435	24.098	126.807	5.758
224680	17546555	55.351	15.440	2	170.029	116.465	91.739	5.439
230927	26093923	65.262	28.229	2	117.979	78.875	52.362	5.869
232268	8756794	74.075	33.367	2	55.988	42.334	59.576	5.487
224988	25329981	22.102	16.056	3	94.150	24.384	56.155	5.791
233560	29143876	76.034	50.810	2	103.059	51.054	79.830	5.672
233332	31713184	56.149	19.018	2	71.777	49.190	111.231	5.776
227936	1619966	54.303	38.248	2	76.256	42.158	49.078	5.075
230078	27085827	40.149	37.890	2	62.105	41.319	62.039	5.832
234429	5438049	24.159	23.687	2	61.763	34.455	57.870	5.883

Table 6.8.: Basic kinematics for candidate events, p_Ts and $\not\!\!E_T$s are given in GeV.

The cut flows for data and $t\bar{t}$ Monte Carlo are shown in Table 6.4 and Table 6.5, respectively. In the first column the selection cut is given and in the second column the number of events after each step of the selection. The number in the first line is the number of events coming from the skim. In Table 6.5 also the efficiencies for each of the selection cuts are given, but not corrected by event weights yet. The overall efficiency after all cuts with the correction for the event weights is 4.03 ± 0.76 %.

Some data-Monte Carlo comparison plots are shown in Figures 6.8, 6.9, 6.10, and 6.11. More comparison plots are added in Appendix D. Comparison plots are shown in the inclusive bin where no requirements for the number of jets were applied and in the two jet inclusive bin in which only events are taken into account that have at least two high p_T jets. Additionally, to these two plots, plots in the two jet inclusive bin after the $\not{E}_T$ cut are shown as well two jet inclusive plots after all cuts.

The comparison plots basically show a good agreement. However, there is a rather big discrepancy for small $\not{E}_T$ which is not understood yet (see Figure 6.9). This discrepancy can also be seen in the yield Table 6.7. Especially in the two jet inclusive bin the discrepancy is rather large taking the uncertainties into account. But events with small $\not{E}_T$ are cut away so the result after all cuts should be correct.

In the comparison plots the different Monte Carlo samples are shown in different colors. The $Z \to \mu\mu$ background is shown in shades of blue, the $Z \to \tau\tau$ background in shades of green, the diboson background in shades of yellow and orange and the signal in red. The different jet multiplicities were added to one background, so they are not listed individually. The fake muon background is not included yet but it is a low background compared to the others and would hardly be seen anyway.

As expected, especially the inclusive plots are mainly showing blue, as expected, because $Z \to \mu\mu$ is expected to be the largest background The other backgrounds are small compared to this one. The red signal can hardly be seen in the inclusive plots. After applying more cuts (requiring at least two jets, cutting on $\not{E}_T$ and $\not{E}_T$ significance) the $Z \to \mu\mu$ background is reduced and the signal becomes visible in the comparison plots.

An interesting plot to look at is the plot showing the value for $\not{E}_T$ significance likelihood. This plot is shown in Figure 6.12 for the two jet inclusive plot after the $\not{E}_T$ cut. The background is already reduced so that the signal can be seen clearly. As expected, the $Z \to \mu\mu$ background can mainly be found at low $\not{E}_T$ significances, while the $t\bar{t}$ distribution peaks somewhere between 5.5 and 6. The $\not{E}_T$ significance cut is done at 5 as indicated with the dashed line in Figure 6.12. Everything below 5 is cut away. This way indeed a lot of $Z \to \mu\mu$ is rejected, which is the purpose of this cut.

6.4. $e\mu$ Selection for the Run IIb Dataset

Not only for the dimuon channel but also for the $e\mu$ channel and for the dielectron channel selections are made to obtain a $t\bar{t}$ enriched sample. In the following only the $e\mu$ selection will be described briefly [55]. Those events selected were used for the mass measurement which is described in Section 6.7.2

The datasets used for the $e\mu$ selection are similar to those used for the dimuon selection. In the $e\mu$ channel $Z \to \tau\tau$ is the largest background process. To simulate the background Alpgen [37] Monte Carlo is used for Z background and signal ($t\bar{t} \to e\mu jj$). For the diboson backgrounds (WW, WZ) Pythia[38] Monte Carlo is used. In the $e\mu$ selection similar selection cuts are used as in the dimuon selection. The only difference is, that here an electron is required. First data quality is applied. In the events at least two jets (coming from the two bottom quarks)

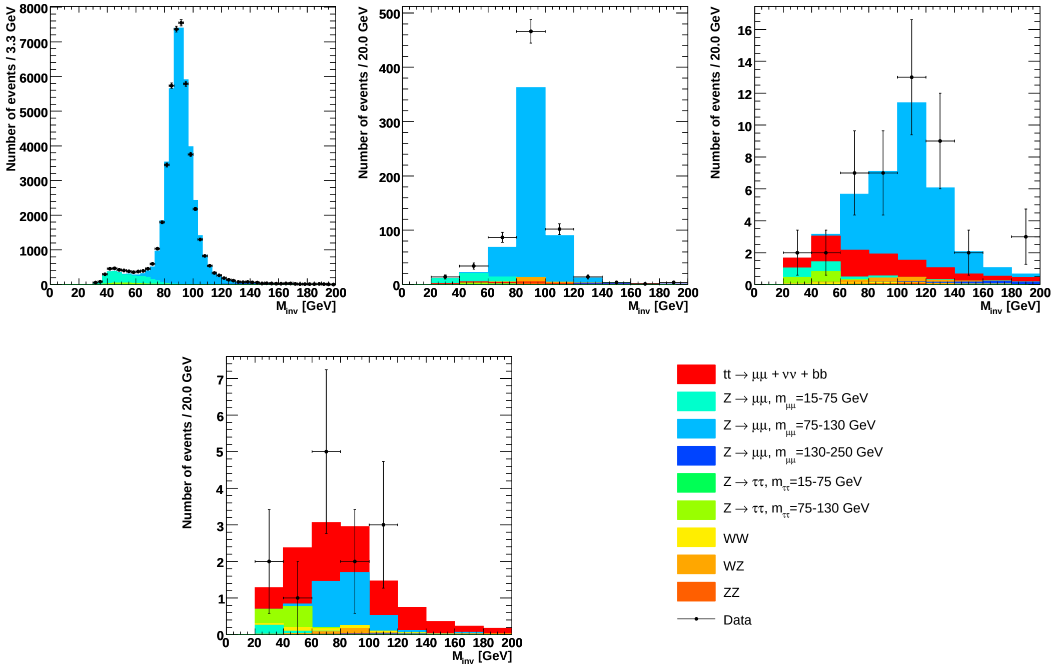

Figure 6.8.: Comparison plots showing the dimuon invariant mass for 0 jet inclusive (left plot in the upper row), 2 jet inclusive (the plot in the middle of the upper row), 2 jet inclusive after $\not\!\!E_T$ cut (right plot in the upper row) and 2 jet inclusive after all cuts (bottom left). The integrated luminosity is 1216 pb^{-1}.

should be found. The jet p_T is supposed to be larger than 20 GeV in case muon corrections were applied. Without muon corrections the p_T has to be larger than 15 GeV. Furthermore exactly one electron matched to a track is required. At least one muon is needed with $p_T >$ 15 GeV. The muon should be matched to a medium track and be isolated in the calorimeter as well as in the tracker. Additionally, the charge of the electron and the leading muon should have opposite signs. A standard vertex selection is performed which is the same as in the dimuon selection. Additionally, a cut at $H_T > 115$ GeV is done (for definition of H_T see Section 2.3) as well as a cut on the electron likelihood (see Section 4.2.2) which should be larger than 0.85. As a correction Z boson p_T reweighting is applied.

	Data	total MC	Signal	$Z \to \tau\tau$	Diboson
0 jet incl	1072	$1110.4^{+80.4}_{-97.7}$	$52.9^{+2.5}_{-2.8}$	$631.1^{+28.6}_{-60.0}$	$86.3^{+17.6}_{-17.7}$
2 jet incl	84	$74.2^{+6.7}_{-6.3}$	$38.2^{+2.0}_{-2.1}$	$14.3^{+1.5}_{-2.0}$	$2.5^{+0.6}_{-0.6}$
2 jet incl after likelihood cut 0.85	50	$40.6^{+2.1}_{-2.3}$	$32.4^{+1.7}_{-1.8}$	$3.7^{+0.5}_{-0.6}$	$1.4^{+0.3}_{-0.3}$

Table 6.9.: Yield table for Run IIb $e\mu$ selection. The Run IIb preshutdown dataset was used [44].

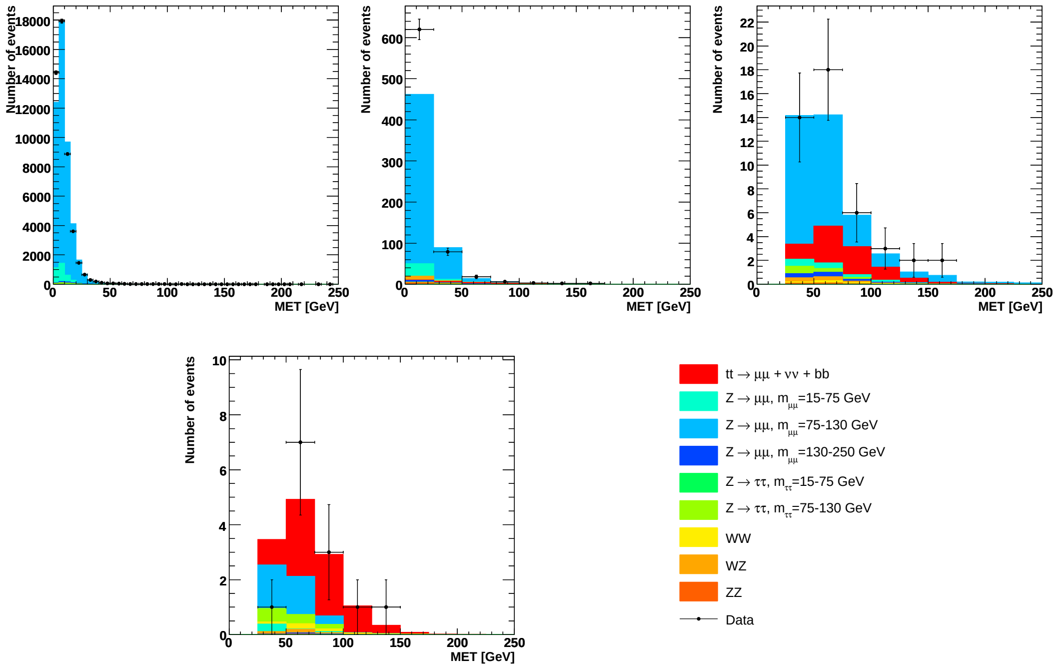

Figure 6.9.: Comparison plots showing the missing transverse energy for 0 jet inclusive (left plot in the upper row), 2 jet inclusive (the plot in the middle of the upper row), 2 jet inclusive after $\not\!\!E_T$ cut (right plot in the upper row) and 2 jet inclusive after all cuts (bottom left). The integrated luminosity is 1216 pb^{-1}.

	Data	total MC	Signal	$Z \rightarrow \tau\tau$	Diboson
0 jet incl	437	$501.8^{+34.9}_{-43.7}$	$25.3^{+1.2}_{-1.3}$	$301.9^{+13.7}_{-28.7}$	$41.3^{+8.4}_{-8.5}$
2 jet incl	38	$36.3^{+4.6}_{-4.0}$	$18.3^{+1.0}_{-1.1}$	$6.8^{+0.8}_{-1.0}$	$1.2^{+0.3}_{-0.3}$
2 jet incl after likelihood cut 0.85	18	$19.2^{+1.1}_{-1.2}$	$15.5^{+0.8}_{-0.9}$	$1.7^{+0.3}_{-0.3}$	$0.7^{+0.2}_{-0.2}$

Table 6.10.: Yield table for Run IIb $e\mu$ selection. The Run IIb posthutdown dataset was used [44].

After all cuts there are 50 events left for the Run IIb preshutdown dataset and 18 for the Run IIb postshutdown dataset. Tables 6.9 and 6.10 contain the yields for the $e\mu$ selection after selected cuts for the Run IIb preshutdown and the Run IIb postshutdown dataset.

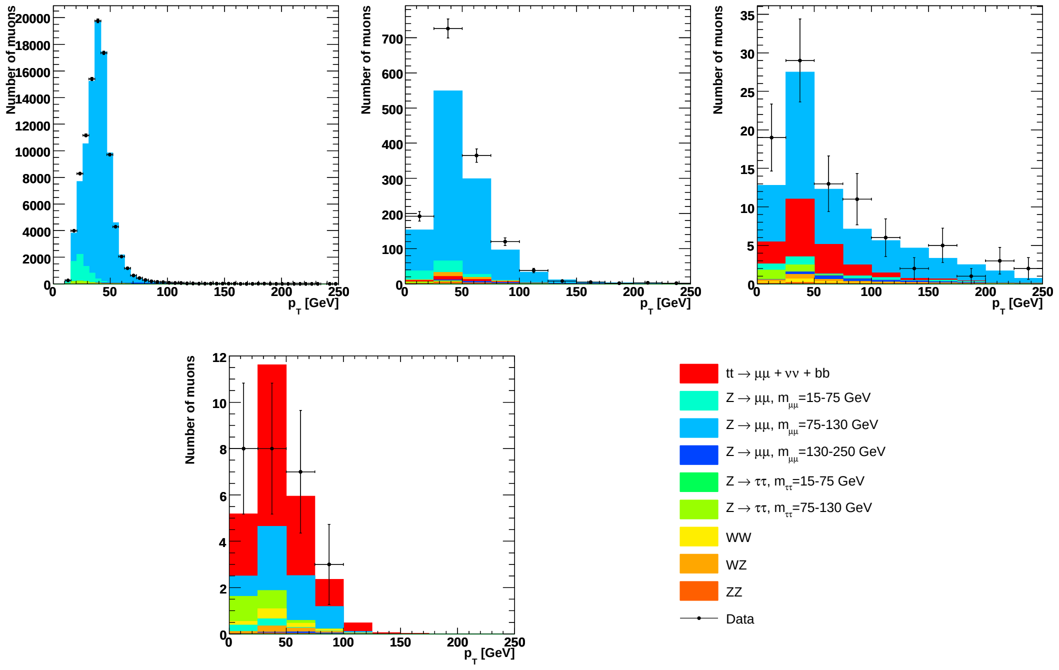

Figure 6.10.: Comparison plots showing the p_T of the two muons for 0 jet inclusive (left plot in the upper row), 2 jet inclusive (the plot in the middle of the upper row), 2 jet inclusive after $\not\!\!E_T$ cut (right plot in the upper row) and 2 jet inclusive after all cuts (bottom left). The integrated luminosity is 1216 pb^{-1}.

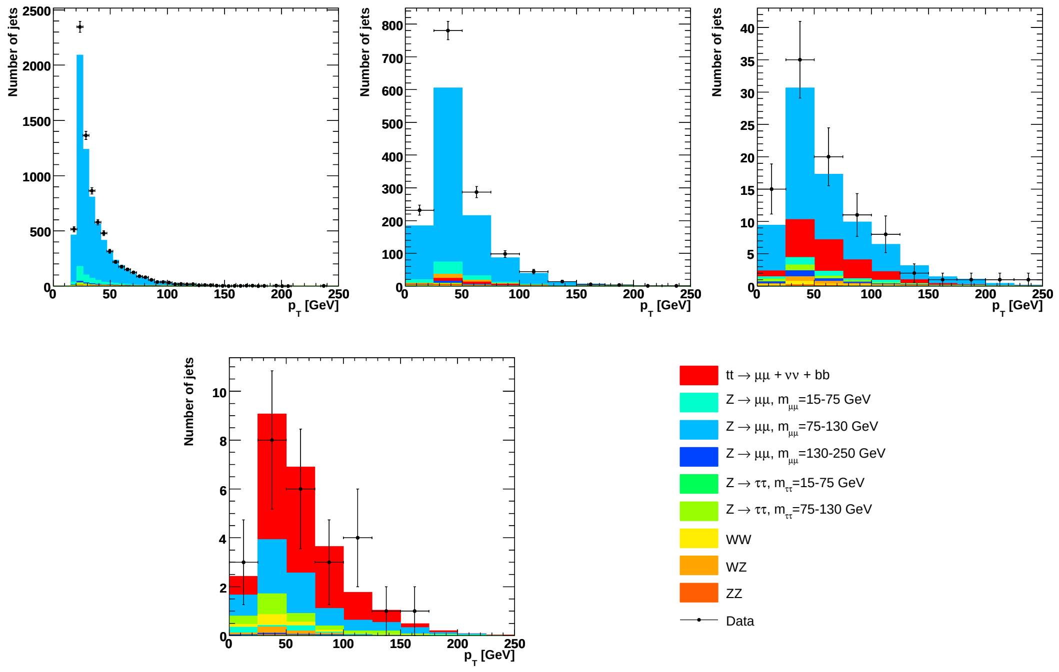

Figure 6.11.: Comparison plots showing the p_T of the two jets for 0 jet inclusive (left plot in the upper row), 2 jet inclusive (the plot in the middle of the upper row), 2 jet inclusive after $\not\!\!E_T$ cut (right plot in the upper row) and 2 jet inclusive after all cuts (bottom left). The integrated luminosity is 1216 pb^{-1}.

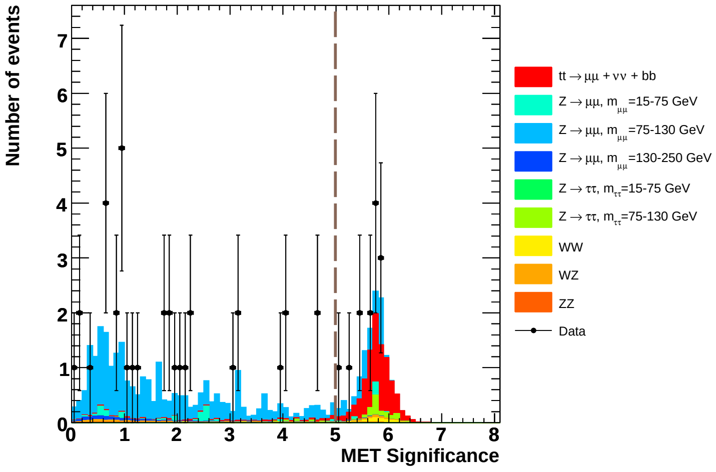

Figure 6.12.: $\not\!\!E_T$ significance in the two jet inclusive bin after the $\not\!\!E_T$ cut. The dashed line indicates where the $\not\!\!E_T$ significance cut is going to be applied. Everything lower than 5 will be cut away.

6.5. Production Cross Section measured in the Dimuon Channel

After the dimuon selection all ingredients are available to measure the production cross section. The cross section can be calculated by

$$\sigma = \frac{N_{Data} - N_{bkg}}{\mathcal{L}\varepsilon br(t\bar{t} \rightarrow \mu\bar{\mu})}, \tag{6.7}$$

where N_{Data} is the number of data left after all cuts. From this number the expected number of background events N_{bkg} is subtracted. The expected background (N_{bkg}) consists of the number of background events from the process described in Section 6.3 and the number of fake muons, which was determined in Section 6.3.4. $\mathcal{L}$ is the integrated luminosity, ε the corrected overall selection efficiency for signal and $br(t\bar{t} \rightarrow \mu\bar{\mu})$ the branching ratio for two top quarks both decaying into a muon. The values for each variable are given in Table 6.11. The $t\bar{t}$ production cross section is now calculated to be

$$\sigma = 8.53 \pm 3.02 \text{ (stat.)pb.}$$

This is in agreement with the theoretical prediction [14]

$$\sigma_{theo} = 6.77 \pm 0.42 \text{ pb.}$$

N_{Data}	13 ± 4
N_{bkg}	5.45 ± 2.33
N_{fakes}	0.84 ± 0.22
$\mathcal{L}$	1215.85 pb^{-1}
ε	0.0403 ± 0.0076
$br(t\bar{t} \rightarrow \mu\bar{\mu})$	0.01607

Table 6.11.: Numbers used to calculate the $t\bar{t}$ production cross section.

6.6. Top Quark Mass Measurement with Neutrino Weighting

6.6.1. The Neutrino Weighting Method

In the final state of the dimuon channel of $t\bar{t}$ decay there are six particles (two bottom quarks, two charged leptons, and two neutrinos, see Section 2.2). Each of these particles has a 4-momentum which results in 24 degrees of freedom. The momenta of four of the six particles (the bottom quarks and the charged leptons) are measured in the detector which reduces the number of unknown degrees of freedom to twelve. In addition, the masses of the particles in the final state are known. So there are only six unknown degrees of freedom left. The $\not{E}_T$ components in x- and y-direction can be determined which leads to only four degrees of freedom. There are three more constraints due to the conservation of the invariant masses of particles:

$$\begin{aligned} m_{W^-} &= m_{l^-\overline{\nu}} \\[2em] m_{W^+} &= m_{l^+\nu} \\[2em] m_t &= m_{\overline{t}} \\ \Rightarrow m_{l^+\nu b} &= m_{l^-\overline{\nu}\overline{b}} \end{aligned}$$

This leads to one unknown degree of freedom that is still left. The system is kinematically underconstrained.

There are possibilities how to determine the mass in such systems. One method is the neutrino weighting method [56].

In this method certain values for the neutrino η as well as the top quark mass are chosen to calculate the p_T components of the two neutrinos. To do this, the two equations for the invariant masses of the W boson and the top quark are used:

$$m_W^2 = (E_l + E_\nu)^2 - (\vec{p}_l + \vec{p}_\nu)^2 \tag{6.8}$$

$$m_t^2 = (E_l + E_\nu + E_b)^2 - (\vec{p}_l + \vec{p}_\nu + E_b)^2 \tag{6.9}$$

In these equations the energy and the momentum of the neutrino are unknown. After performing a Lorentz-boost along the z-direction in such a way that the neutrino momentum in z direction is zero and using the equation

$$p_{T,\nu}^2 = p_{\nu,x}^2 + p_{\nu,y}^2 \tag{6.10}$$

the system of equations can be solved for the transverse components of the neutrino momentum. The result is of the form

$$p_{\nu,x} = b - \frac{ad}{2c} \pm \frac{a}{2c} \cdot \sqrt{d^2 - 2cf} \tag{6.11}$$

$$p_{\nu,y} = -\frac{d}{2c} \pm \frac{1}{2c} \cdot \sqrt{d^2 - 2cf}, \tag{6.12}$$

where a, b, c, d, e and f are

$$\begin{aligned} a &= \frac{E^{'}_b p_{l,y} - E^{'}_l p_{b,y}}{E^{'}_l p_{b,x} - E^{'}_b p_{l,x}} \\ b &= \frac{E^{'}_l (m_t^2 - m_W^2 - m_b^2 - 2p_l p_b) - E^{'}_b m_W^2}{2(E^{'}_b p_{l,x} - E^{'}_l p_{b,x})} \\ c &= -\left(\frac{p_{l,x}}{E^{'}_l} a + \frac{p_{l,y}}{E^{'}_l}\right)^2 + a^2 + 1 \\ d &= 2ab - 2\left(\frac{p_{l,x}}{E^{'}_l} a + \frac{p_{l,y}}{E^{'}_l}\right)\left(\frac{m_W^2}{2E^{'}_l} + \frac{p_{l,x}}{E^{'}_l} b\right) \\ f &= b^2 - \left(\frac{m_W^2}{2E^{'}_l} + \frac{p_{l,x}}{E^{'}_l} b\right)^2 . \end{aligned} \tag{6.13}$$

This is not only done for the neutrino but also for the antineutrino.
In a next step for each chosen pseudorapidity and top quark mass the calculated values for $p_{\nu,x}$ and $p_{\nu,y}$ are compared to the measured values and a weight w_i is calculated from

$$w_i = \exp\left(\frac{-\not{E}_{T\,x} - p_{\nu,x} - p_{\overline{\nu},x}}{2\sigma_{\not{E}_x}}\right) \cdot \exp\left(\frac{-\not{E}_{T\,y} - p_{\nu,y} - p_{\overline{\nu},y}}{2\sigma_{\not{E}_y}}\right), \tag{6.14}$$

where i stands for one of the possible solutions of neutrino momentum components. There is a total of up to eight solutions. Four of them are coming from equations 6.11 and 6.12. Additionally, there is an ambiguity due to the two bottom quarks in the final state. No charge measurement is performed. Therefore it is not known which jet was produced by the bottom quark and which one by the antibottom quark. That is why a total of up to eight solutions is possible. A weight function is now defined as

$$W(m_t) = \sum_{\eta_\nu,\eta_{\overline{\nu}}} \sum_{i=1}^{8} w_i P(\eta_\nu, m_{top}^{MC}) P(\eta_{\overline{\nu}}, m_{top}^{MC}). \tag{6.15}$$

There are ten η assumptions for each simulated top quark mass and for neutrino and antineutrino each. The ηs are chosen in such a way, that each η range is as likely as the others. Practically this means that the η ranges have different sizes. The integral of the η distribution (which has a Gaussian form) over each η range is the same. The weights are summed over all pseudorapidity values of the neutrinos as well as over all possible solutions for neutrino momentum solutions. This weight function only depends on the top quark mass. The weights are calculated for data as well as signal and background Monte Carlo. PYTHIA Monte Carlo is used for various top quark masses between 155 GeV and 200 GeV. Each event delivers exactly one weight function.

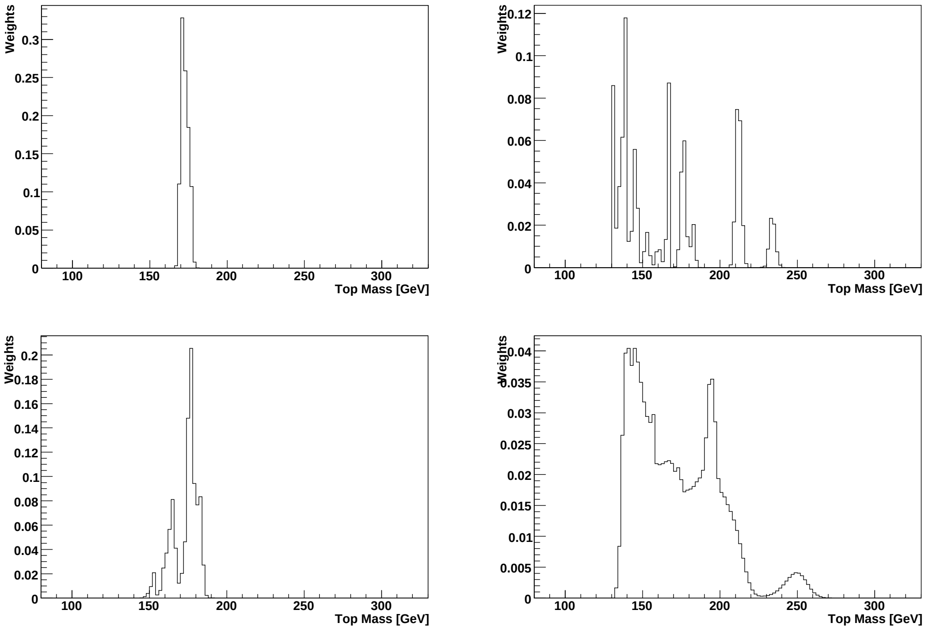

Figure 6.13.: Weight functions for four different events. Signal Monte Carlo for m_{top} = 170 GeV was used.

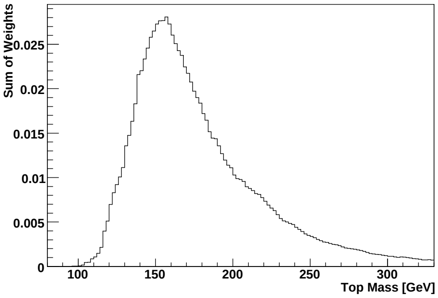

Figure 6.14.: The sum of all weight functions for a simulated top quark mass of m_{top} = 170 GeV. Although each weight function looks spiky the sum of them looks smooth again.

Examples are shown in Figure 6.13. These functions can look spiky which is due to the sum over all possible solutions. Each solution has its own maximum and therefore its own most likely top quark mass. But when adding all weight functions the distribution looks smooth again (see Figure 6.14).

Now there are different possibilities how to proceed. The easiest way to extract the top quark mass is the maximum method [57, 58]. The top quark mass for each event is reconstructed by taking the maximum of the weight function belonging to that event, which is supposed to be the most likely top quark mass. For all events the reconstructed top quark mass is filled into a histogram. This is done for various simulated top quark masses separately. This leads to a two dimensional distribution. To smoothen it, a two-dimensional fit is done. The data are compared to the fitted function with a maximum likelihood method. This delivers the measured top quark mass.

However, in this thesis not the maximum method will be presented, but the mean-rms method [58, 59]. This is a similar method, but the result is expected to be more precise because one additional variable is used. Instead of the maximum of the weight functions the mean is used as reconstructed top quark mass. As an additional variable the rms of the weight function is used.

Signal

For the signal this leads, taking various simulated top quark masses into account, to a three dimensional distribution instead of the two dimensional distribution. This three dimensional weight distribution is fitted with the analytic function given in Equation 6.16, which has 14 parameters (p_0, ..., p_{14})[1]:

$$\begin{aligned} f_s(mean_i, rms_i|m_{top}) = & \frac{(rms_i + p_{14})^{p_7} \cdot \exp\left(-p_8(rms_i + p_{14})^{p_9}\right)}{\int\limits_0^\infty [(x + p_{14})^{p_7} \cdot \exp\left(-p_8(x + p_{14})^{p_9}\right)]dx} \\ & \times \left[\frac{1 - p_{10}}{\sqrt{2\pi}(p_3 + p_4(rms_i - 36) + p_5(m_{top} - 175))}\right. \\ & \times \exp\left(\frac{-[mean_i - (p_0 + p_1(rms_i - 36) + p_2(m_{top} - 175))]^2}{2 \cdot [p_3 + p_4(rms_i - 36) + p_5(m_{top} - 175)]^2}\right) \\ & \left. + \left\{\begin{matrix} 0 & ; & mean_i < \frac{p_0 + p_1(rms_i - 36) + p_2(m_{top} - 175)}{p_{11}} \\ f(m_{top}, mean_i, rms_i) & ; & else \end{matrix}\right\}\right], \end{aligned} \tag{6.16}$$

where

$$\begin{aligned} f(m_{top}, mean_i, rms_i) = & p_{10} \cdot \frac{p_{12}^{(1+p_{13})}}{\Gamma(1 + p_{13})} \times \left(mean_i - \frac{p_0 - p_1(rms_i - 36) + p_2(m_{top} - 175)}{p_{11}}\right)^{p_{13}} \\ & \times \exp\left(-p_{12}\left[mean_i - \frac{p_0 - p_1(rms_i - 36) + p_2(m_{top} - 175)}{p_{11}}\right]\right). \end{aligned}$$

The measured top quark mass is obtained by a maximum likelihood method.

Background

In the data sample not only $t\bar{t}$ events are present but also background events. This has to be taken into account when doing the mass measurement. To do so weight functions are calculated for the background events and the mean-rms method is applied. But here only a two dimensional fit is necessary to get a smooth distribution. There is no simulated top quark mass for background events, only the mean and the rms of the weight functions. The fit function has seven parameters (p_0, ...,p_6) and reads

$$\begin{aligned} f_b(mean_i, rms_i) = & \frac{1}{p_0} \cdot \exp\left(-\frac{1}{2}\cdot\right. \\ & \left.((p_1 \cdot mean_i + p_2 \cdot rms_i - p_3)^2 + (p_4 \cdot mean_i + p_5 \cdot rms_i - p_6)^2)\right). \end{aligned} \tag{6.17}$$

Maximum Likelihood Method

To determine the top quark mass from data an unbinned likelihood is used. It consists of three parts. A Poisson part makes sure that, within Poisson fluctuation, the number of background events and the number of signal events is consistent with the number of events observed in the data sample. A Gaussian part is used so that the number of background events and the number

---

[1] For historical reasons there is no parameter p_6.

of expected background events (see table C) is the same within the allowed fluctuations. The last part contains the top quark mass dependence. In this part the fit functions for signal and background as described above can be found again. The likelihood depends on the top quark mass, the number of signal events n_s and the number of background events n_b:

$$\mathcal{L}(n_s, n_b, m_{top}) = \underbrace{\frac{(n_s+n_b)^N \exp -(n_s+n_b)}{N!}}_{Poisson} \times \underbrace{\frac{1}{\sqrt{2\pi}\sigma_b} \exp \frac{-(n_b-\overline{n}_b)^2}{2\sigma_b^2}}_{Gauss} \times \underbrace{\prod_{i=1}^{N} \frac{n_s f_s(mean_i, rms_i|m_{top}) + n_b f_b(mean_i, rms_i)}{n_s+n_b}}_{mass\ dependence}. \tag{6.18}$$

Combination of Channels

To combine both channels ($e\mu$ and $\mu\mu$) the likelihoods for each channel are multiplied and then the maximum is calculated, the mass measurement for the ee channel is not presented in this thesis and currently investigated by the DØ Top Group. However, in reality the negative logarithm of the likelihood is minimized. Instead of multiplying the likelihoods the logarithms of the likelihoods are added. The combined likelihood depends on m_{top}, $n_s^{e\mu}$, $n_b^{e\mu}$, $n_s^{\mu\mu}$, and $n_b^{\mu\mu}$.

6.6.2. Ensemble Testing

An ensemble testing is performed. This is used for the calibration of the measured value for the top quark mass. Out of the background pool events are drawn randomly according to the yields. The number of background events is Poisson distributed. Then $t\bar{t}$ Monte Carlo events are drawn from the signal pool in such a way that the total number of events in the ensemble matches the number of events in data. With this simulated sample the mass measurement is done. For each simulated top quark mass 300 ensembles are created. With this a calibration curve can be calculated. On one axis the simulated top quark mass is plotted, on the other one the reconstructed top quark mass. The reconstructed top quark mass is expected to be the same as the simulated top quark mass. Therefore the calibration curve should be a line with a slope of one and an offset of zero. Examples for such calibration curves can be found in Section 6.7. The pull is defined as

$$pull = \frac{m_{top} - m_{top}^{sim}}{\sigma_{m_{top}}}, \tag{6.19}$$

where $m_{top} \pm \sigma_{m_{top}}$ is the reconstructed top quark mass and m_{top}^{sim} is the simulated top quark mass. This is done to cross check the estimated uncertainties for the measured top quark mass. The pull distribution is expected to have a mean of zero and a rms of one. When the width of the pull distribution is larger than one the statistical uncertainty is underestimated, when the width is smaller than one the statistical uncertainty in overestimated.

6.7. Results

6.7.1. Dimuon Channel

Fit of the Signal Monte Carlo

As a first step the three dimensional fit for the signal was performed. The fit function depends on the generated top quark mass, the mean of the weight functions, and the rms of the weight functions. The fit function is given in Equation 6.16. Plots showing this function can be found in Figures 6.15, 6.16 and 6.17. Additional plots can be found in Appendix E. To plot the function the parameters in Equation 6.20 were used, which were determined by the fit. The first figure contains the plots for a constant generated top quark mass of 170 GeV, the second one shows the function for a constant mean of 175 GeV, the last one for a constant rms of 33 GeV. The left plots show the distributions coming directly from the weight functions, the right plots show the fitted function. In Figure 6.17 one can see that the reconstructed top quark mass (the mean of the weight functions) depends on the generated top quark mass as expected. The fit converges with the following parameters:

$$\begin{aligned}
p_0 &= 196.5 \pm 0.2 \\
p_1 &= 1.317 \pm 0.006 \\
p_2 &= 0.603 \pm 0.008 \\
p_3 &= 23.26 \pm 0.09 \\
p_4 &= 0.183 \pm 0.005 \\
p_5 &= 0.180 \pm 0.007 \\
p_7 &= 0.550 \pm 0.006 \\
p_8 &= 0.0001134 \pm 0.0000007 \\
p_9 &= 2.554 \pm 0.002 \\
p_{10} &= 0.347 \pm 0.007 \\
p_{11} &= 1.428 \pm 0.003 \\
p_{12} &= 0.0526 \pm 0.0003 \\
p_{13} &= 2.17 \pm 0.02 \\
p_{14} &= 0.047 \pm 0.069.
\end{aligned} \tag{6.20}$$

The result of this fit is sufficient, one obtains $\frac{\chi^2}{ndf} = 2.6$. The parameters and their uncertainties are reasonable as well. Only for p_{14} some additional work could be done because the uncertainty of that parameter is larger than the parameter itself. However, there is no systematic uncertainty coming from the large uncertainties of the parameters or the choice of the function. The only reason why the fit is done is to get a smooth function which shows correlation between mean and m_{top}. After the mass measurement a calibration of the measured value is done. These corrections are small compared to the statistical uncertainty.

Background Fit

The background function is given in Equation 6.17 in Section 6.6.1. It depends on the mean and the rms of the weight functions and has seven parameters. The fit converges and for the

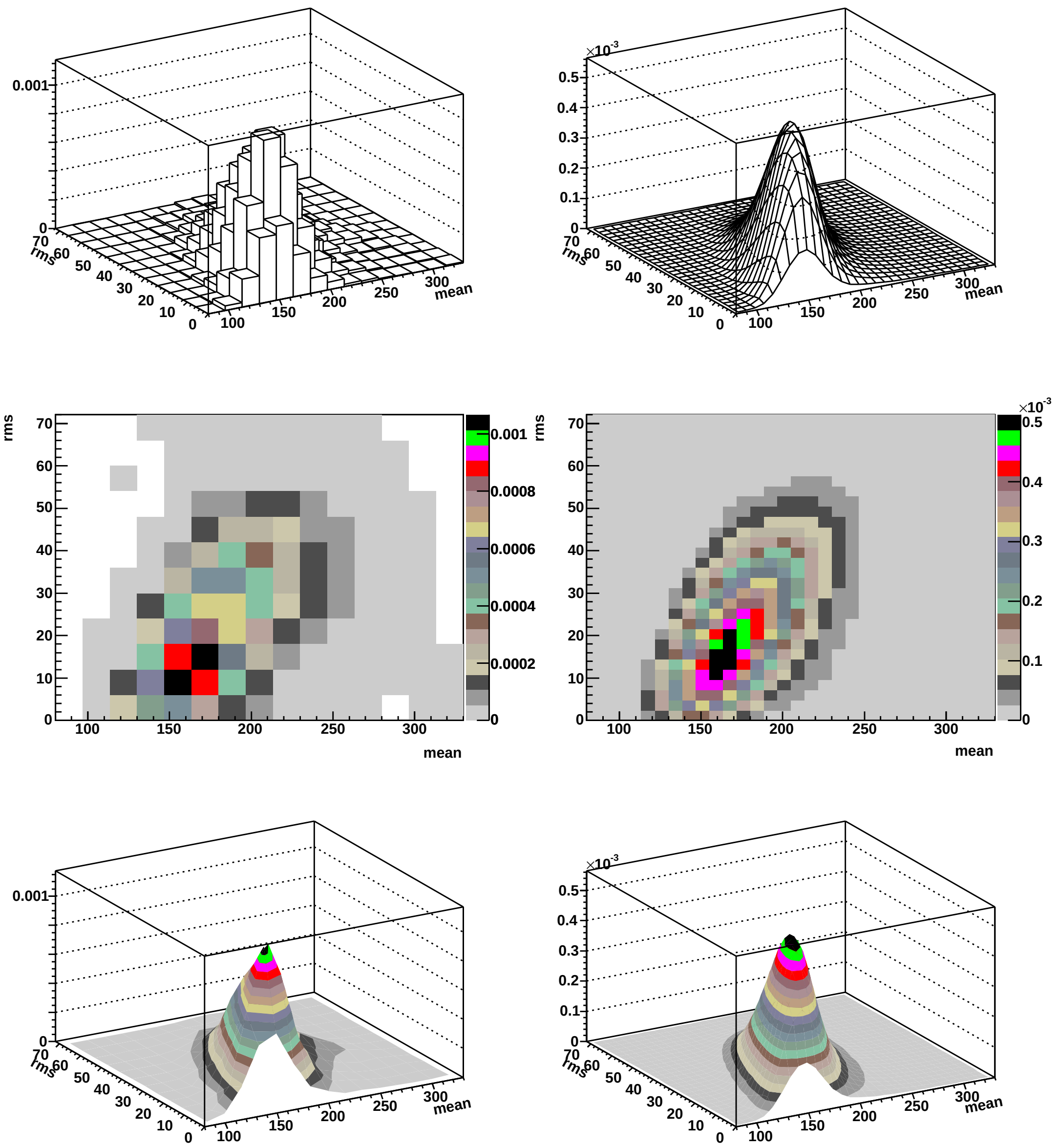

Figure 6.15.: Signal fit function for $m_{top} = 170$ GeV in the dimuon channel. In the plots on the left hand side the distribution coming from the neutrino weighting, in the plots on the right hand side the fitted function is shown.

parameters the following values are obtained:

$$\begin{aligned} p_0 &= 1133 \pm 290 \\ p_1 &= 0.055 \pm 0.002 \\ p_2 &= -0.073 \pm 0.008 \\ p_3 &= 7.8 \pm 0.2 \\ p_4 &= -0.004 \pm 0.007 \\ p_5 &= 0.055 \pm 0.009 \\ p_6 &= 0.85 \pm 1.1. \end{aligned} \tag{6.21}$$

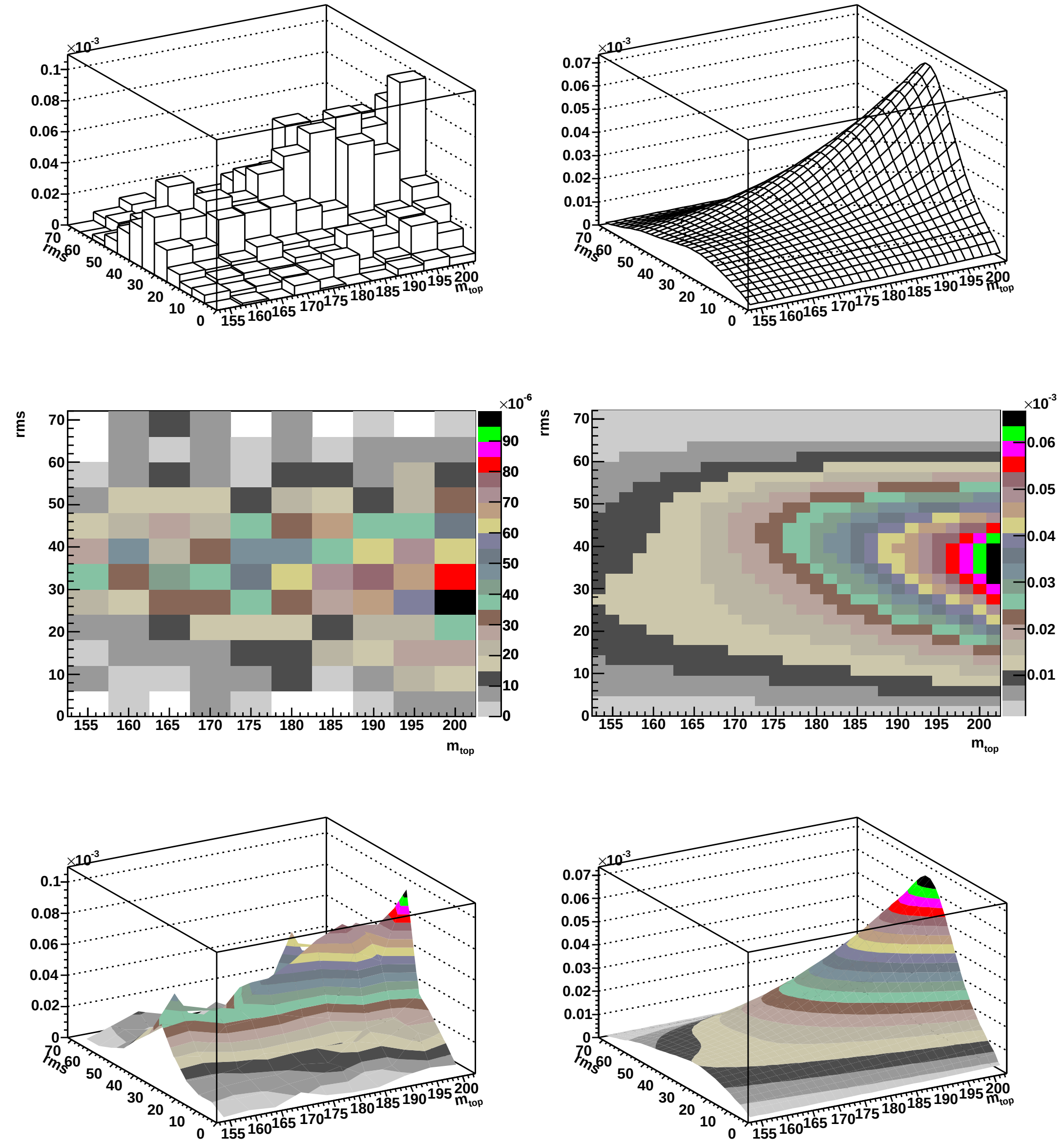

Figure 6.16.: Signal fit function for mean = 175 GeV in the dimuon channel. In the plots on the left hand side the distribution coming from the neutrino weighting, in the plots on the right hand side the fitted function is shown.

For parameters p_4 and p_6 the uncertainty is larger than the value itself. So here some more work is still to be done. The fit is not as good as for the signal and one gets $\frac{\chi^2}{ndf} = 5.4$. A plot of the fit function for background in the dimuon channel can be found in Figure 6.18. As for the signal distribution the plots on the left hand side show the distribution coming directly from the neutrino weighting, the plots on the right hand side show the fitted function.

Systematic uncertainties are mainly due to the low statistics but also due to the choice of the fit function.

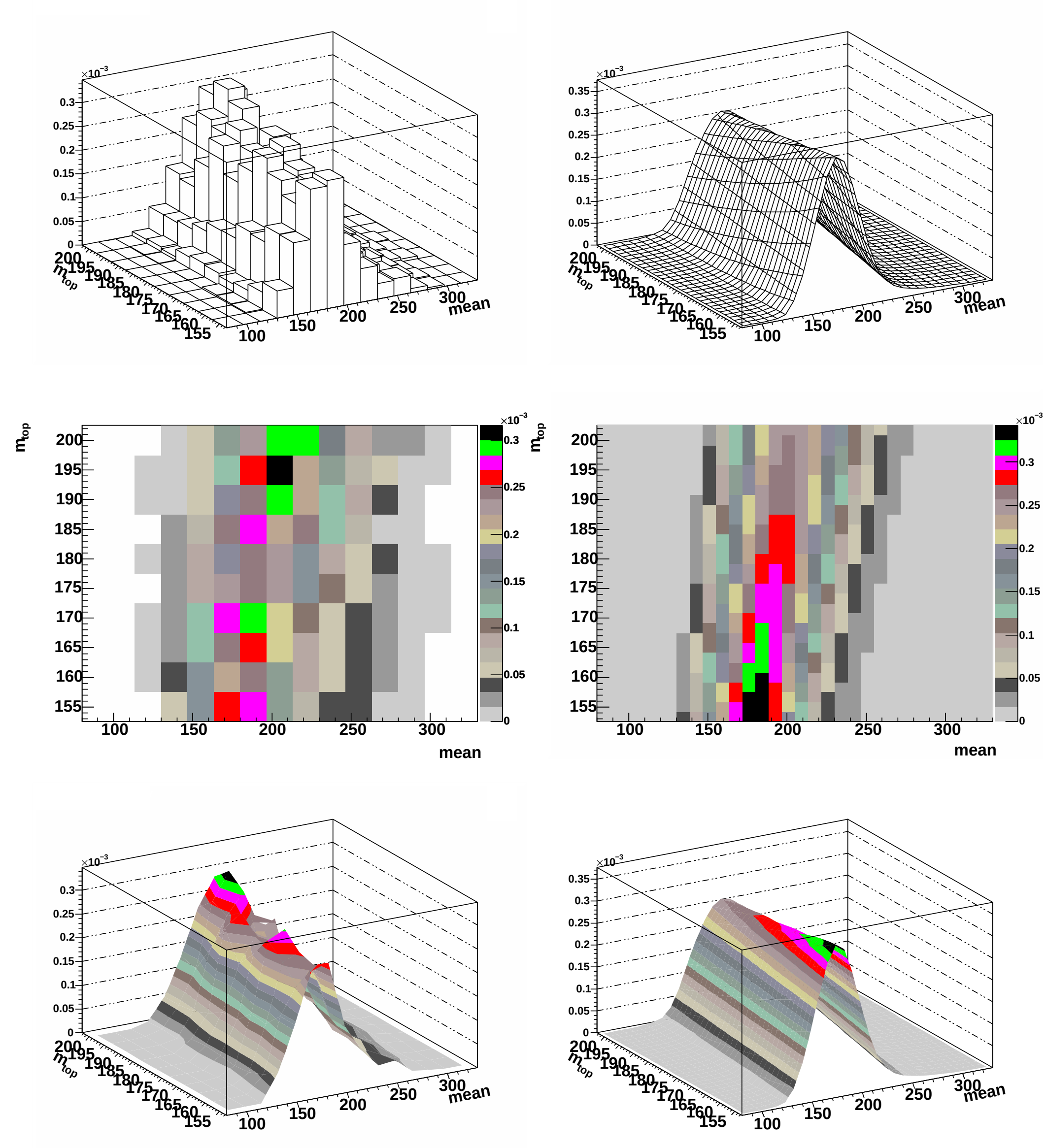

Figure 6.17.: Signal fit function for rms = 33 GeV in the dimuon channel. In the plots on the left hand side the distribution coming from the neutrino weighting, in the plots on the right hand side the fitted function is shown.

Ensemble Testing

After the fits for signal and background have been done successfully an ensemble testing is performed. For this 300 ensembles are created for each simulated top quark mass as described in Section 6.6.2. The likelihood method as described in Section 6.6.1 is used for each of the ensembles to determine a top quark mass. The equation for the likelihood is given in Equation 6.18. For each simulated top quark mass the measured top quark masses obtained by the ensemble testing are filled into a histogram and the uncertainty of the measured top quark mass is filled

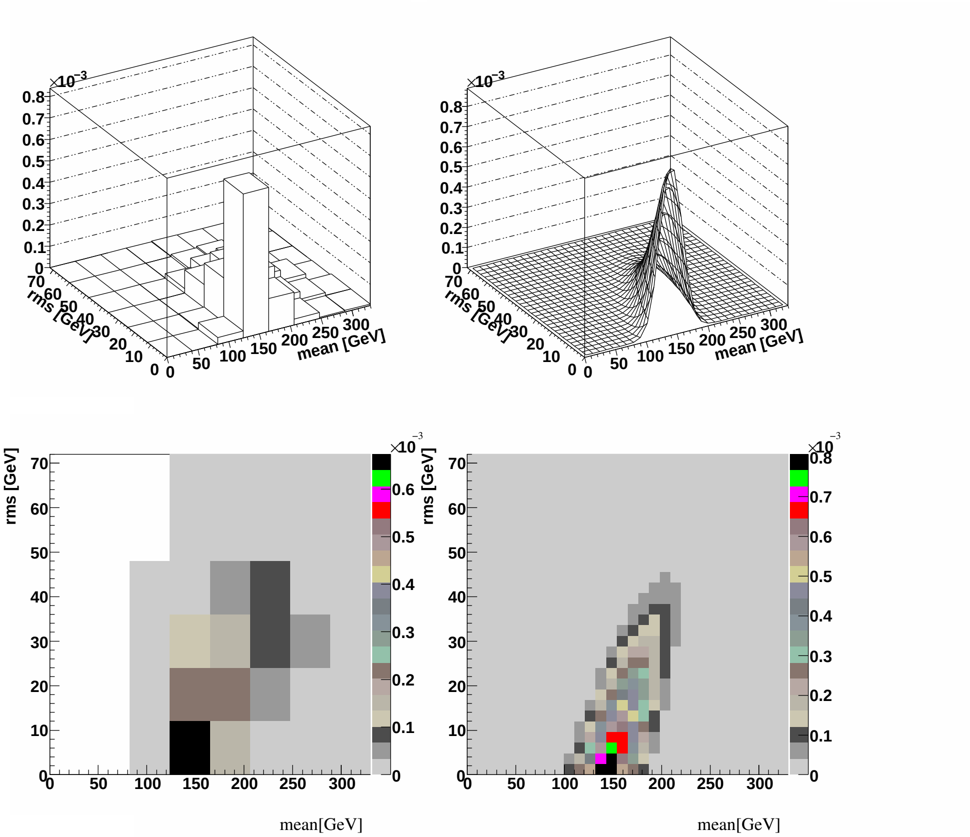

Figure 6.18.: Function fitted to the background for the dimuon channel. The two plots on the left hand side show the distribution coming from the neutrino weighting. The plots on the right hand side show the fitted function.

into a second histogram. These histograms are useful to compare the measured top quark mass and its uncertainty to the results coming from the ensemble testing (see Figure 6.22).
Then the calibration curve is calculated. The mean of the output top quark masses calculated in the ensemble testing is plotted for each simulated top quark mass. Then a line is fitted to the entries. For the dimuon channel the curve is shown in Figure 6.19 on the left hand side. On the x-axis the input top quark mass minus 175 GeV is plotted, on the y-axis the output top quark mass minus 175 GeV. It shows an offset of 1.5 ± 0.5 GeV and a slope of 0.8 ± 0.04. As expected the offset is close to zero and the slope is close to one. However, there is a positive offset which means that the estimated top quark mass is biased due to the signal probability distribution. This is taken into account by a calibration. The corrections due to the calibration are small compared to the statistical uncertainty. In Figure 6.19 a second calibration curve is shown on the right hand side. In this plot the output top quark mass minus the input top quark mass is plotted against the input top quark mass minus 175 GeV. It is expected that both, input top quark mass and output top quark mass are the same. Therefore the slope and the offset are expected to be zero. However, the offset for this calibration curve is 1.5 ± 0.5 GeV and the slope is -0.2 ± 0.04. The pull was calculated for each mass bin. Plots containing the mean and the width of the pull distribution for each simulated top quark mass are shown in Figure 6.20. The mean of the pull is expected to be zero, the width is expected to be one. As can be seen in the

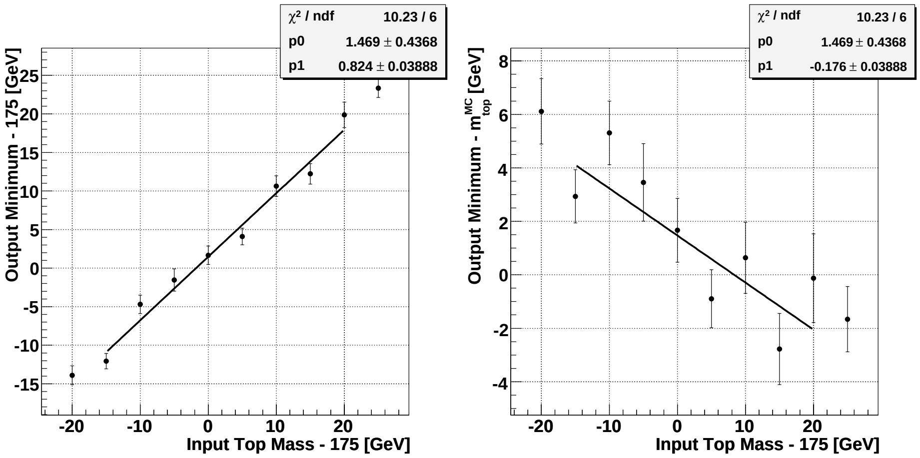

Figure 6.19.: Calibration curves for the dimuon channel.

plots the pull mean is -0.2 ± 0.03 while the pull width is 1.1 ± 0.03. The pull width is larger than one, therefore the statistical uncertainty of the measured top quark mass is underestimated.

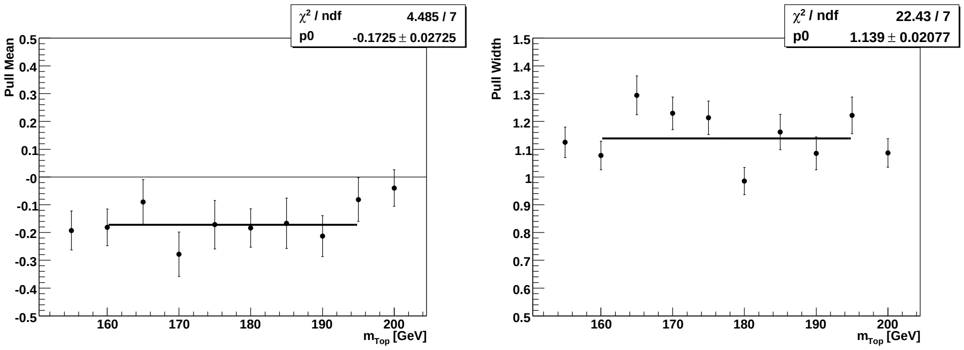

Figure 6.20.: Pull mean on the left hand side and the pull width on the right hand side for the dimuon channel.

Mass Measurement

After the ensemble testing the likelihood method is used for the data sample and a top quark mass is determined, which is the measured top quark mass. The uncalibrated result is

$$m_{top,RunIIb,\mu\mu}^{measured} = 173.6 \pm 12.7 \text{ GeV}.$$

The negative logarithm of the likelihood as a function of the top quark mass m_{top} at n_s and n_b of the minimum is shown in Figure 6.21.

As a next step this measured value for the top quark mass has to be corrected according to the calibration curve which is shown on the left hand side of Figure 6.19. The calibrated top quark mass measured in the dimuon channel is

$$m_{top,RunIIb,\mu\mu}^{calibrated} = 171.5 \pm 15.4 \text{ GeV}.$$

Finally the uncertainty is corrected for the pull width. Because the uncertainty is underestimated this correction leads to a larger statistical uncertainty:

$$m_{top,RunIIb,\mu\mu}^{corrected} = 171.5 \pm 17.5 \text{ GeV}. \tag{6.22}$$

In Figure 6.22 the uncertainty distributions after each of the steps are shown which were created during the ensemble testing. This is only shown for ensembles with a generated top quark mass of 170 GeV because the measured top quark mass is close to this mass point. The uncertainty obtained in the mass measurement is indicated as a blue arrow. The uncertainty of the measurement lies in a region close to the maximum of the distribution. This shows a good agreement with the expected uncertainties coming from the ensemble testing.

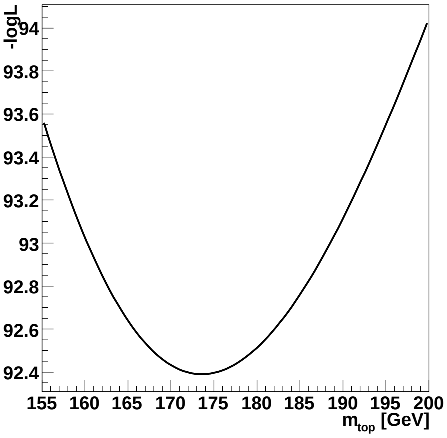

Figure 6.21.: Negative logarithm of the likelihood for the dimuon channel as a function of m_{top}. n_b and n_s are kept constant and are chosen in such away that the negative logarithm of the likelihood is minimized.

6.7.2. $e\mu$ Channel

Signal Fit

As for the dimuon channel (Section 6.7.1) the three-dimensional fit is done for the signal Monte Carlo in the $e\mu$ channel. The 14 parameters obtained by this fit are given in Equation 6.23.

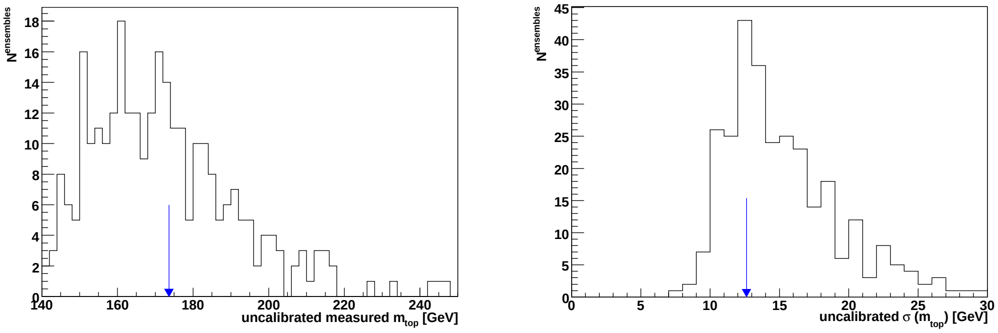

(a) Measured top quark mass (left) and uncertainty (right).

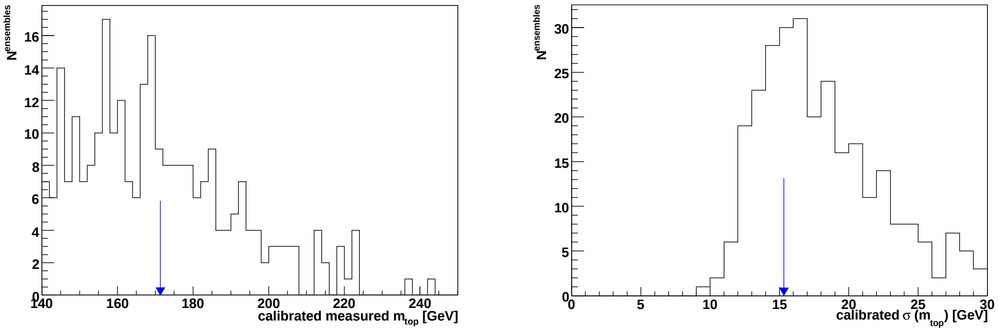

(b) Top quark mass (left) and uncertainty (right) after calibration.

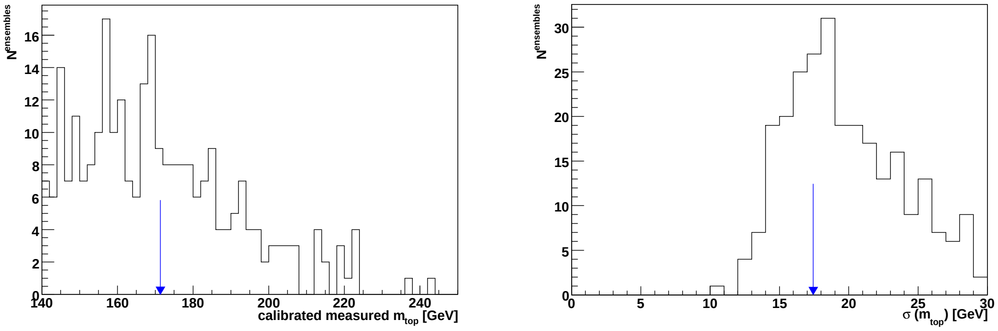

(c) Top quark mass (left) and uncertainty (right) after calibration with pull correction.

Figure 6.22.: Top quark mass and estimated uncertainty of the measured top quark mass in the dimuon channel. The histograms show the top quark mass distribution and uncertainties distribution created during the ensemble testing for mass point 170 GeV. The blue arrows show the top quark mass and its uncertainty obtained from data.

$$\begin{aligned}
p_0 &= 202.7 \pm 0.3 \\
p_1 &= 1.36 \pm 0.02 \\
p_2 &= 0.67 \pm 0.02 \\
p_3 &= 19.2 \pm 0.2 \\
p_4 &= 6.16211 \times 10^{-10} \pm 1.664 \times 10^{-3} \\
p_5 &= 0.16 \pm 0.02 \\
p_7 &= 0.38 \pm 0.02 \\
p_8 &= 8.4 \times 10^{-7} \pm 1.1 \times 10^{-7} \\
p_9 &= 3.84 \pm 0.04 \\
p_{10} &= 0.275 \pm 0.008 \\
p_{11} &= 1.373 \pm 0.004 \\
p_{12} &= 0.0920 \pm 0.0010 \\
p_{13} &= 1.8 \\
p_{14} &= 0.16 \pm 0.21.
\end{aligned} \tag{6.23}$$

This fit is, with $\frac{\chi^2}{ndf} = 3.6$, not as good as the fit for the dimuon channel. Parameter and p_{13} were fixed to the values given in Equation 6.23 to obtain a smooth fit function. Additionally, as in the dimuon channel, the uncertainties of some parameters is larger than their value. So the fit could be improved. Plots of the fitted function can be found in Figures 6.23, 6.24, and 6.25 as well as in Appendix F. As can be seen on some of the plots in Appendix F the fitted function for constant simulated top quark mass and constant *rms* does not show such a good agreement to the distribution it was fitted to. Also the fitted function looks very different from the distribution it was fitted to for constant *mean* and *rms*. Some additional work is to be done here to make the fitted function look more like the distribution it was fitted to. Probably the differences are due to the fact that a smaller mass range is used in the $e\mu$ channel than in the dimuon channel. However, the fit still fulfills the requirements needed for the mass measurement. The function is smooth and a correlation between the mean and m_{top} can be seen.

Background Fit

An analytic function with seven parameters is fitted to the background. The parameters obtained by this fit are given in Equation 6.24:

$$\begin{aligned}
p_0 &= 2887.35 \pm 315.78 \\
p_1 &= 0.046 \pm 0.003 \\
p_2 &= -0.034 \pm 0.018 \\
p_3 &= 6.79 \pm 0.31 \\
p_4 &= 0.0058 \pm 0.0130 \\
p_5 &= 0.063 \pm 0.011 \\
p_6 &= -0.14 \pm 1.95
\end{aligned} \tag{6.24}$$

One gets $\frac{\chi^2}{ndf} = 3.8$. A plot of the function fitted to the background can be found in Figure 6.26. The WZ background was not used because it is small and therefore is expected to have nearly no influence on the result.

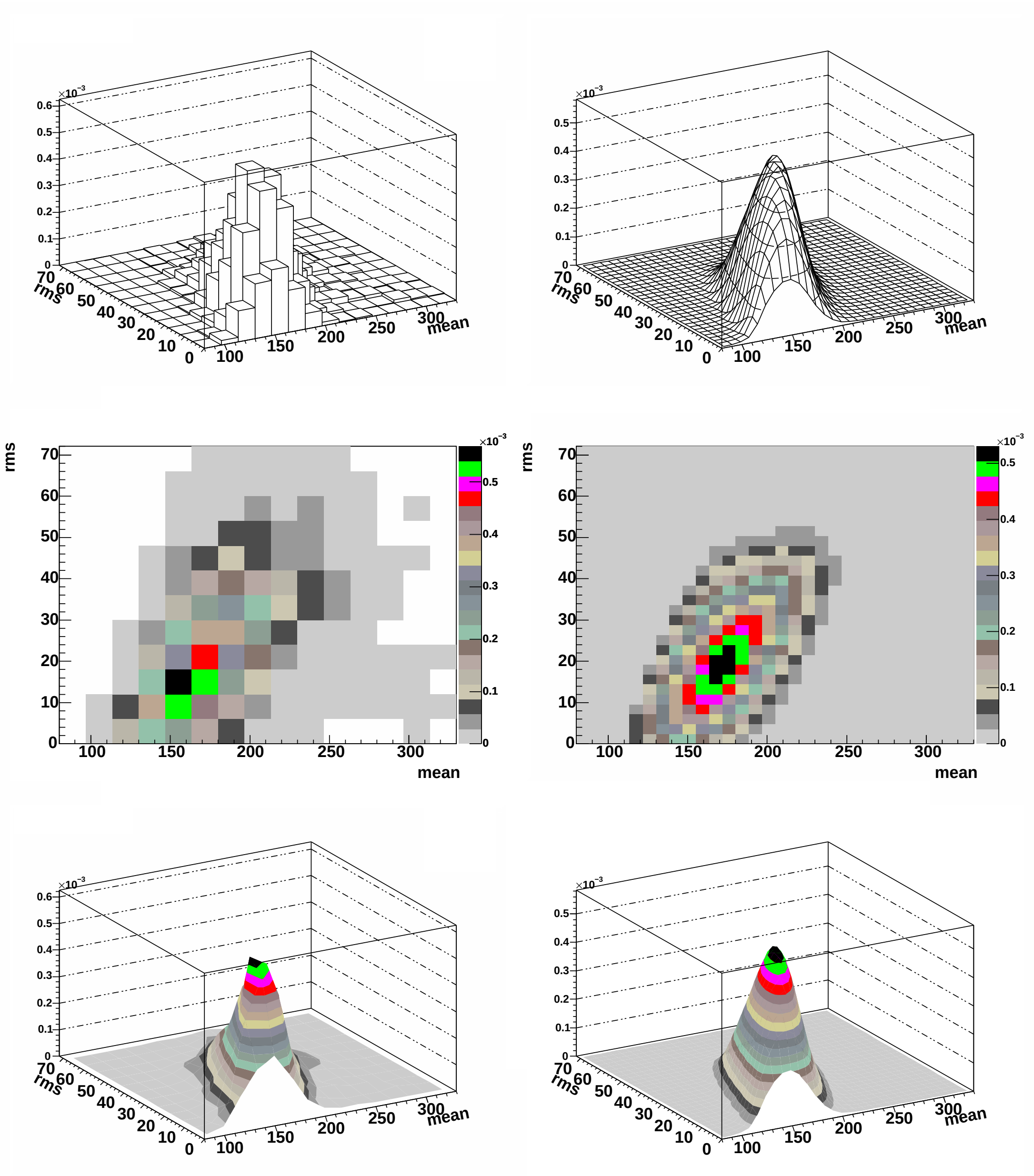

Figure 6.23.: Signal fit function for $m_{top} = 170$ GeV in the $e\mu$ channel. In the plots on the left hand side the distribution coming from the neutrino weighting, in the plots on the right hand side the fitted function is shown.

Ensemble Testing

As for the dimuon channel an ensemble testing is performed as described in Section 6.6.2. The calibration curves are shown in Figure 6.27. On the left hand side of this figure the output top quark mass minus 175 GeV in plotted against the input top quark mass minus 175 GeV. A slope of one and an offset of zero is expected for this curve. From the ensemble testing a slope of 0.8 ± 0.01 is obtained which is smaller than the expected value. The offset is 3.7 ± 0.2 GeV. On the right hand side of the same figure the output top quark mass minus the input top quark mass

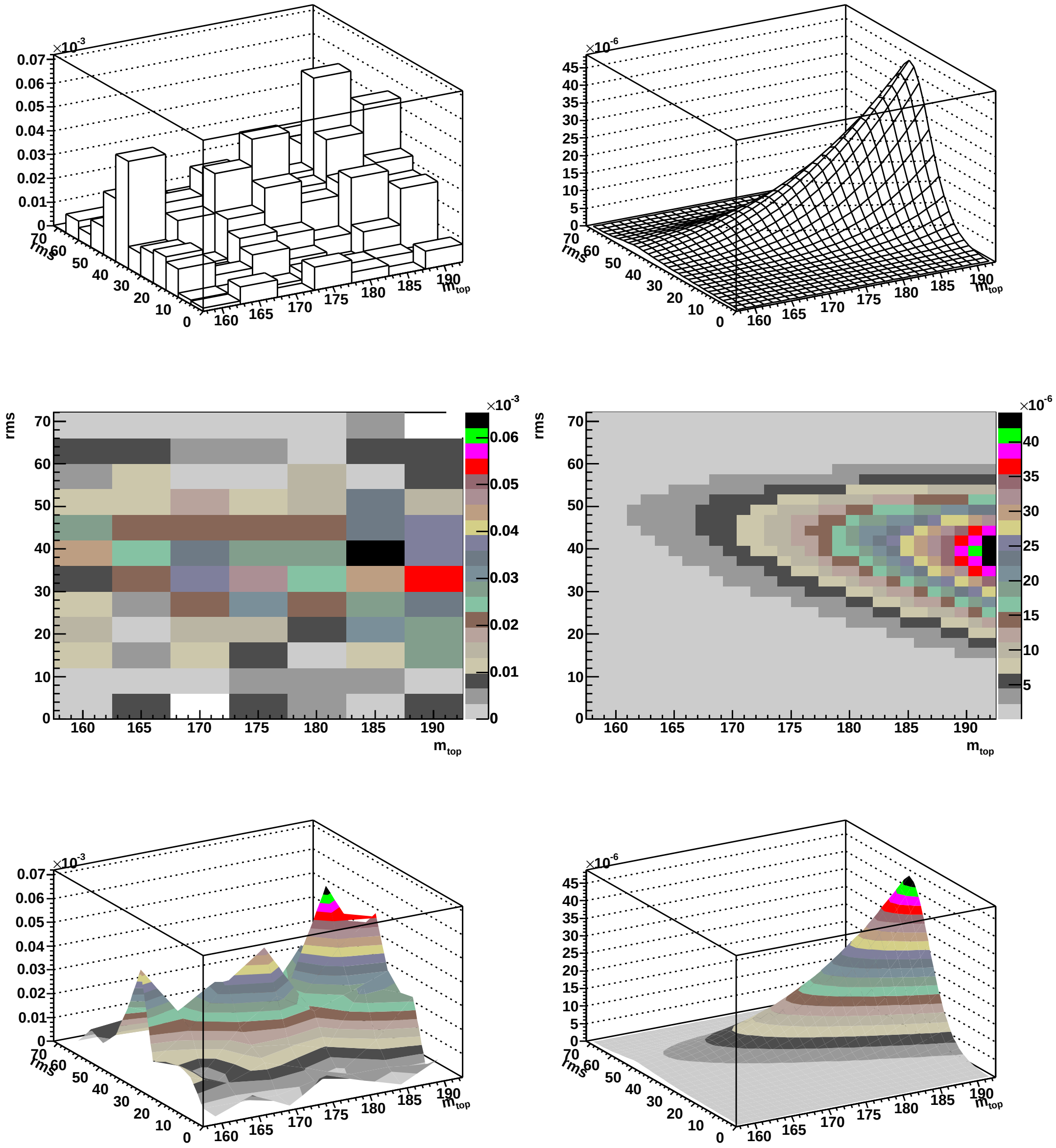

Figure 6.24.: Signal fit function for mean = 175 GeV in the $e\mu$ channel. In the plots on the left hand side the distribution coming from the neutrino weighting, in the plots on the right hand side the fitted function is shown.

is plotted against the input top quark mass minus 175 GeV. In this case the slope is expected to be zero, but in reality it is -0.2 ± 0.02.

Pull mean and pull width in the different mass bins for the $e\mu$ channel are shown in Figure 6.28. The pull mean has a value of -0.01 ± 0.05 which is in good agreement with zero. The pull width has a value of 1.4 ± 0.05, which is much larger than one. This means, that the statistical uncertainty is underestimated by about 40%. This is a large discrepancy and additional work is to be done here.

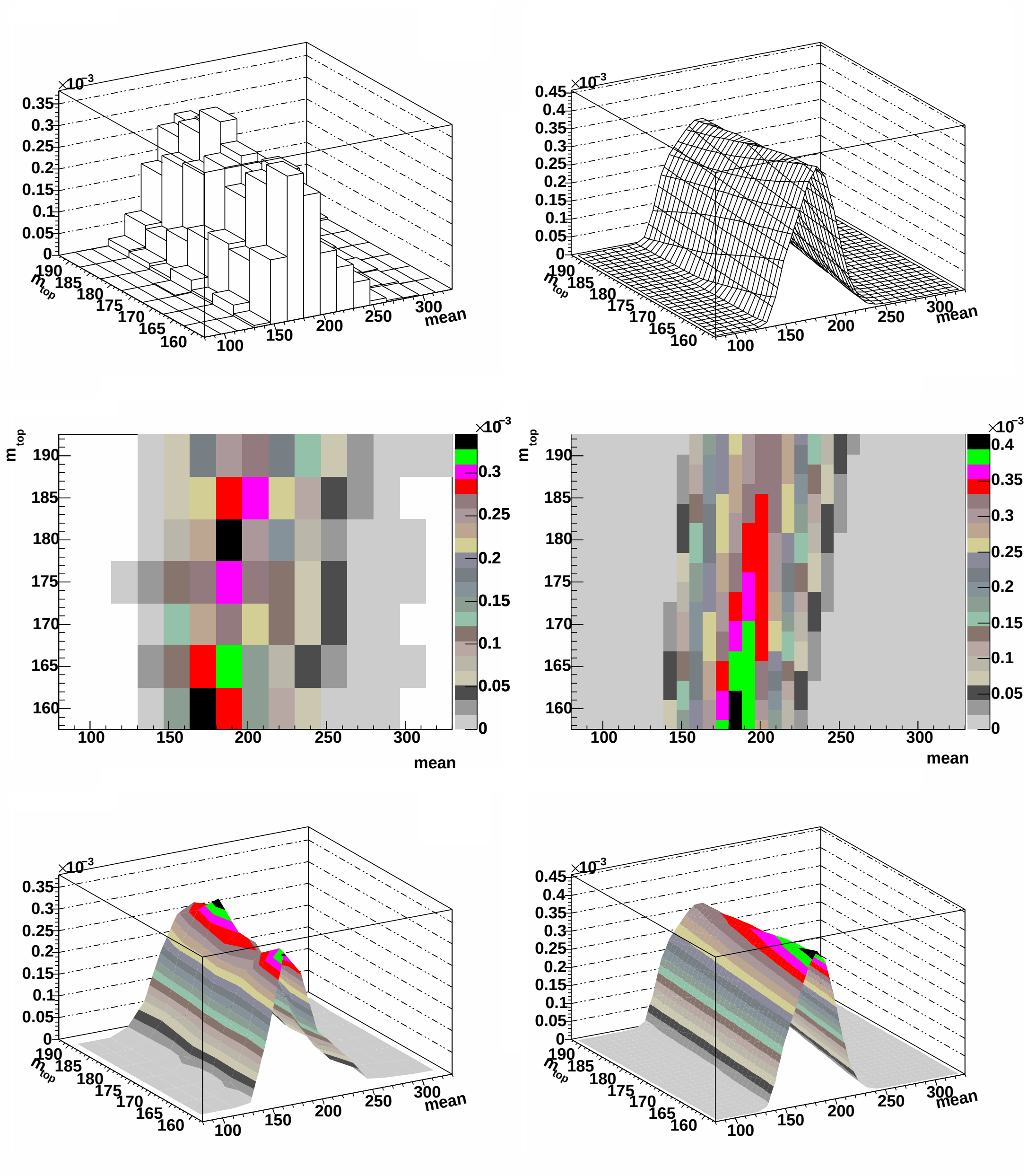

Figure 6.25.: Signal fit function for rms = 33 GeV in the $e\mu$ channel. In the plots on the left hand side the distribution coming from the neutrino weighting, in the plots on the right hand side the fitted function is shown.

Mass Measurement

The uncalibrated top quark mass obtained from data with the maximum likelihood method in the $e\mu$ channel is

$$m_{top,RunIIb,e\mu}^{measured} = 189.7 \pm 4.2 \text{ GeV}.$$

Compared to the dimuon channel the uncertainty is much lower in the $e\mu$ channel. This is due to the fact that much higher statistics is available in the $e\mu$ channel. One reason is the higher

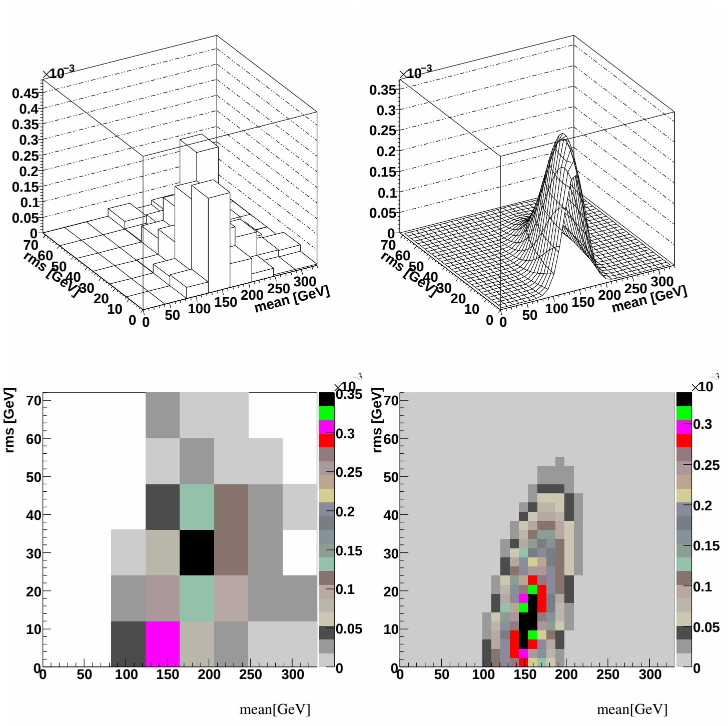

Figure 6.26.: Function fitted to the background for the $e\mu$ channel. The two plots on the left hand side show the distribution coming from the neutrino weighting. The plots on the right hand side show the fitted function.

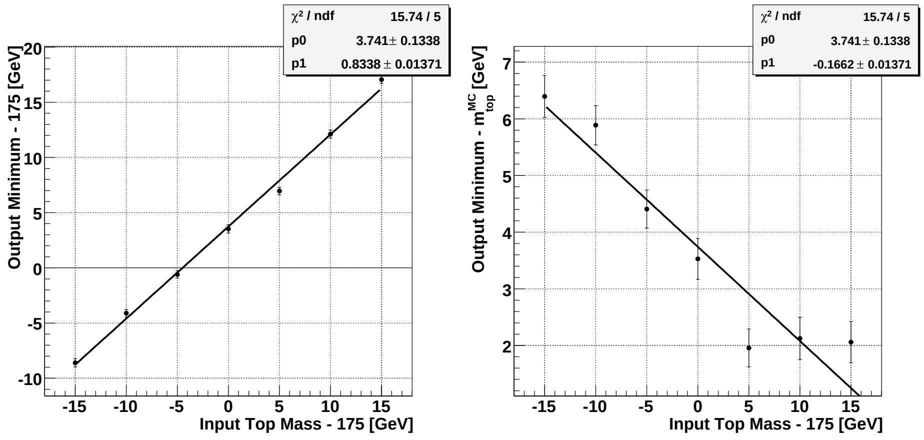

Figure 6.27.: Calibration curves for the $e\mu$ channel.

branching ratio in the $e\mu$ channel. Additionally in the $e\mu$ channel the background is lower because no direct $Z \rightarrow ll$ background exists. Another reason is that, for the $e\mu$ channel the Run IIb postshutdown dataset is available, but not yet for the dimuon channel. So a higher luminosity is available for the $e\mu$ channel. A third reason is the better electron resolution compared to the muon resolution. This leads to more candidates. The negative logarithm of the likelihood is shown in Figure 6.29.

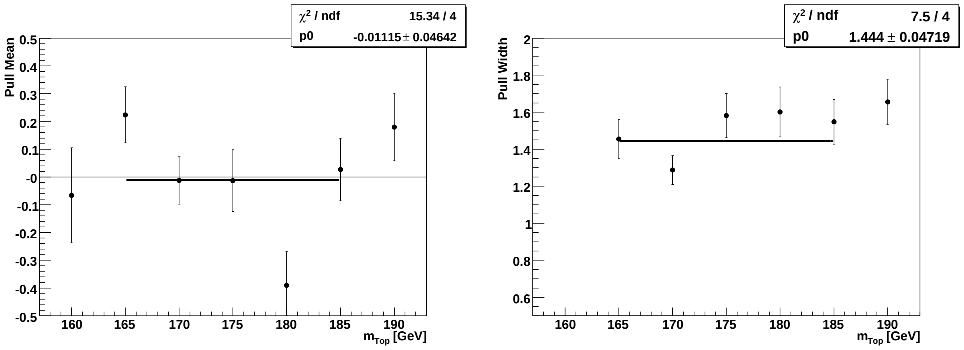

Figure 6.28.: Pull mean on the left hand side and the pull width on the right hand side for the $e\mu$ channel.

After calibration one gets

$$m^{calibrated}_{top,RunIIb,e\mu} = 188.1 \pm 5.1 \text{ GeV}.$$

And with pull correction

$$m^{corrected}_{top,RunIIb,e\mu} = 188.1 \pm 7.3 \text{ GeV}. \tag{6.25}$$

These three values compared to the results coming from the ensemble testing can be found in Figure 6.30.

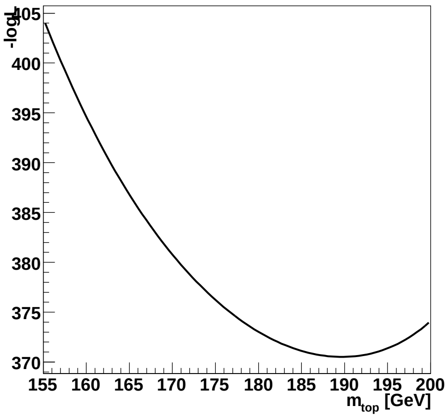

Figure 6.29.: negative logarithm of the likelihood for the $e\mu$ channel as a function of m_{top}. n_b and n_s are kept constant and are chosen in such away that the negative logarithm of the likelihood is minimized.

6.7.3. Combination

The two results can now be combined as described in Section 6.6.1. The result of the combination of the uncalibrated values is

$$m^{measured}_{top,RunIIb,combined} = 188.5 \pm 4.2 \text{ GeV}.$$

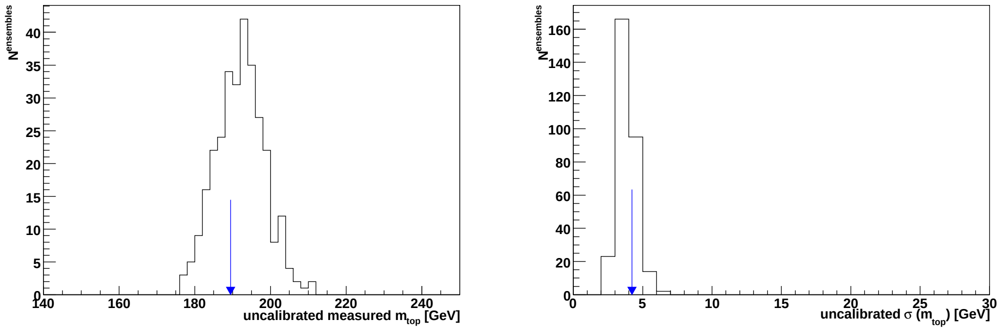

(a) Measured top quark mass (left) and uncertainty (right).

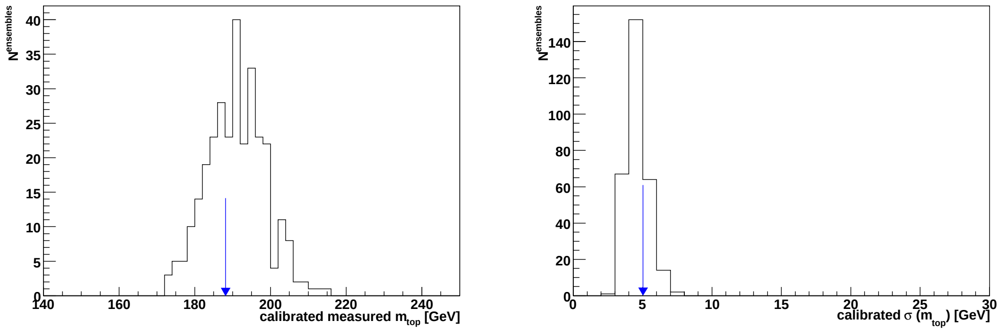

(b) Top quark mass (left) and uncertainty (right) after calibration.

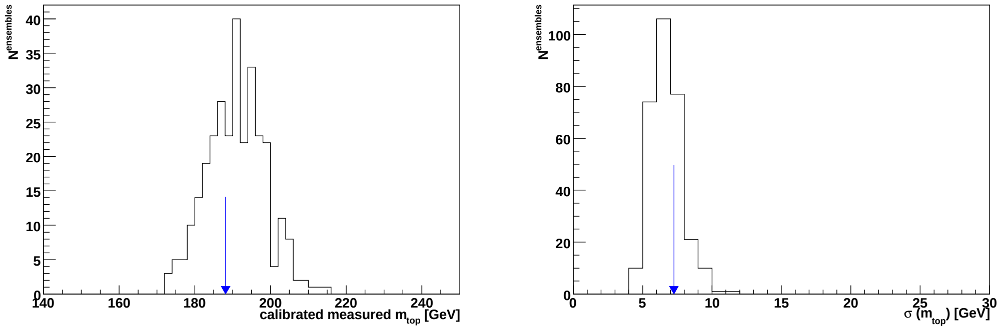

(c) Top quark mass (left) and uncertainty (right) after calibration with pull correction.

Figure 6.30.: Top quark mass and estimated uncertainty of the measured top quark mass in the $e\mu$ channel. The histograms show the top quark mass distribution and uncertainties distribution created during the ensemble testing for mass point 190 GeV. The blue arrows show the top quark mass and its uncertainty obtained from data.

As expected the value of the combination is closer to the result coming from the $e\mu$ channel because this is the more precise measurement. The negative logarithm of the combined likelihood is shown in Figure 6.31. The calibration curve for the combination is shown in Figure 6.32. It

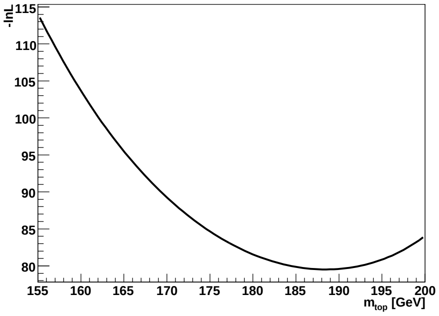

Figure 6.31.: Negative logarithm of the combined likelihood as a function of m_{top}. n_b and n_s are kept constant and are chosen in such a way that the negative logarithm of the likelihood is minimized.

shows a slope of 0.8±0.02 and an offset of 3.1±0.2 GeV. The ensemble testing for the combination was performed for the mass bins 160 GeV, 165 GeV, 170 GeV, 175 GeV, 180 GeV, 185 GeV, and 190 GeV, because these mass bins are the ones which are available in both channels, $e\mu$ and $\mu\mu$.

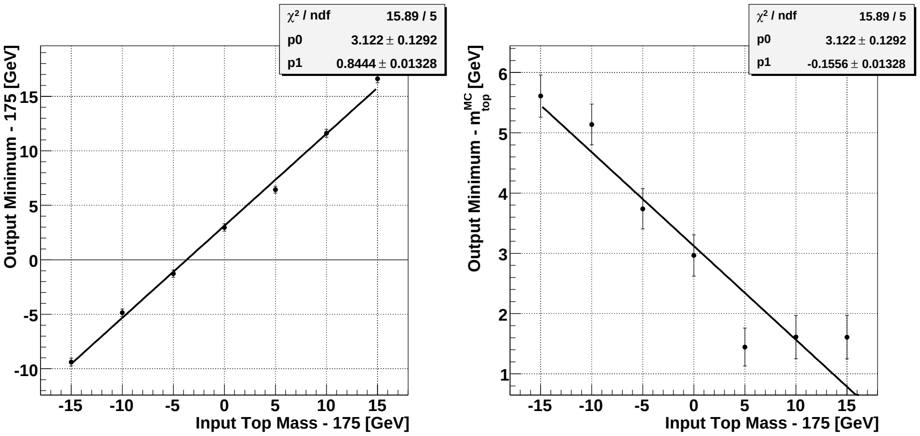

Figure 6.32.: Calibration curves for the combination of the dimuon channel and the $e\mu$ channel.

With calibration the combined value for the top quark mass is

$$m_{top,RunIIb,combined}^{calibrated} = 187.3 \pm 4.9 \text{ GeV}.$$

The distributions of the pull mean and the pull width for the combination are shown in Figure 6.33. Both, pull mean (0.7 ± 0.06) and pull width (1.5 ± 0.06) are significantly different from the expected values. After the pull correction the combined top quark mass is

$$m_{top,RunIIb,combined}^{corrected} = 187.3 \pm 7.3 \text{ GeV}. \tag{6.26}$$

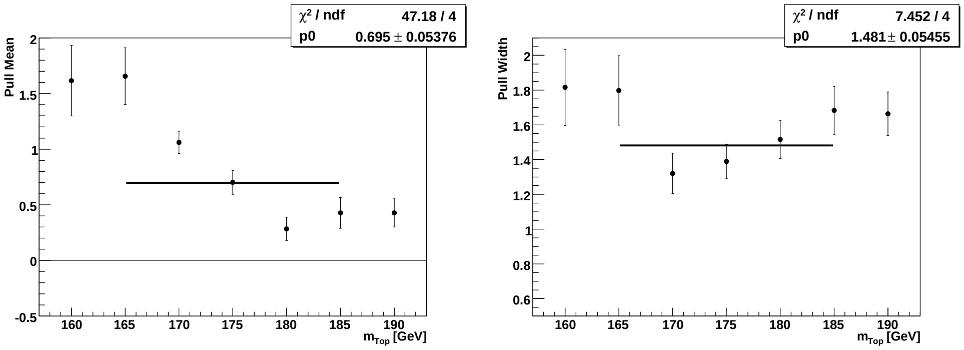

Figure 6.33.: Pull mean on the left hand side and the pull width on the right hand side for the combination of the dimuon channel and the $e\mu$ channel.

These three values for the combination compared to the results from the ensemble testing are shown in figure 6.34.

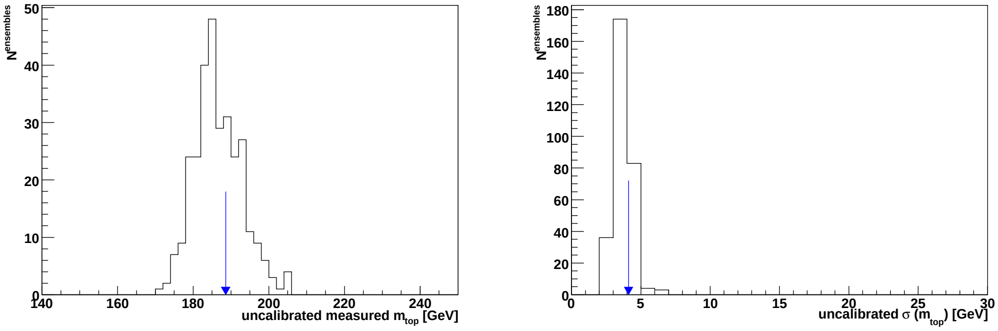

(a) Measured top quark mass (left) and uncertainty (right).

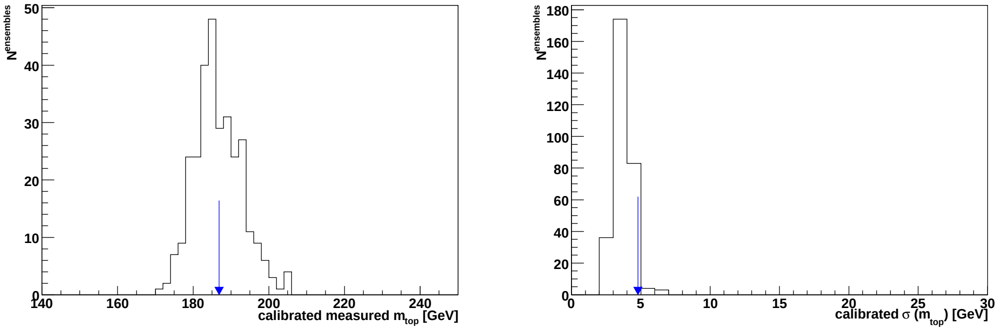

(b) Top quark mass (left) and uncertainty (right) after calibration.

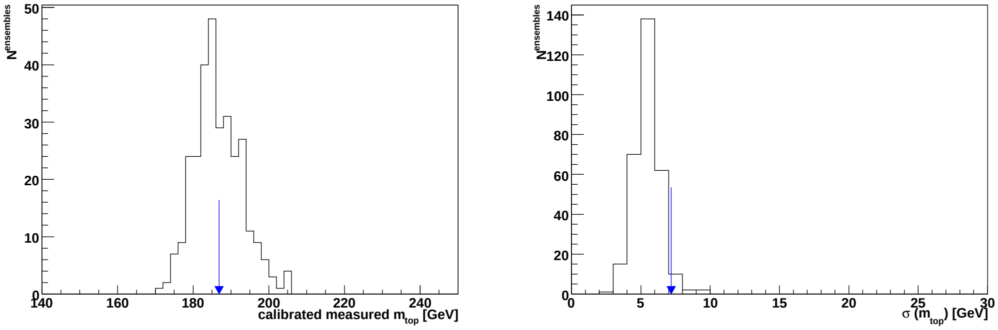

(c) Top quark mass (left) and uncertainty (right) after calibration with pull correction.

Figure 6.34.: Top quark mass and estimated uncertainty of the measured top quark mass in the combination of the $e\mu$ channel and the dimuon channel. The histograms show the top quark mass distribution and uncertainties distribution created during the ensemble testing for mass point 185 GeV. The blue arrows show the top quark mass and its uncertainty obtained from data.

7. Conclusion and Outlook

7.1. Final Result

In this thesis a mass measurement of the top quark in the electron-muon channel and in the dimuon channel via the neutrino weighting method was presented. For the analysis data taken with the DØ detector at Fermilab in Run IIb were used. The dataset for the dimuon channel has a size of 1216 pb^{-1}, the one for the $e\mu$ channel 1780 pb^{-1}. After the selections 13 events are left in the dimuon channel and 68 in the $e\mu$ channel. The combination of the values measured in the $e\mu$ and the $\mu\mu$ channel of the Run IIb dataset is

$$m_{top,RunIIb,combined}^{corrected} = 187.3 \pm 7.3 \text{ (stat.) GeV.}$$

This value was calibrated and pull-corrected. The result for the Run IIa dataset can be found in [60]. The combination of the dimuon channel, the dielectron channel, the $e\mu$ channel, and lepton+track (Events in which one lepton was not reconstructed, so only the track is used.) for this measurement delivers

$$m_{top,RunIIa} = 176.0 \pm 5.3 \text{ (stat.)} \pm 2.0 \text{ (syst.) GeV.}$$

For this measurement about 1 fb^{-1} of data were used.
These two measurements are in agreement with the world average of August 2008 [12]

$$m_{top} = 172.4 \pm 0.7 \text{ (stat.)} \pm 1.0 \text{ (syst.) GeV.}$$

7.2. Outlook: Plans and Improvements

The results for the dimuon selection for the Run IIb preshutdown dataset and for the mass measurement in the dimuon channel as well as in the $e\mu$ channel look reasonable. However, a lot of additional work can and should be done to improve the result.

7.2.1. Dimuon Selection

Already a lot of programming mistakes were fixed in the Run IIb software version which was used for the selection presented in this thesis. However, more programming mistakes were found and fixed. The software version should be updated again. A new Z boson reweighting is available, too. This should be used as well.
A high discrepancy between data and Monte Carlo was observed for small $\not\!\!E_T$. This discrepancy is not understood yet, but it might vanish when using the newest software version containing all programming mistakes fixed.
The fake muons could be added as a background in the comparison plots. For this the loose sample and the tight sample as used for the calculation of the fake muons (Section 6.3.4) are

needed. One should plot the events in the loose sample without the events in the tight sample and scale them according to how many fake muons are expected.

As for the $e\mu$ selection already done, the dimuon selection should be repeated for the Run IIb postshutdown dataset.

Further improvements for the production cross section measurement could be done. The calculation presented in Section 6.5 was only a short test to see if the result is reasonable.

7.2.2. Mass Measurement

For the signal and background fit further improvements could be tried to achieve by using more statistics and by improving the fit function. Some of the parameters have a larger uncertainty than the value itself. The fit for the $e\mu$ channel does look good in general, however, discrepancies are larger than for the dimuon channel. The reason for this might be, that for the $e\mu$ channel not all mass bins were used. So to improve the $e\mu$ fit one should try to use all mass bins between 155 GeV and 200 GeV.

For the dimuon channel only the Run IIb preshutdown dataset was used because the selection for the Run IIb postshutdown dataset is not available yet. The additional data are still to be added. The mass measurement for the dielectron channel and the Run IIb dataset has not been performed yet. As soon as this is done all three dilepton channels can be combined. Also the Run IIa and the Run IIb results can be combined.

For the combination of the dimuon channel and the $e\mu$ channel the pull distributions do not show the expected values for the mean and the width. A better result might already be achieved by improving the measurements of the two channels individually.

Last but not least further studies on systematic uncertainties are necessary.

A. List of Triggers in Run IIa and Run IIb

Run IIa	Run IIb
MU_W_L2M0_TRK3	MUHI1_ITLM10
MU_W_L2M3_TRK10	MUHI1_TK12_TLM12
MU_W_L2M0_TRK10	MUHI1_ILM15
MU_W_L2M5_TRK10	MUHI2_ITLM10
MUW_W_L2M3_TRK10	MUHI2_TK12_TLM12
MUW_W_L2M5_TRK10	MUHI2_ILM15
MUH1_TK10	MUHI3_ITLM10
MUH1_TK12_TLM12	MUHI3_TK12_TLM12
MUH1_TK12	MUHI3_ILM15
MUH1_TK15	
MUH2_LM3_TK12	
MUH2_LM6_TK12	
MUH2_LM10_TK12	
MUH2_LM15	
MUH3_LM3_TK10	
MUH3_LM6_TK12	
MUH3_LM10_TK12	
MUH3_LM15	
MUH4_LM15	
MUH4_TK10	
MUH5_LM15	
MUH6_TK12_TLM12	
MUH6_LM15	
MUH6_TK10	
MUH7_TK12	
MUH7_LM15	
MUH7_TK10	
MUH8_TK12_TLM12	
MUH1_ILM15	
MUH1_ITLM10	
MUH8_ILM10	
MUH_A_L2M3_TRK10	

Table A.1.: List of triggers used in the Run IIa dimuon selection and in the Run IIb dimuon selection.

B. Comparison Plots for the Run IIa Dimuon Selection

Comparison between data and Monte Carlo for the p17 dimuon selection are shown in this appendix. In Figure B.1 the legend for all plots in Appendix B is shown. In all figures the upper left plots are the plots without requirement on the number of jets. The upper right plots show the two jet inclusive plots, the lower left ones the two jet inclusive plots with $\not\!\!E_T$ cut. The lower right plots finally show the two jet inclusive plots with $\not\!\!E_T$ cut and $\not\!\!E_T$ significance cut.
The plots shown here were not produced with the final version of the selection [45]. They were produced with the same version which was used for the comparison between the old Run IIa code and the new Run IIb code (see Section 6.2). All plots in this appendix contain an integrated luminosity of 1069 pb^{-1}.

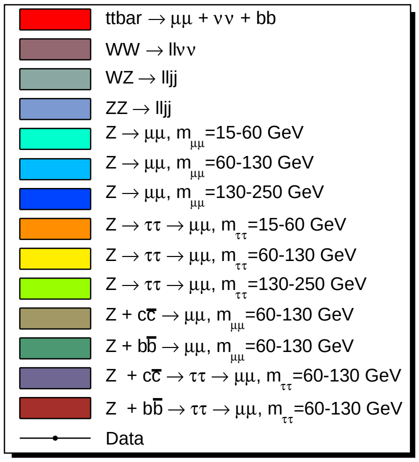

Figure B.1.: Legend for all plots in Appendix B.

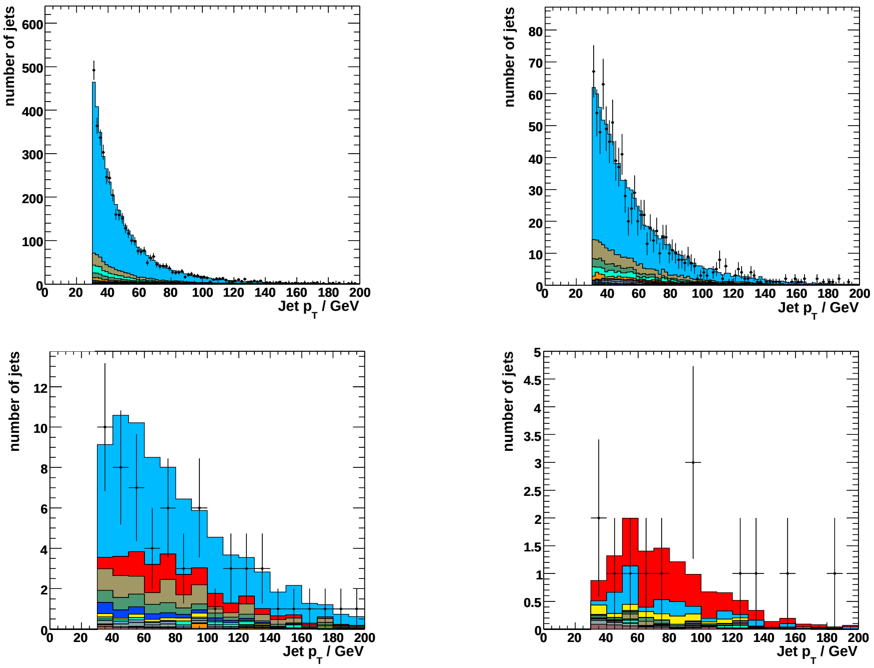

Figure B.2.: p_T of the jet with highest p_T.

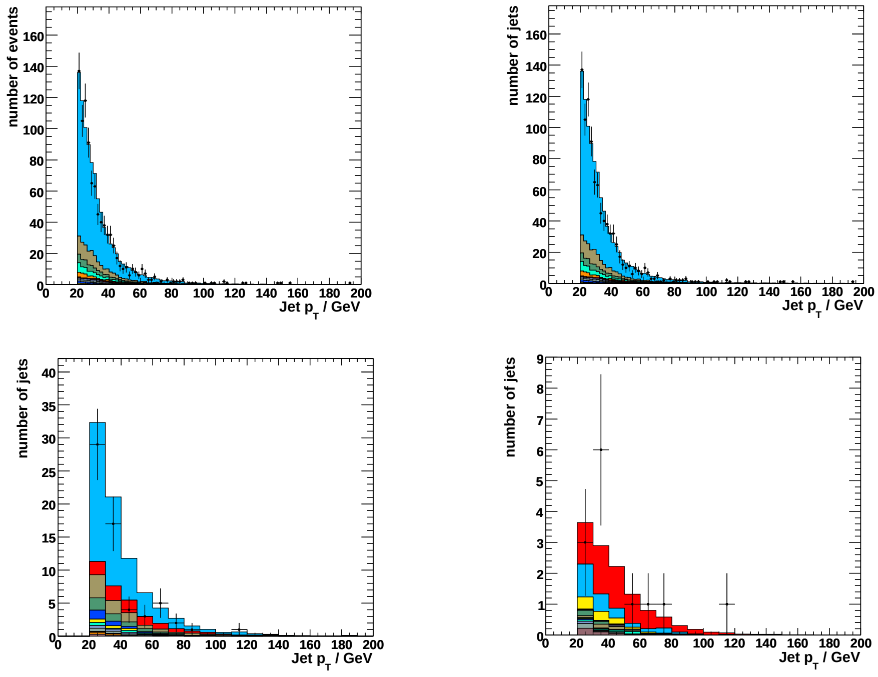

Figure B.3.: p_T of the jet with second highest p_T.

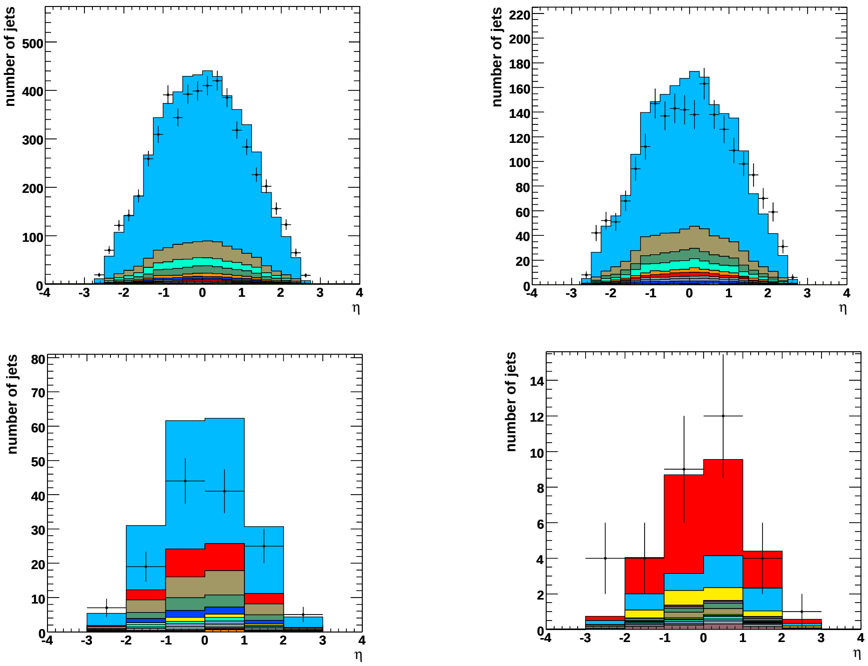

Figure B.4.: η of the jet with highest p_T.

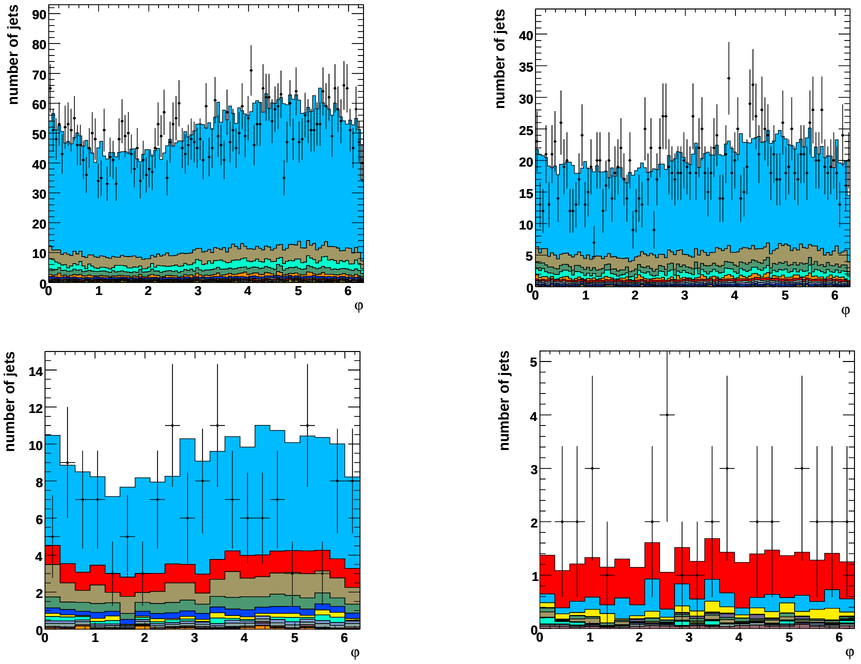

Figure B.5.: φ of the jet with highest p_T.

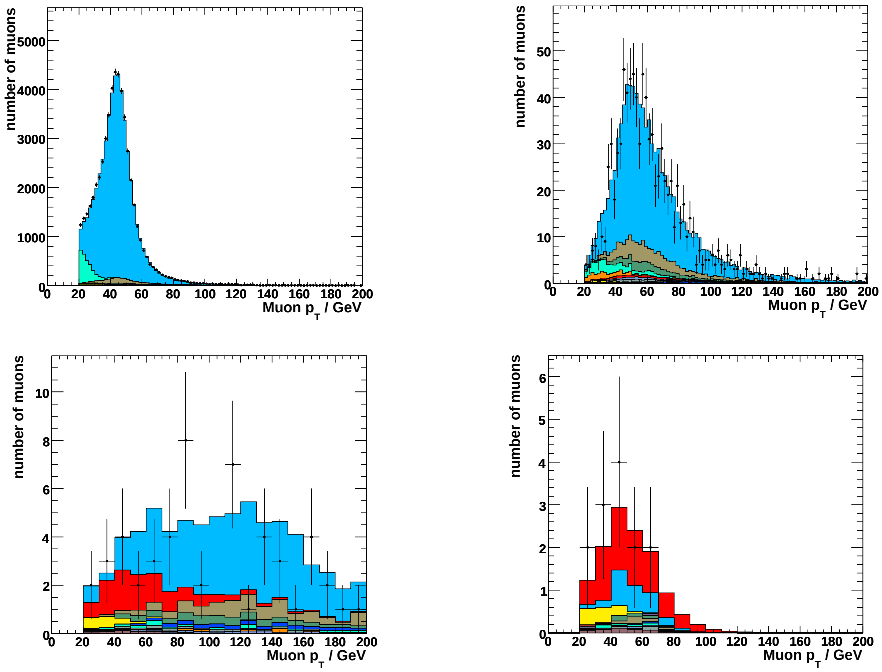

Figure B.6.: p_T of the muon with highest p_T.

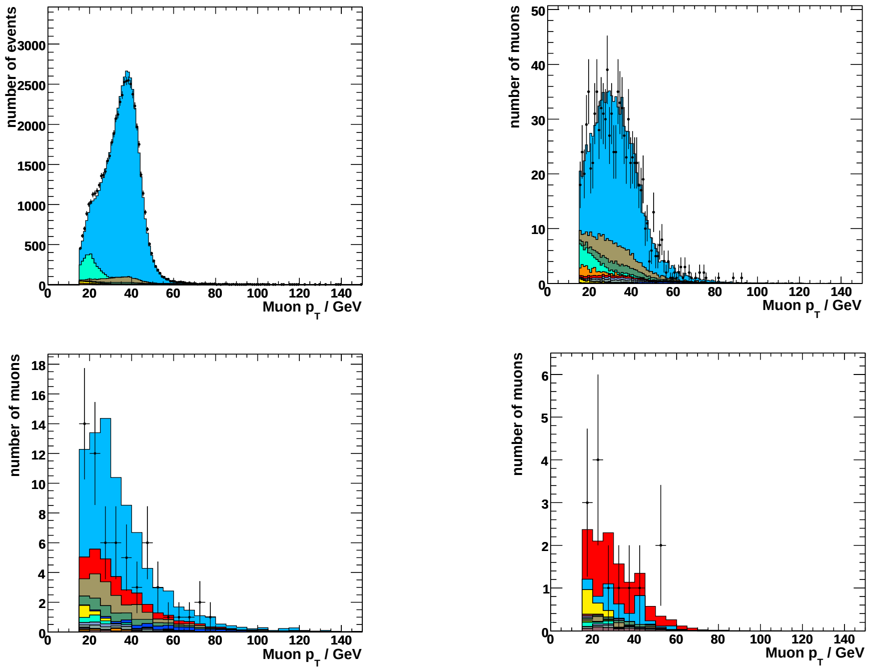

Figure B.7.: p_T of the muon with second highest p_T.

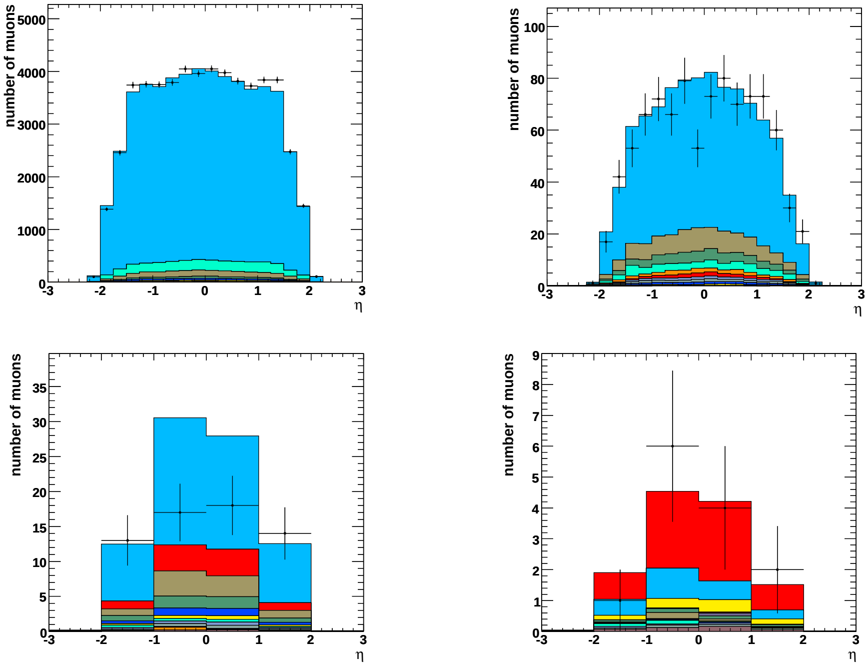

Figure B.8.: η of the muon with highest p_T.

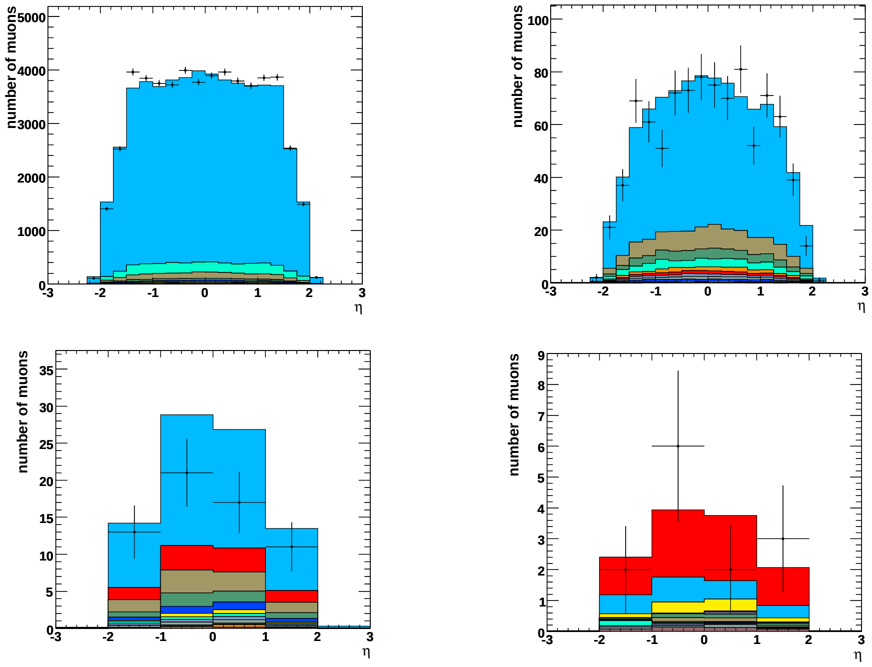

Figure B.9.: η of the muon with second highest p_T.

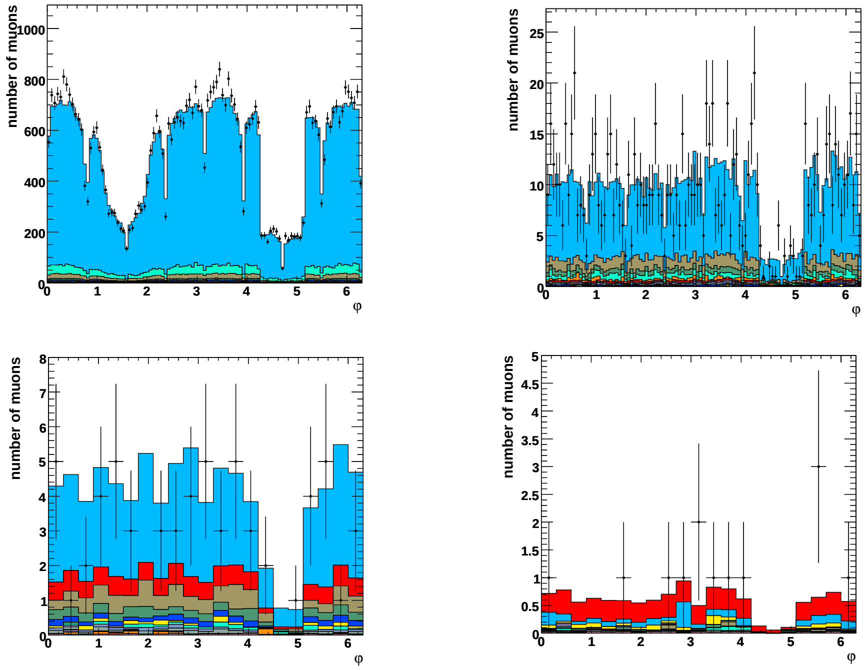

Figure B.10.: φ of the muon with highest p_T.

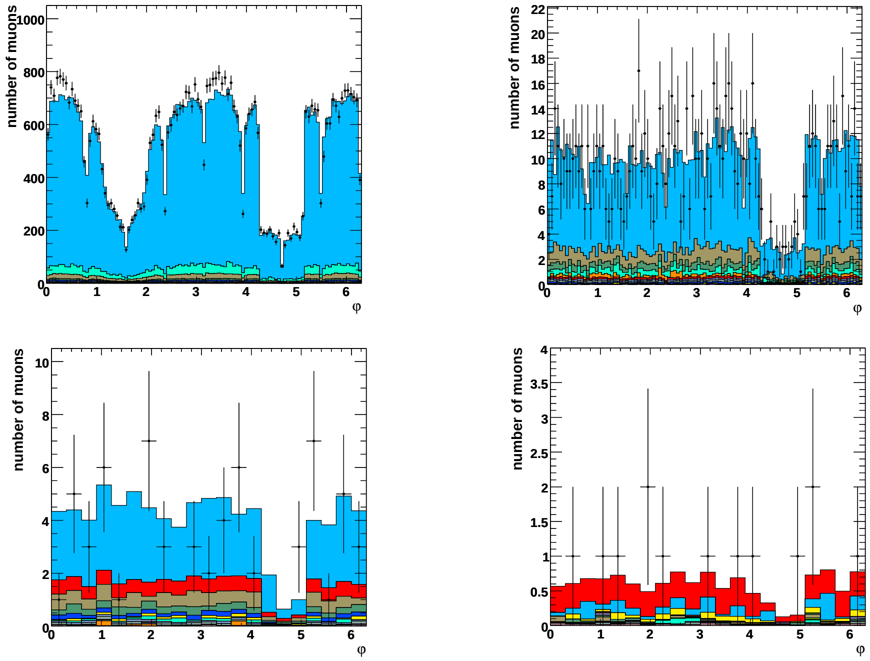

Figure B.11.: φ of the muon with second highest p_T.

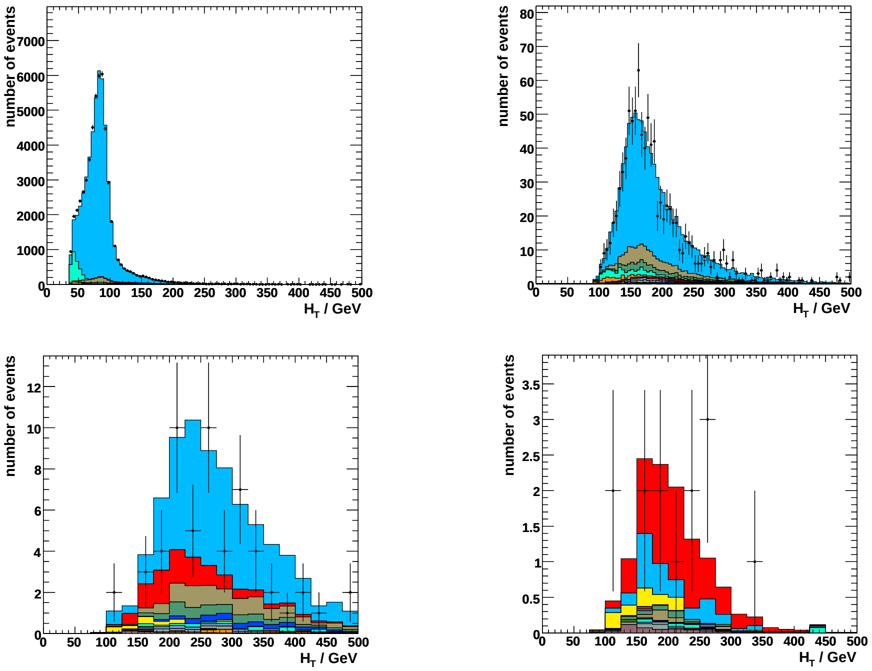

Figure B.12.: H_T.

C. Yield Tables for the Run IIb Dimuon Selection

In this appendix detailed yield tables for the Run IIb dimuon selection are shown. They also contain relative and overal efficiencies for the last three cuts. Every background is listed individually. The tables were produced with a dataset of 1216 pb^{-1}.

	Data	Efficiencies (overall/relative)	total MC	Efficiencies (overall/relative)	Signal	Efficiencies (overall/relative)
incl	47738 ± 218	1.000 ± 0.007/ 1.000 ± 0.006	47205.3 ± 217.3	1.000 ± 0.007/ 1.000 ± 0.007	14.6 ± 3.9	1.000 ± 0.381/ 1.000 ± 0.381
1jet excl	2572 ± 51	0.054 ± 0.002/ 0.054 ± 0.002	2663.0 ± 51.6	0.056 ± 0.002/ 0.056 ± 0.002	3.0 ± 1.8	0.207 ± 0.137/ 0.207 ± 0.137
2jet incl	726 ± 27	0.015 ± 0.001/ 0.282 ± 0.012	572.5 ± 24.0	0.012 ± 0.001/ 0.216 ± 0.010	10.8 ± 3.3	0.745 ± 0.303/ 3.600 ± 2.421
topo	13 ± 4	0.001 ± 0.001/ 0.018 ± 0.005	12.67 ± 3.6	0.001 ± 0.001/ 0.022 ± 0.007	7.2 ± 2.7	0.497 ± 0.230/ 0.667 ± 0.322

	$Z \to \mu\mu$	Efficiencies (overall/relative)	$Z \to \tau\tau \to \mu\mu$	Efficiencies (overall/relative)	Diboson	Efficiencies (overall/relative)
incl	46760.3 ± 371.2	1.000 ± 0.012/ 1.000 ± 0.011	347.7 ± 18.6	1.000 ± 0.076/ 1.000 ± 0.076	82.8 ± 9.1	1.000 ± 0.155/ 1.000 ± 0.155
1jet excl	2626.9 ± 55.6	0.056 ± 0.002/ 0.056 ± 0.002	19.1 ± 4.4	0.055 ± 0.013/ 0.055 ± 0.013	13.9 ± 3.7	0.168 ± 0.049/ 0.168 ± 0.049
2jet incl	544.1 ± 23.8	0.012 ± 0.001/ 0.207 ± 0.010	4.1 ± 2.0	0.012 ± 0.006/ 0.215 ± 0.116	16.5 ± 4.1	0.199 ± 0.054/ 1.187 ± 0.432
topo incl	3.7 ± 1.9	0.001 ± 0.001/ 0.007 ± 0.004	1.0 ± 1.0	0.003 ± 0.003/ 0.244 ± 0.272	0.8 ± 0.9	0.009 ± 0.011/ 0.048 ± 0.056

	WW	Efficiencies (overall/relative)	WZ	Efficiencies (overall/relative)	ZZ	Efficiencies (overall/relative)
incl	41.6 ± 6.5	1.000 ± 0.220/ 1.000 ± 0.219	32.9 ± 5.7	1.000 ± 0.247/ 1.000 ± 0.247	8.4 ± 2.9	1.000 ± 0.489/ 1.000 ± 0.489
1jet excl	3.1 ± 1.8	0.074 ± 0.044/ 0.074 ± 0.044	8.7 ± 3.0	0.265 ± 0.101/ 0.265 ± 0.101	2.1 ± 1.5	0.257 ± 0.196/ 0.257 ± 0.196
2jet incl	0.7 ± 0.9	0.018 ± 0.021/ 0.243 ± 0.317	11.7 ± 3.4	0.357 ± 0.122/ 1.345 ± 0.607	4.0 ± 2.0	0.482 ± 0.293/ 1.905 ± 1.661
topo	0.4 ± 0.7	0.011 ± 0.016/ 0.568 ± 1.114	0.3 ± 0.5	0.009 ± 0.0163/ 0.026 ± 0.044	0.0 ± 0.2	0.006 ± 0.027/ 0.012 ± 0.051

D. Comparison Plots for the Run IIb Dimuon Selection

Comparison between data and Monte Carlo for the Run IIb dimuon selection are shown in this appendix. In Figure D.1 the legend for all plots in Appendix D is shown. In all figures the upper left plots are the plots without requirement on the number of jets. The upper right plots show the two jet inclusive plots, the lower left ones the two jet inclusive plots with $\not\!\!E_T$ cut. The lower right plots finally show the two jet inclusive plots with $\not\!\!E_T$ cut and $\not\!\!E_T$ significance cut. The plots were produced for an integrated luminosity of 1216 pb^{-1}.

Figure D.1.: Legend for all plots in Appendix D.

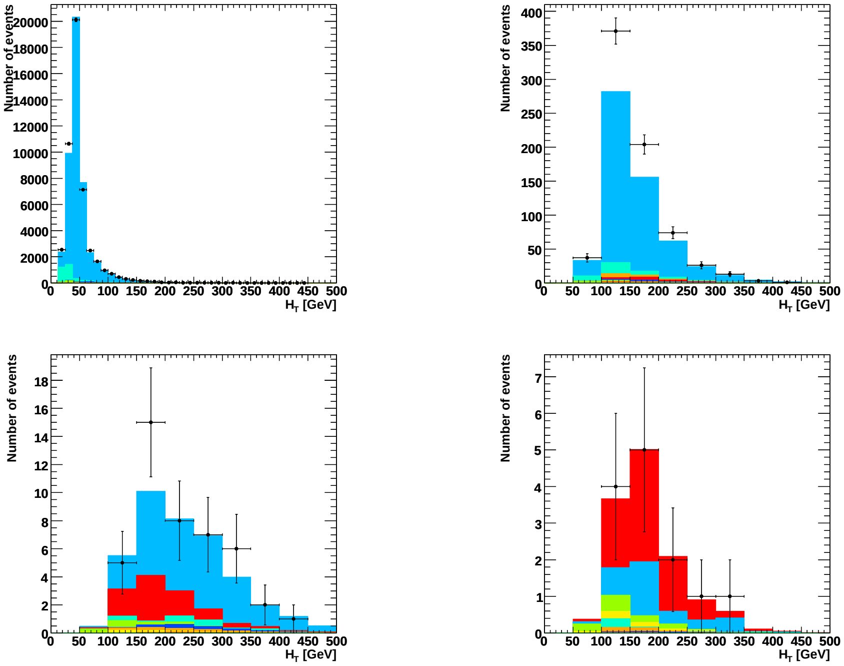

Figure D.2.: H_T.

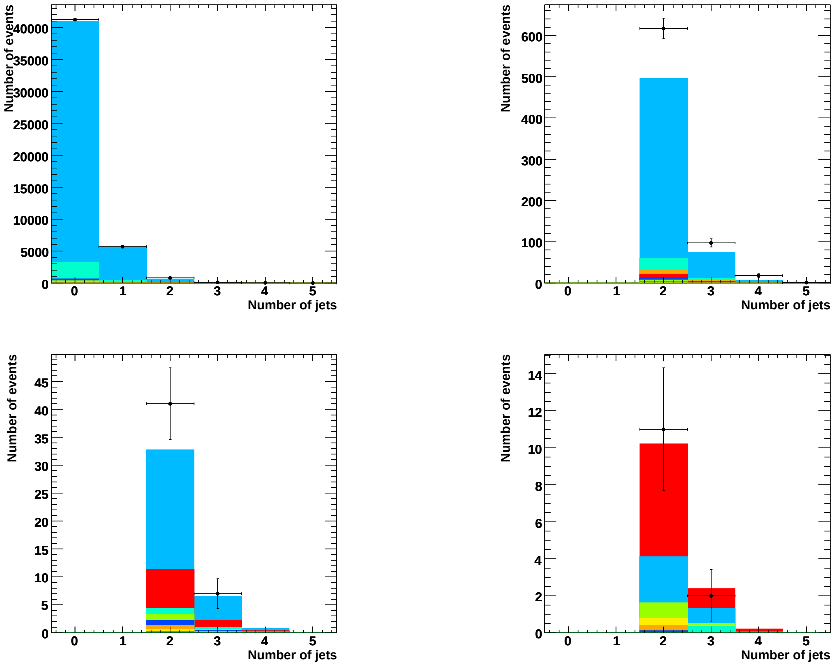

Figure D.3.: Number of jets.

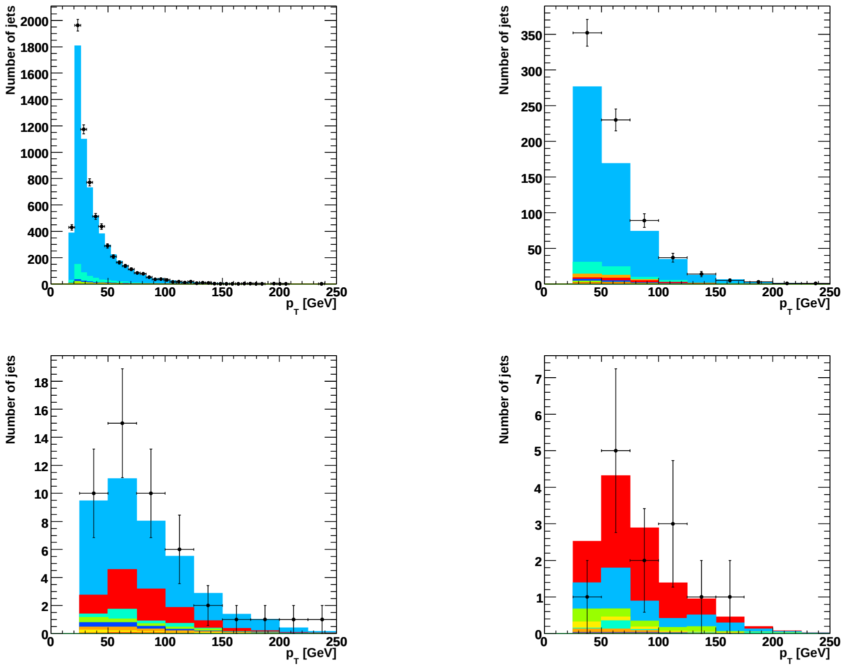

Figure D.4.: p_T of the jet with the highest p_T.

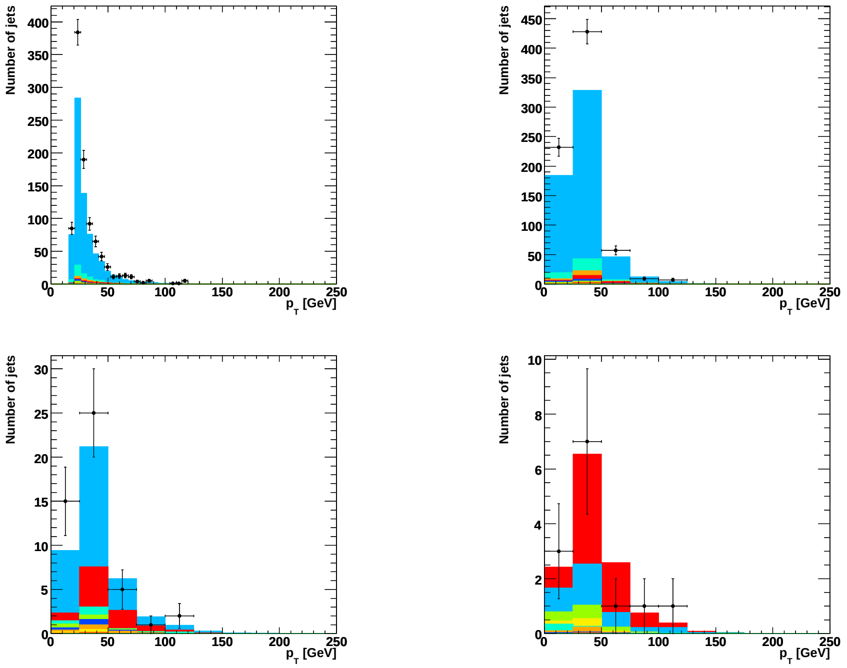

Figure D.5.: p_T of the jet with the second highest p_T.

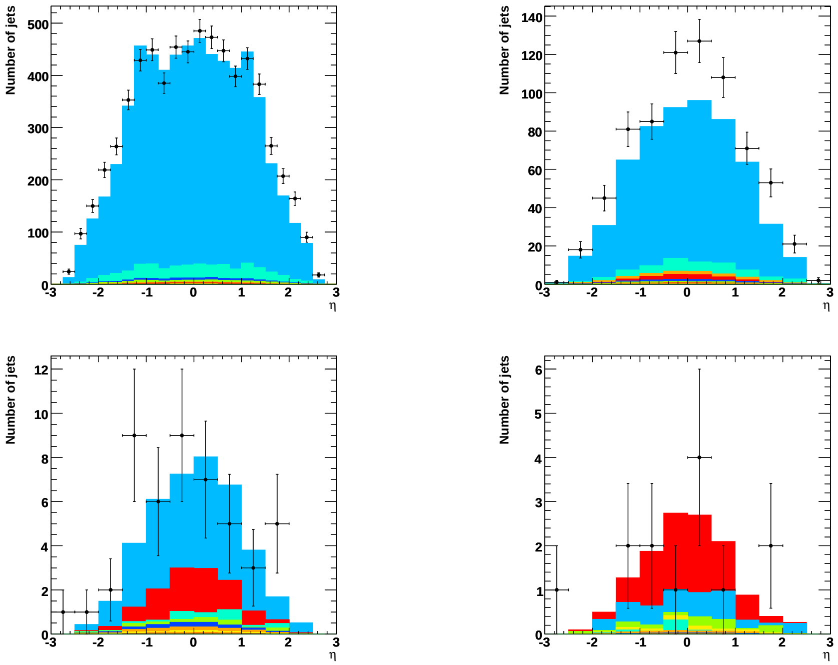

Figure D.6.: η of the jet with the highest p_T.

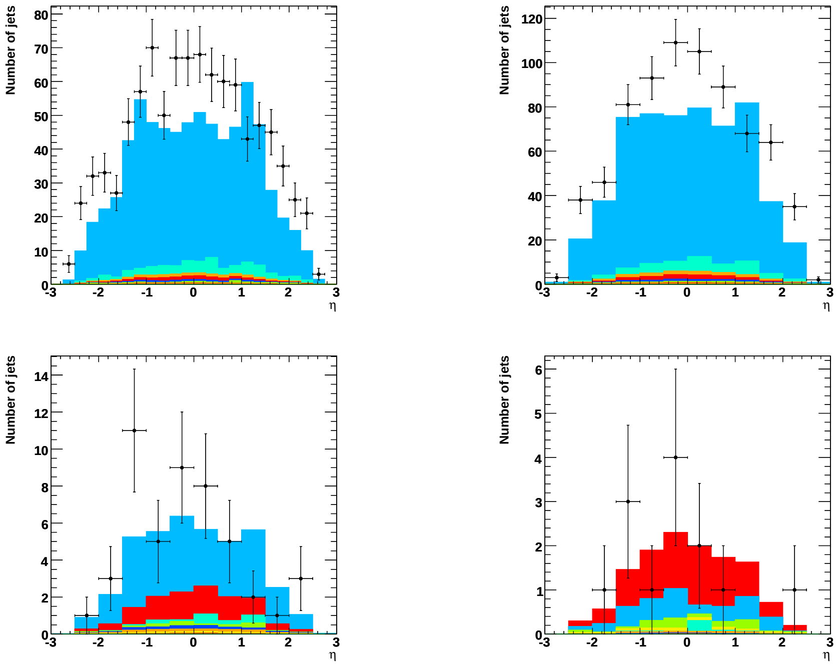

Figure D.7.: η of the jet with the second highest p_T.

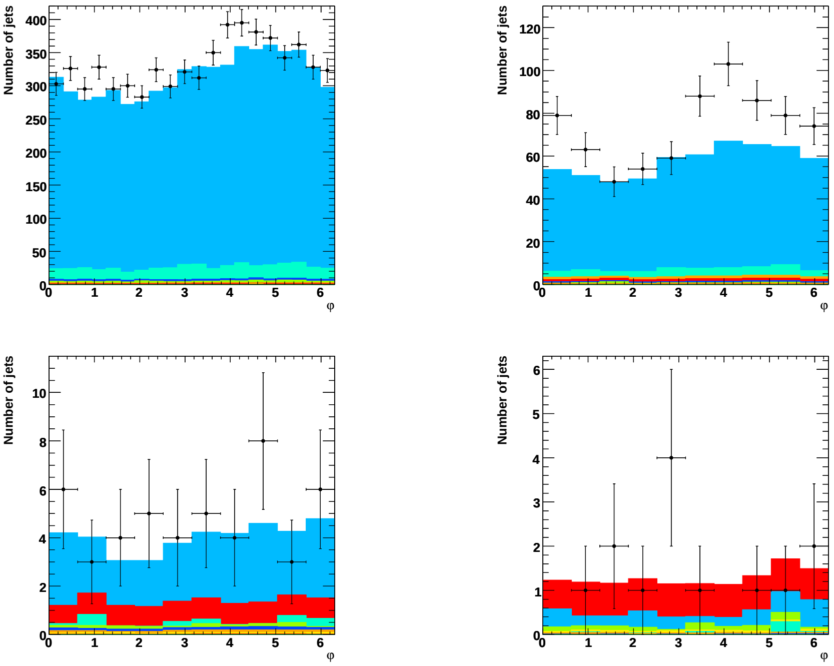

Figure D.8.: φ of the jet with the highest p_T.

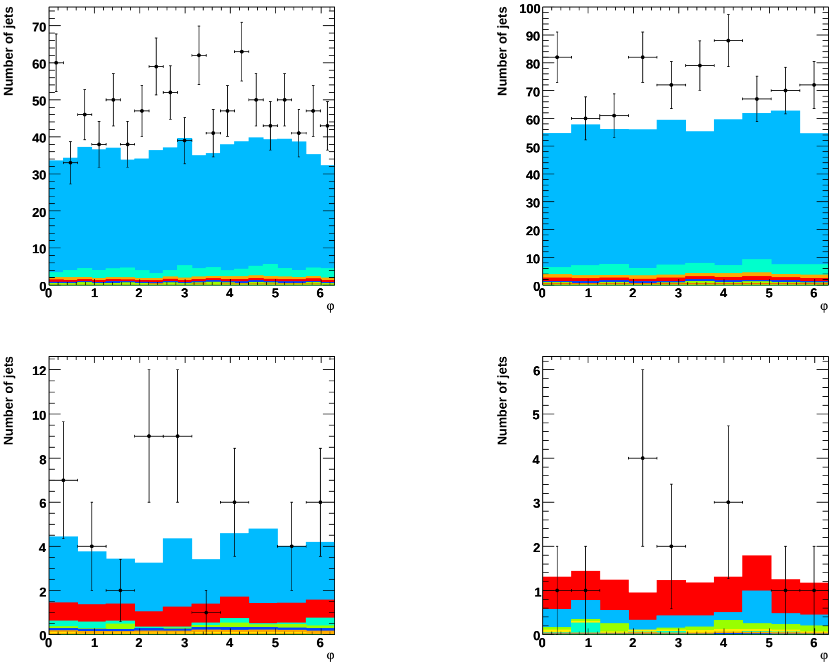

Figure D.9.: φ of the jet with the second highest p_T.

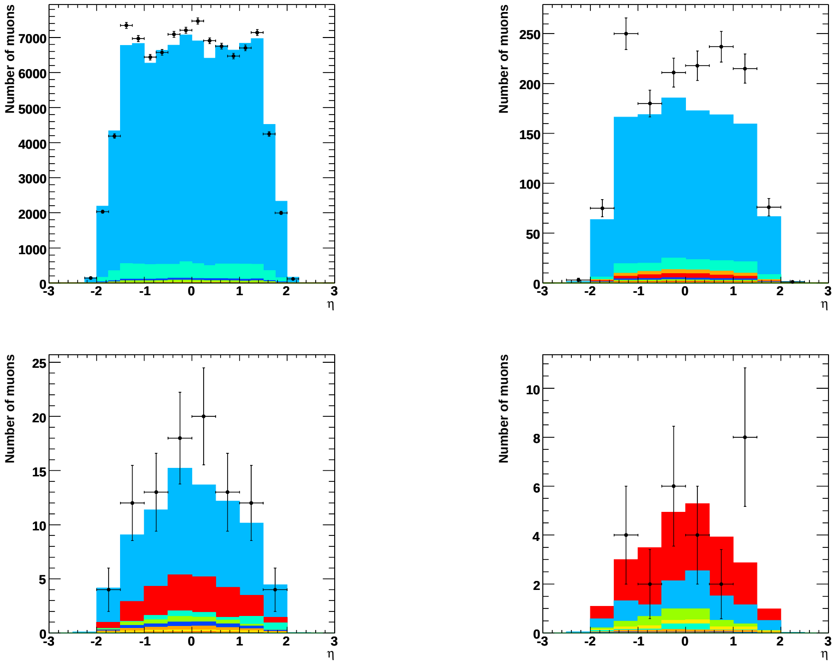

Figure D.10.: η of the two muons.

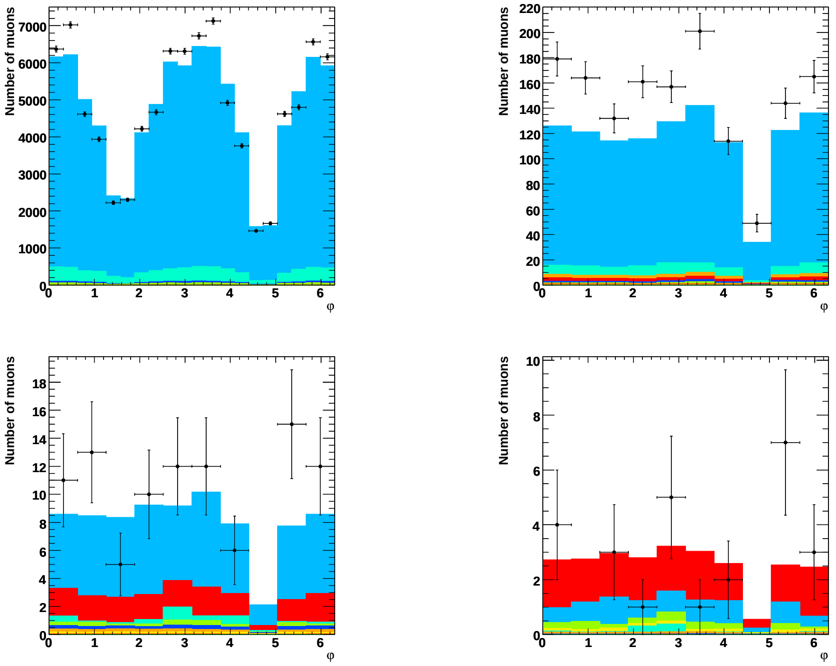

Figure D.11.: φ of the two muons.

E. Signal Fit Function (Dimuon Channel)

The fit function for the signal for the dimuon channel is shown on the following pages. All variables, rms, $mean$, and m_{top} are given in GeV. For each plot two of the variables were kept fixed and the distribution of the third variable was plotted. The dots with the errorbars represent the histogram coming from the weight functions. The black line represents the fitted function.

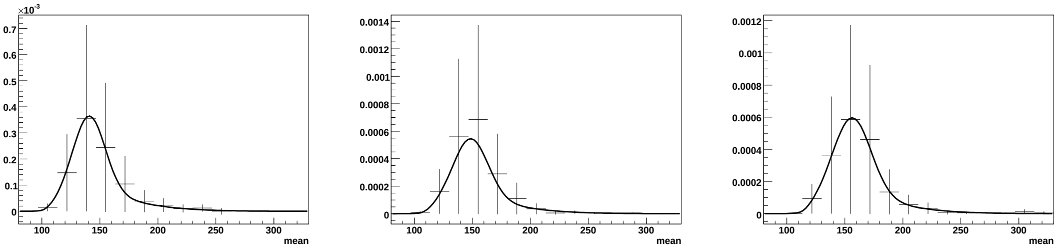

(a) $rms = 3$ GeV (b) $rms = 9$ GeV (c) $rms = 15$ GeV

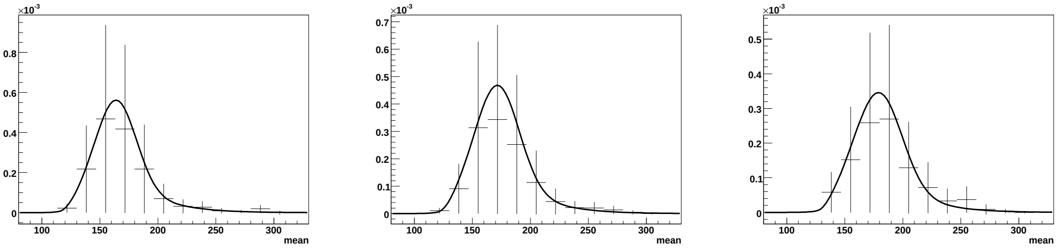

(d) $rms = 21$ GeV (e) $rms = 27$ GeV (f) $rms = 33$ GeV

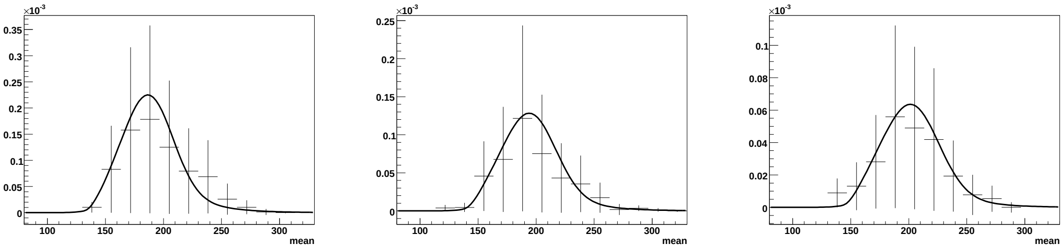

(g) $rms = 39$ GeV (h) $rms = 45$ GeV (i) $rms = 51$ GeV

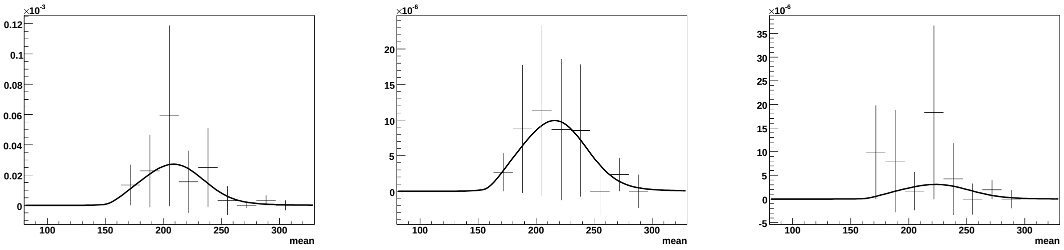

(j) $rms = 57$ GeV (k) $rms = 63$ GeV (l) $rms = 69$ GeV

Figure E.1.: Distribution of the mean of the weightfunctions for various rms-values and $m_{top} = 155$ GeV. The black line represents the fitted function.

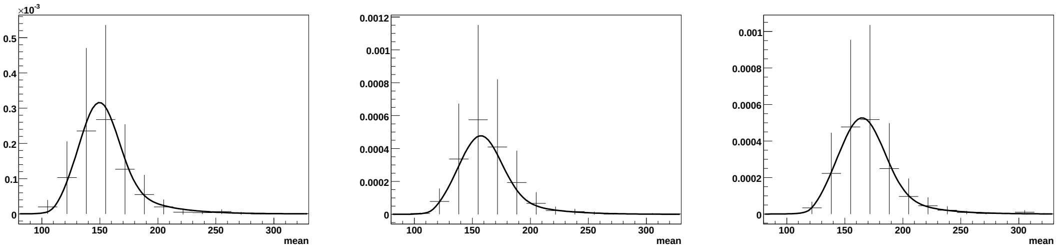

(a) $rms = 3$ GeV (b) $rms = 9$ GeV (c) $rms = 15$ GeV

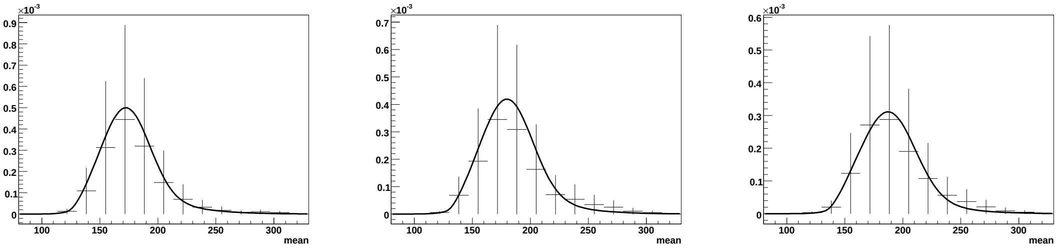

(d) $rms = 21$ GeV (e) $rms = 27$ GeV (f) $rms = 33$ GeV

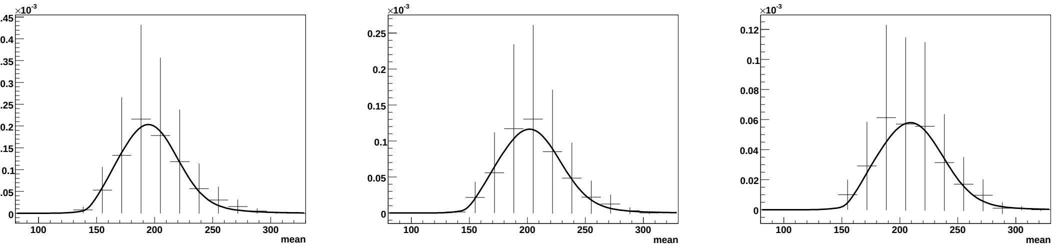

(g) $rms = 39$ GeV (h) $rms = 45$ GeV (i) $rms = 51$ GeV

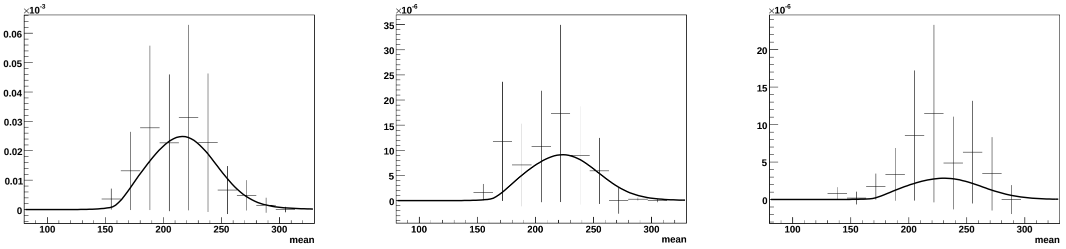

(j) $rms = 57$ GeV (k) $rms = 63$ GeV (l) $rms = 69$ GeV

Figure E.2.: Distribution of the mean of the weightfunctions for various rms-values and $m_{top} = 170$ GeV. The black line represents the fitted function.

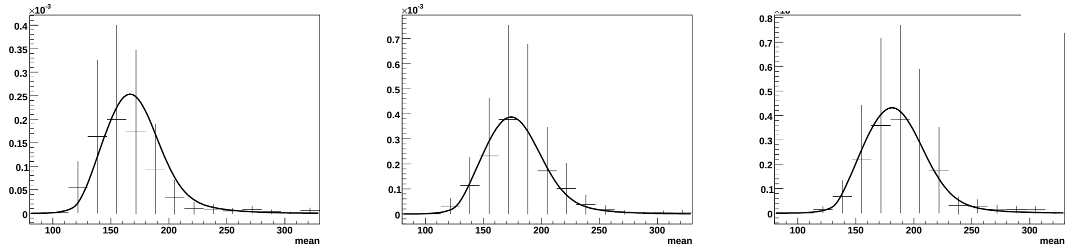

(a) $rms = 3$ GeV (b) $rms = 9$ GeV (c) $rms = 15$ GeV

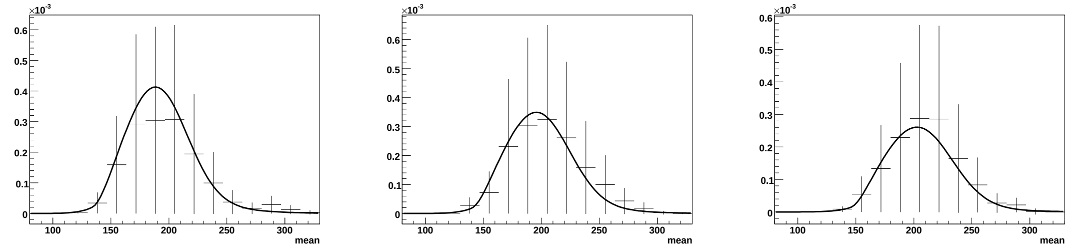

(d) $rms = 21$ GeV (e) $rms = 27$ GeV (f) $rms = 33$ GeV

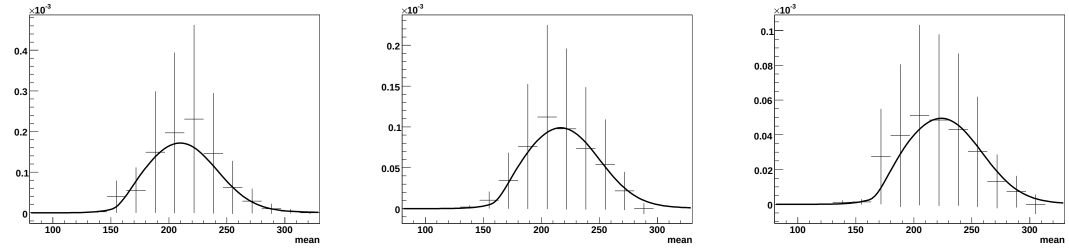

(g) $rms = 39$ GeV (h) $rms = 45$ GeV (i) $rms = 51$ GeV

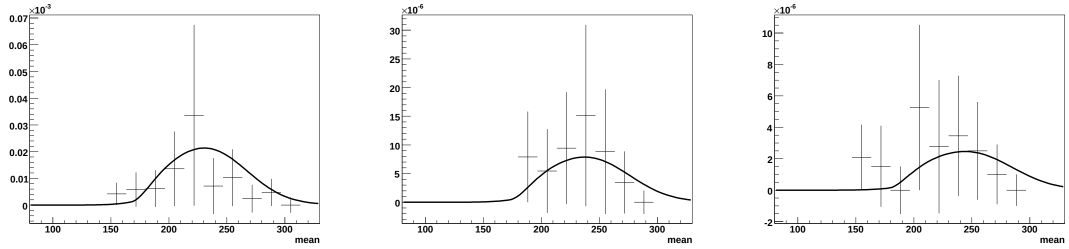

(j) $rms = 57$ GeV (k) $rms = 63$ GeV (l) $rms = 69$ GeV

Figure E.3.: Distribution of the mean of the weightfunctions for various rms-values and $m_{top} = 200$ GeV. The black line represents the fitted function.

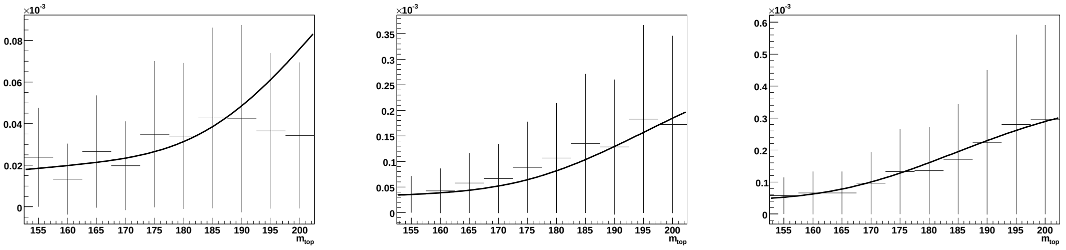

(a) $rms = 3$ GeV

(b) $rms = 9$ GeV

(c) $rms = 15$ GeV

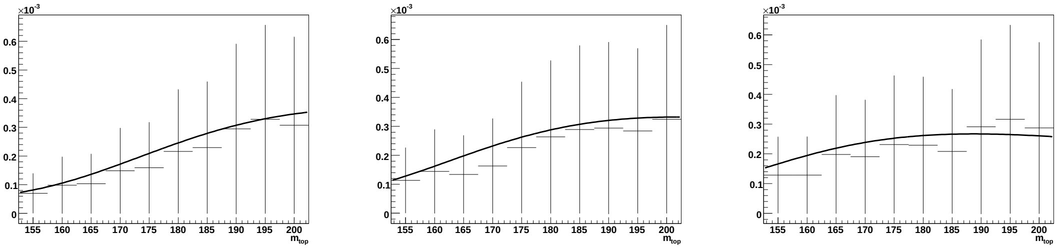

(d) $rms = 21$ GeV

(e) $rms = 27$ GeV

(f) $rms = 33$ GeV

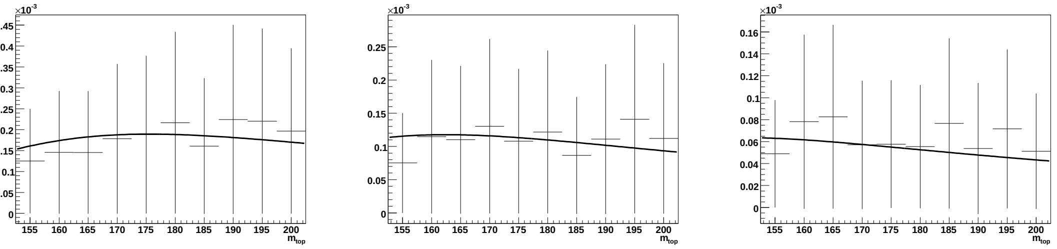

(g) $rms = 39$ GeV

(h) $rms = 45$ GeV

(i) $rms = 51$ GeV

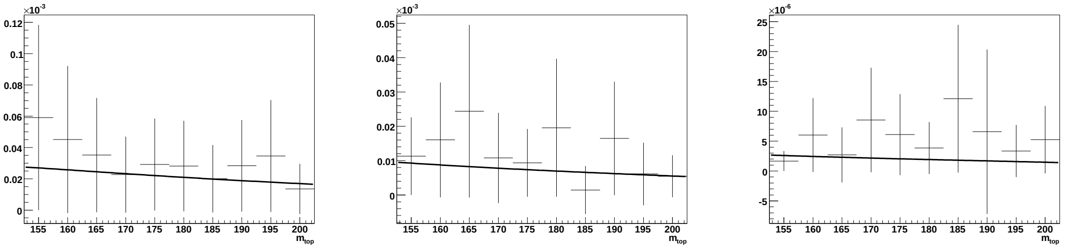

(j) $rms = 57$ GeV

(k) $rms = 63$ GeV

(l) $rms = 69$ GeV

Figure E.4.: Distribution of simulated top quark mass (m_{top}) of the weightfunctions for various rms-values and $mean = 125$ GeV. The black line represents the fitted function.

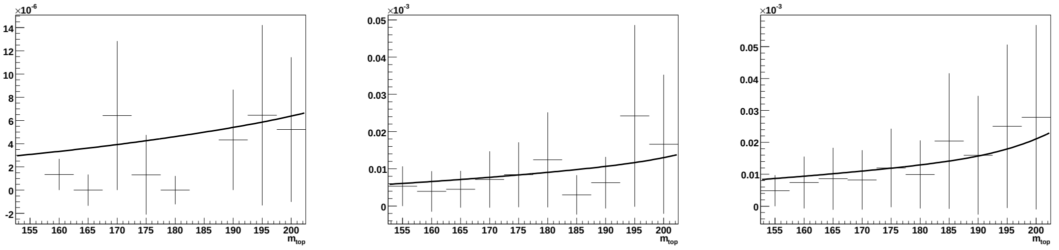

(a) $rms = 3$ GeV (b) $rms = 9$ GeV (c) $rms = 15$ GeV

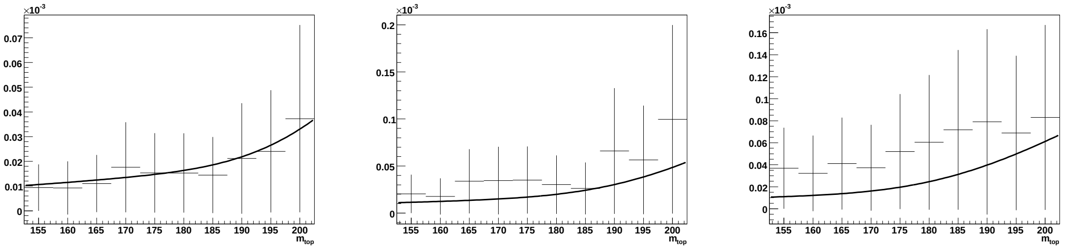

(d) $rms = 21$ GeV (e) $rms = 27$ GeV (f) $rms = 33$ GeV

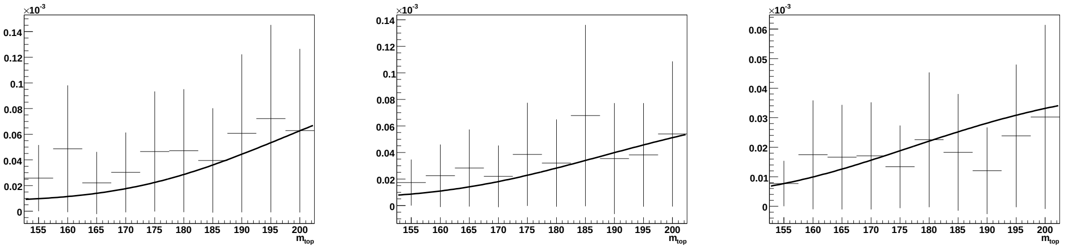

(g) $rms = 39$ GeV (h) $rms = 45$ GeV (i) $rms = 51$ GeV

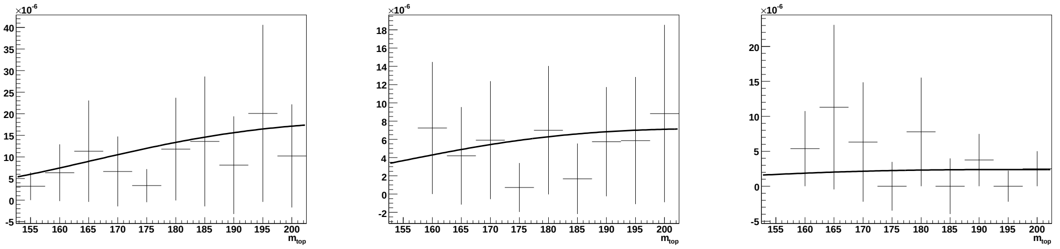

(j) $rms = 57$ GeV (k) $rms = 63$ GeV (l) $rms = 69$ GeV

Figure E.5.: Distribution of simulated top quark mass (m_{top}) of the weightfunctions for various rms-values and $mean = 175$ GeV. The black line represents the fitted function.

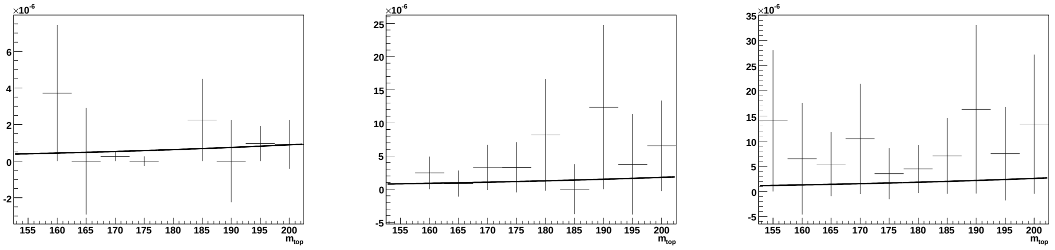

(a) $rms = 3$ GeV

(b) $rms = 9$ GeV

(c) $rms = 15$ GeV

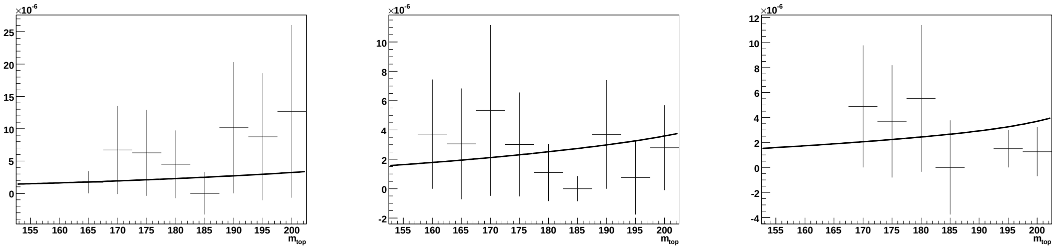

(d) $rms = 21$ GeV

(e) $rms = 27$ GeV

(f) $rms = 33$ GeV

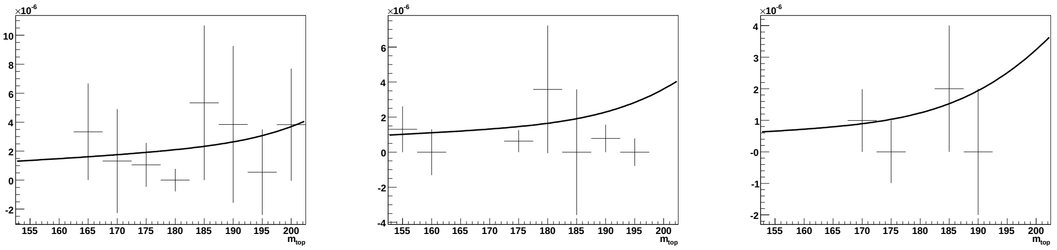

(g) $rms = 39$ GeV

(h) $rms = 45$ GeV

(i) $rms = 51$ GeV

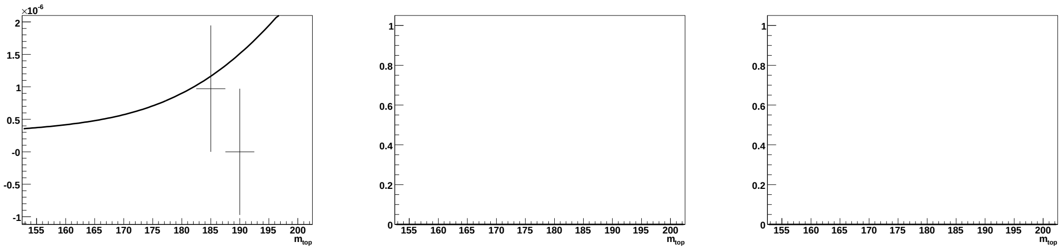

(j) $rms = 57$ GeV

(k) $rms = 63$ GeV

(l) $rms = 69$ GeV

Figure E.6.: Distribution of simulated top quark mass (m_{top}) of the weightfunctions for various rms-values and $mean = 225$ GeV. The black line represents the fitted function.

F. Signal Fit Function ($e\mu$ Channel)

The fit function for the signal for the $e\mu$ channel is shown on the following pages. All variables, rms, $mean$, and m_{top} are given in GeV. For each plot two of the variables were kept fixed and the distribution of the third variable was plotted. The dots with the errorbars represent the histogram coming from the weight functions. The black line represents the fitted function.

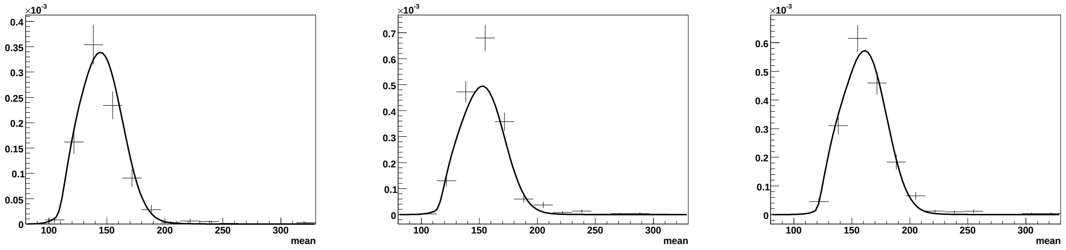

(a) $rms = 3$ GeV (b) $rms = 9$ GeV (c) $rms = 15$ GeV

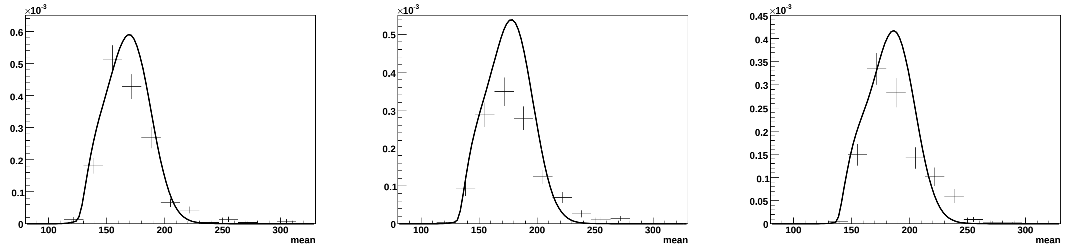

(d) $rms = 21$ GeV (e) $rms = 27$ GeV (f) $rms = 33$ GeV

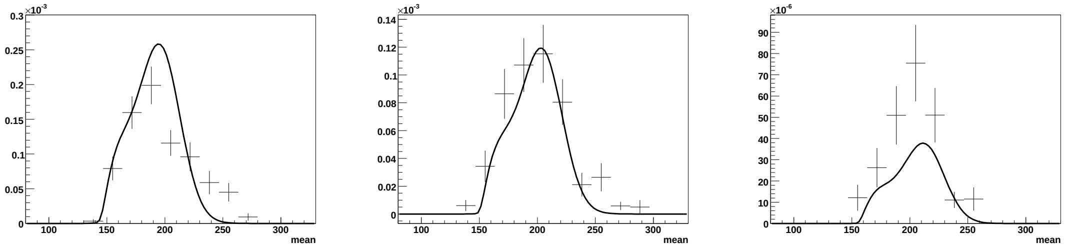

(g) $rms = 39$ GeV (h) $rms = 45$ GeV (i) $rms = 51$ GeV

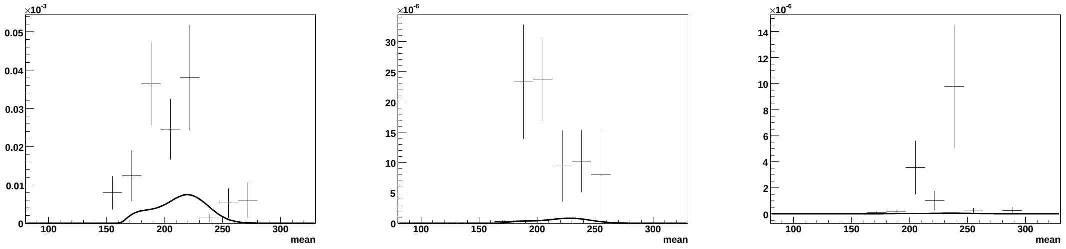

(j) $rms = 57$ GeV (k) $rms = 63$ GeV (l) $rms = 69$ GeV

Figure F.1.: Distribution of the mean of the weightfunctions for various rms-values and $m_{top} = 160$ GeV. The black line represents the fitted function.

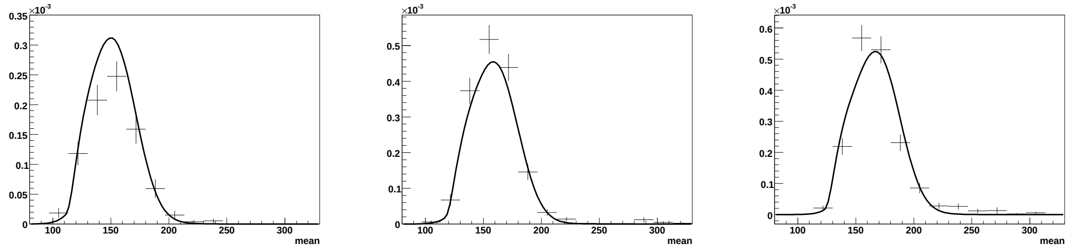

(a) $rms = 3$ GeV (b) $rms = 9$ GeV (c) $rms = 15$ GeV

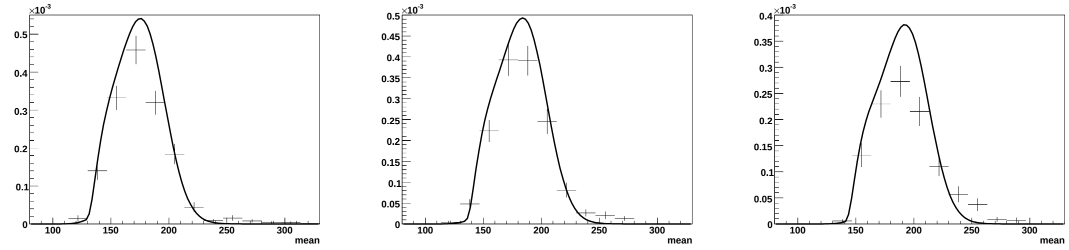

(d) $rms = 21$ GeV (e) $rms = 27$ GeV (f) $rms = 33$ GeV

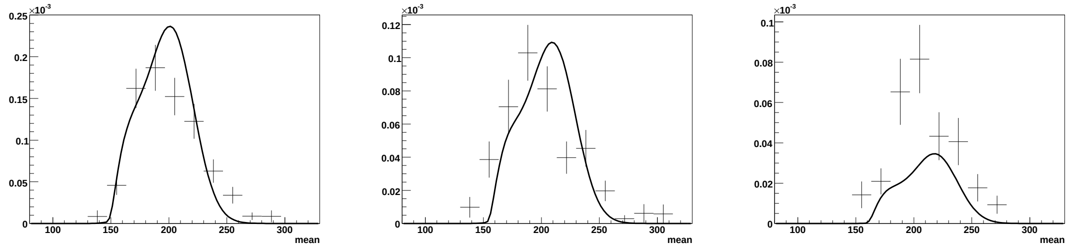

(g) $rms = 39$ GeV (h) $rms = 45$ GeV (i) $rms = 51$ GeV

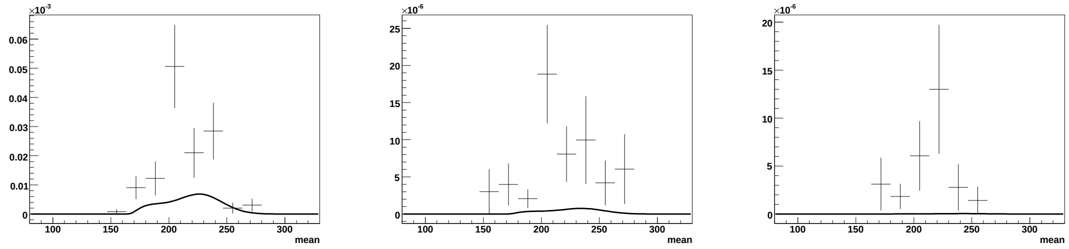

(j) $rms = 57$ GeV (k) $rms = 63$ GeV (l) $rms = 69$ GeV

Figure F.2.: Distribution of the mean of the weightfunctions for various rms-values and $m_{top} =$ 170 GeV. The black line represents the fitted function.

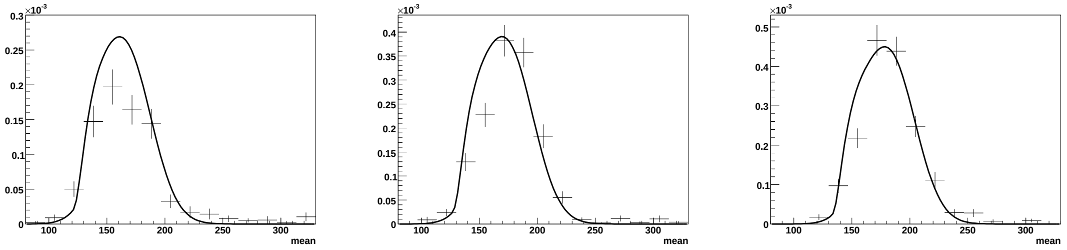

(a) $rms = 3$ GeV

(b) $rms = 9$ GeV

(c) $rms = 15$ GeV

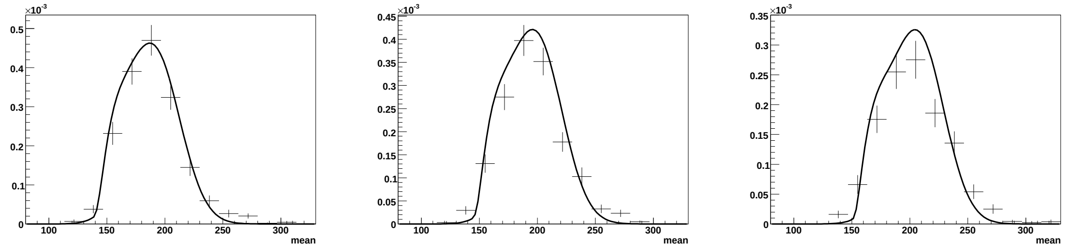

(d) $rms = 21$ GeV

(e) $rms = 27$ GeV

(f) $rms = 33$ GeV

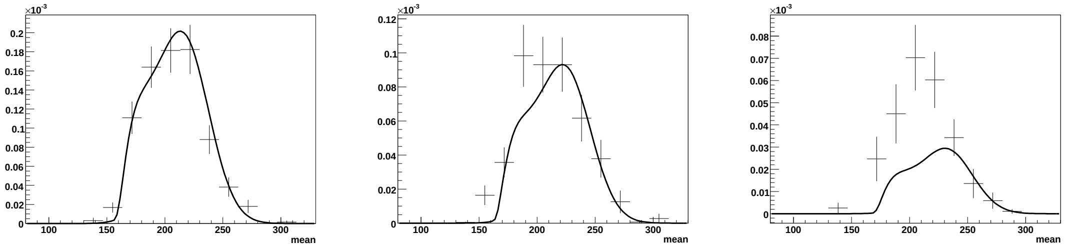

(g) $rms = 39$ GeV

(h) $rms = 45$ GeV

(i) $rms = 51$ GeV

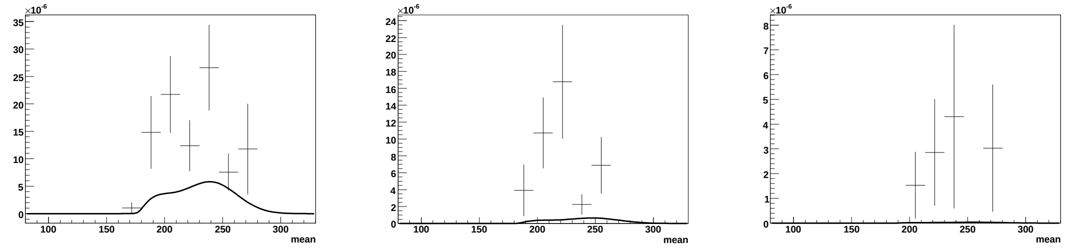

(j) $rms = 57$ GeV

(k) $rms = 63$ GeV

(l) $rms = 69$ GeV

Figure F.3.: Distribution of the mean of the weightfunctions for various rms-values and $m_{top} = 190$ GeV. The black line represents the fitted function.

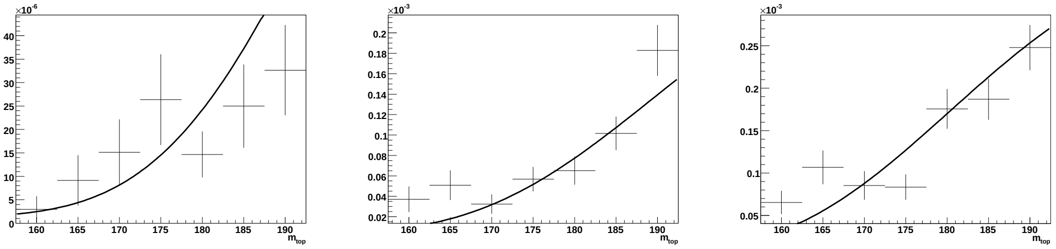

(a) $rms = 3$ GeV

(b) $rms = 9$ GeV

(c) $rms = 15$ GeV

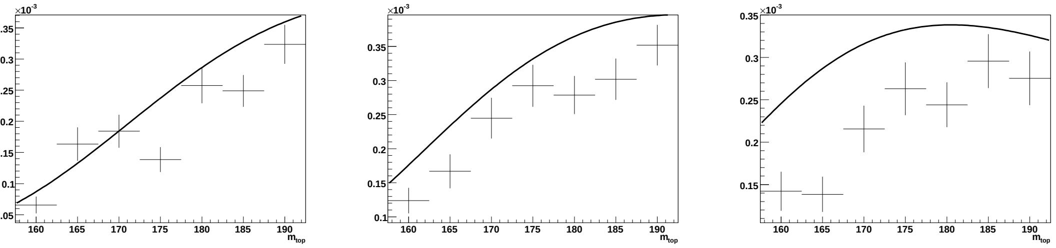

(d) $rms = 21$ GeV

(e) $rms = 27$ GeV

(f) $rms = 33$ GeV

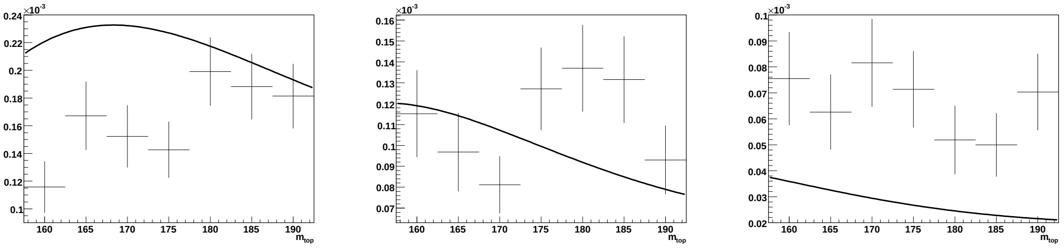

(g) $rms = 39$ GeV

(h) $rms = 45$ GeV

(i) $rms = 51$ GeV

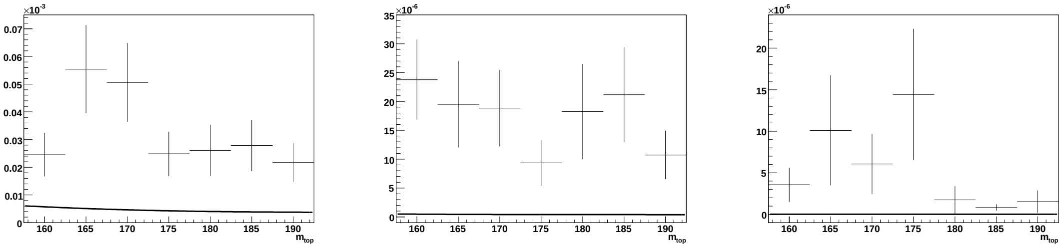

(j) $rms = 57$ GeV

(k) $rms = 63$ GeV

(l) $rms = 69$ GeV

Figure F.4.: Distribution of simulated top quark mass (m_{top}) of the weightfunctions for various rms-values and $mean = 125$ GeV. The black line represents the fitted function.

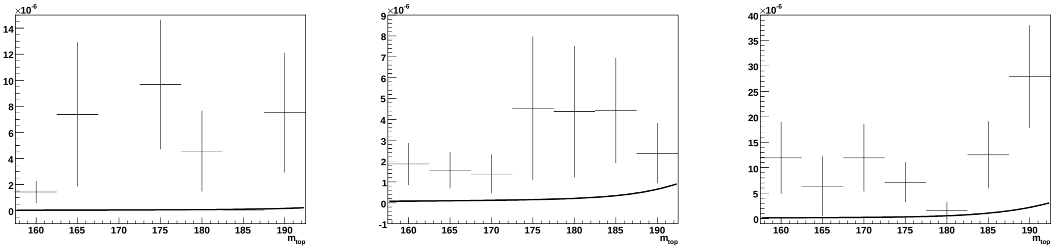

(a) $rms = 3$ GeV

(b) $rms = 9$ GeV

(c) $rms = 15$ GeV

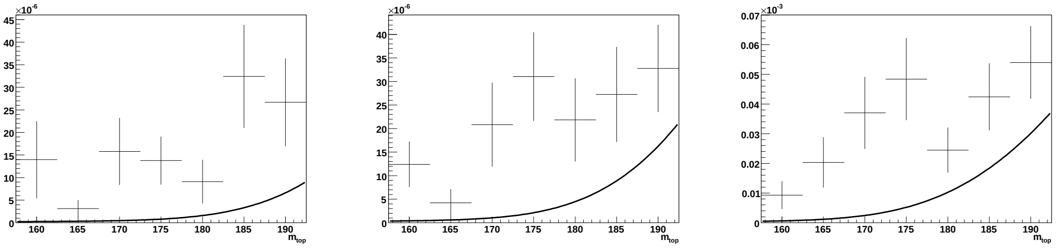

(d) $rms = 21$ GeV

(e) $rms = 27$ GeV

(f) $rms = 33$ GeV

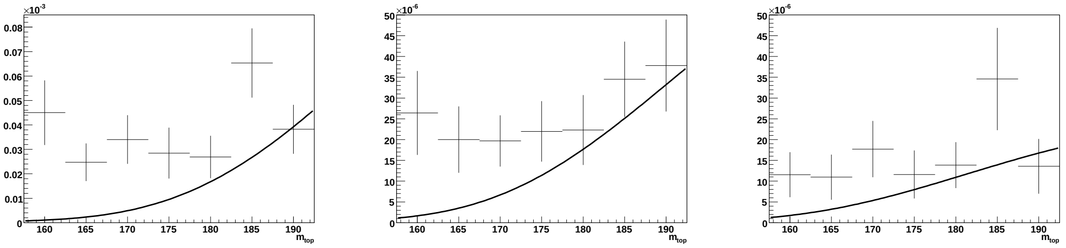

(g) $rms = 39$ GeV

(h) $rms = 45$ GeV

(i) $rms = 51$ GeV

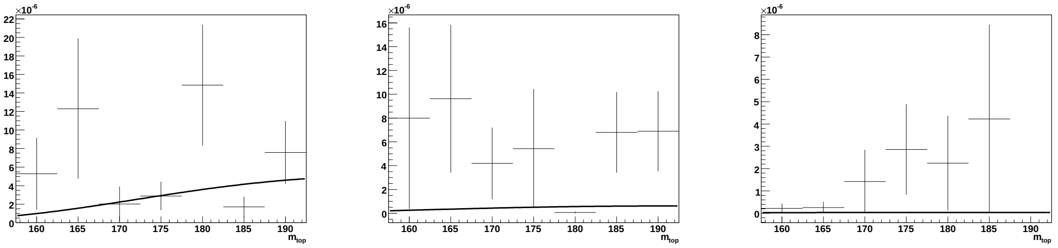

(j) $rms = 57$ GeV

(k) $rms = 63$ GeV

(l) $rms = 69$ GeV

Figure F.5.: Distribution of simulated top quark mass (m_{top}) of the weightfunctions for various rms-values and $mean = 175$ GeV. The black line represents the fitted function.

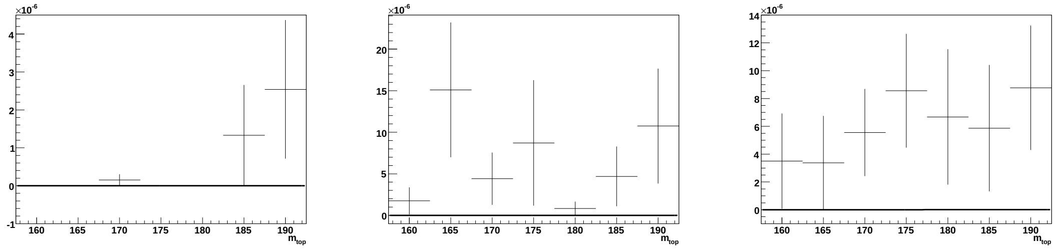

(a) $rms = 3$ GeV (b) $rms = 9$ GeV (c) $rms = 15$ GeV

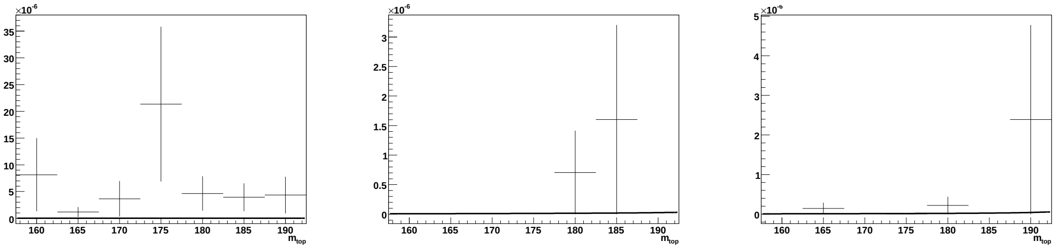

(d) $rms = 21$ GeV (e) $rms = 27$ GeV (f) $rms = 33$ GeV

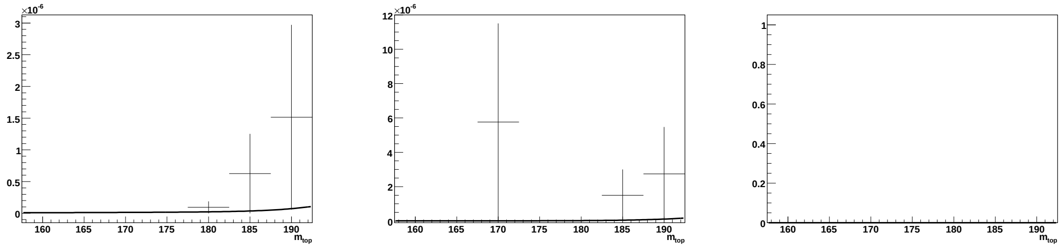

(g) $rms = 39$ GeV (h) $rms = 45$ GeV (i) $rms = 51$ GeV

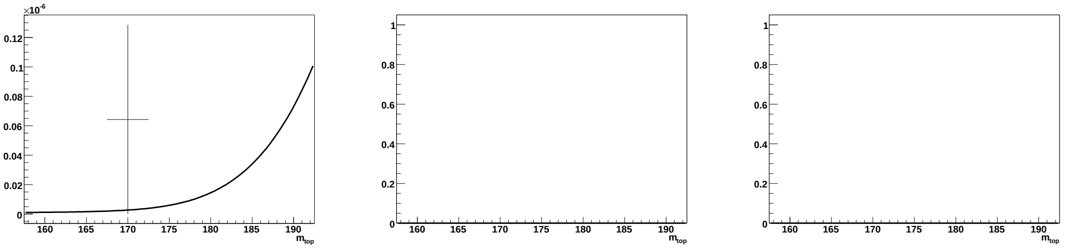

(j) $rms = 57$ GeV (k) $rms = 63$ GeV (l) $rms = 69$ GeV

Figure F.6.: Distribution of simulated top quark mass (m_{top}) of the weightfunctions for various rms-values and $mean = 225$ GeV. The black line represents the fitted function.

Bibliography

[1] C. Berger, *Elementarteilchenphysik - Von den Grundlagen zu den modernen Experimenten*, 2nd edn., (2006).

[2] S. L. Glashow, *Partial Symmetries of Weak Interactions*, Nucl. Phys. **22** (1961) 579.

[3] S. Weinberg, *A Model of Leptons*, Phys. Rev. Lett. **19** (1967) 1264.

[4] A. Salam, *Elementary Particle Physics*, N. Svartholm, ed., Nobel Symposium No. 8, Almqvist & Wiksell, Stockholm.

[5] Particle Data Group, *Summary Tables of Particle Properties*, Phys. Lett. **B667** (2008), `http://pdg.lbl.gov`.

[6] P. W. Higgs, *Broken Symmetries, Massless Particles and Gauge Fields*, Phys. Lett. **12** (1964) 132.

[7] F. Englert and R. Brout, *Broken Symmetry and the Mass of Gauge Vector Mesons*, Phys. Rev. Lett. **13** (1964) 321.

[8] S. Martin, *A Supersymmetry Primer*, `hep-ph/9709356`.

[9] D. Gladyshev and D. Kazakov, *Supersymmetry and LHC*, `hep-ex/0606288v1`.

[10] CDF Collaboration, *Observation of Top Quark Production in $p\bar{p}$ Collisions with the Collider Detector at Fermilab*, Phys. Rev. Lett. **74** (1995) 2626.

[11] DØ Collaboration, *Observation of the Top Quark*, Phys. Rev. Lett. **74** (1995) 2632.

[12] The Tevatron Electroweak Working Group, *Combination of CDF and DØ Results on the Mass of the Top Quark*, FERMILAB -TM -2413 -E (2008), `arXiv:0808.1089v1[hep-ex]`.

[13] Particle Data Group, *The Top Quark*, Phys. Lett. **B667** (2008), `http://pdg.lbl.gov`.

[14] N. Kidonakis and R. Vogt, *Next-to-next-to-leading Order Soft-gluon Corrections in Top Quark Hadron Production*, Phys. Rev. D **68** (2003) 114014.

[15] DØ Collaboration, *Measurement of the $t\bar{t}$ Production Cross Section in $p\bar{p}$ Collisions at $\sqrt{s} = 1.96\ TeV$*, Phys. Rev. Lett. **100** (2008) 192004.

[16] C. Cortese and R. Petronzio, *The Single Top Production Channel at Tevatron Energies*, Phys. Lett. B **253** (1991) 494.

[17] DØ Collaboration, *Evidence for Production of Single Top Quarks*, Phys. Rev. D **78** (2008) 012005.

[18] N. Kidonakis, *Single Top Quark Production at the Tevatron: Threshold Resummation and Finit-order Soft Gluon Corrections*, Phys. Rev. D **74** (2006) 114012, `hep-ph/0609287v3`.

[19] DØ Collaboration, *Spin Correlation in $t\bar{t}$ Production from $p\bar{p}$ Collisions at* $\sqrt{s} = 1.8$ *TeV.*, Phys. Rev. Lett. **85** (2000) 256.

[20] Particle Data Group, *The CKM Quark Mixing Matrix*, Phys. Lett. **B667** (2008), `http://pdg.lbl.gov`.

[21] The ALEPH, DELPHI, L3, OPAL and SLD Collaborations, the LEP-Electroweak Working Group, the SLD Electroweak and Heavy Flavour Groups, *A Combination of Preliminary Electroweak Measurements and Constraints on the Standard Model*, updated for the Winter 2007 conferences, `http://www.cern.ch/LEPEWWG` (2008).

[22] `www-d0.fnal.gov/pub/about/whatis/history.html`.

[23] `www-d0.fnal.gov/pub/about/whatis/timeline.html`.

[24] `www-d0.fnal.gov/pub/inquiring/physics/accelerators/chainaccel.html`.

[25] DØ Collaboration, *The Upgraded DØ Detector*, Nucl. Instr. and Methods **A565** (2006) 463.

[26] DØ Collaboration, *The DØ Detector*, Nucl. Instr. and Methods **A338** (1994) 185.

[27] *DØ Layer 0 Conceptual Design Report*, `http://d0server1.fnal.gov/projects/run2b/Meetings/PMGs/Nov03/D0_L0_CDR_%v2.6.pdf`.

[28] D. Tsybychev, *Status and Performance of the new Layer of Silicon Detector at DØ*, Nucl. Instr. and Methods **A582-3** (2007) 701.

[29] M. Abolins et al., *The Run IIb Trigger Upgrade for the DØ Experiment.*, IEEE Trans. of Nucl. Sci. **51** (2004) 340.

[30] Common Samples Group, `http://www-d0.fnal.gov/Run2Physics/cs`.

[31] A. Harel, *Jet ID Optimization*, DØ Note 4919 (2005).

[32] E. Busato and B. Andrieu, *Jet Algorithms in the DØ Run II Software: Description and User's Guide*, DØ Note 4457 (2004).

[33] O. Atramentov et al, *Electron and Photon Identification with p20 Data*, DØ Note 5761 (2008).

[34] M. Aoki, *Electron Likelihood in p20*, DØ Note 5675 (2008).

[35] P. Calfayan, *Muon Identification Certification for p17 data*, DØ Note 4487 (2004).

[36] S. Trincaz-Duvoid and P. Verdier, *Missing* E_T *Reconstruction in p17*, DØ Note 4474 (2004).

[37] M. L. Mangano, F. Piccinini, and A. D. Polosa, *ALPGEN, a Generator for Hard Multiparton Processes in Hadronic Collisions*, JHEP **0307** (2003), `hep-ex/0206293v2`.

[38] T. Sjöstrand, S. Mrenna, and P. Skands, *Pythia 6.4 - Physics and Manual*, JHEP **0605** (2006) 026, `hep-ph/0603175`.

[39] M. L. Mangano, M. Moretti, F. Piccinini, R. Pittau, and A. D. Polosa, *ALPGEN, a Generator for Hard Multiparton Processes in Hadronic Collisions*, JHEP **07** (2003) 001, `hep-ph/0206293`.

[40] M. L. Mangano and others, *Multijet Matrix Elements and Shower Evolution in Hadronic Collisions: W b bbar + n Jets as a Case Study*, Nucl. Phys. B **632** (2002) 343, `hep-ph/0108069`.

[41] J. Pumplin et al., *New Generation of Parton Distributions with Uncertainties from Global QCD Analysis*, JHEP **0207** (2002) 012.

[42] R. Brun and others, *GEANT - Detector Description and Simulation Tool*, CERN Program Library Vers. 3.21 **W5013** (1993).

[43] Y. Fisyak and J. Womersley, *D0gstar D0 GEANT Simulation of the Total Apparatus Response*, DØ Note 3191 (April 1997).

[44] F. Déliot, V. Sharyy, M. Besançon, M. Arthaud, and S. Chakrabarti, *Latest p20 Electron Muon Selection Results*, Talk at DØ Double Top Meeting, June 19th, 2008.

[45] U. Bassler, J. Konrath, Y. Peters, C. Schwanenberger, and E. Shabalina, *Measurement of the* $t\bar{t}$ *Production Cross Section at* $\sqrt{(}s) = 1.96$ *TeV in the Dimuon Final State using p17 Dataset*, DØ Note 5581 (2008).

[46] P. Calfayan, *Combination of Single Muon Triggers in p17 Data by using an inclusive OR*, DØ Note 5329 (2008).

[47] N. Makovec and J.-F. Grivaz, *Shifting, Smearing and Removing Simulated Jets*, DØ Note 4919 (2005).

[48] A. Schwartzman, $\not{E}_T$ *Significance Algorithm in Run II Data*, DØ Note 4254 (2003).

[49] Trigger Meister Webpage, `http://www-d0.fnal.gov/trigger_meister/private/www/tl_desc/global.html`.

[50] B. Martin, Y. Arnoud, G. Sajot, and E. Shabalina, *Measurement of the* $t\bar{t}$ *Production Cross Section at* $\sqrt{s} = 1.96$ *TeV in the ee Final State using p17 Dataset*, DØ Note 5386 (2007).

[51] P. Calfayan et al., *Muon Identification Certification for p17 Data*, DØ Note 5157 (2006).

[52] J. Kvita and A. Harel, *Jet ID Efficiencies and Scale Factors*, DØ Note 5634 (2008).

[53] JES Group, *Jet Energy Scale Determination at DØ Run II final p17 version*, DØ Note 5382 (2007).

[54] G. Golovanov, U. Heintz, S. Jabeen, and A. Kupco, *Preliminary Jet Energy Scale Calibration for Run IIb Data*, DØ Note 5555 (2007).

[55] M. Arthaud, M. Besançon, S. Chakrabarti, F. Déliot, and V. Sharyy, $t\bar{t}$ *Event Selection in the Electron Muon Final State using p20 Dataset*, DØ Note 5720 (2008).

[56] DØ Collaboration, *Measurement of the Top Quark Mass Using Dilepton Events*, Phys. Rev. Lett. **80** (1998) 2063.

[57] O. Brandt, *Measurement of the Mass of the Top Quark in Dilepton Final States with the DØ-Detector*, diploma thesis, University of Bonn, (2006), FERMILAB-MASTERS-2006-03.

[58] DØ Collaboration, *Measurement of* m_{top} *in* $e\mu$ *Events with Neutrino Weighting in Run II at DØ*, DØ Note 5171 (2006).

[59] J. Meyer, *Measurement of the Top Quark Mass using Dilepton Events and a Neutrino Weighting Algorithm with the DØ Experiment at the Tevatron (Run II)*, Ph.D. thesis, University of Bonn, (2007), FERMILAB-THESIS-2007-65.

[60] DØ Collaboration, *Measurement of Top Quark Mass in Dilepton Final States via Neutrino Weighting*, DØ Note 5746 (2008).

Acknowledgements

First of all I would like to thank Arnulf Quadt and Dmitri Denisov for making this thesis possible and for arranging the possibility to spend some time at Fermilab. All in all I had a great time.

Also I would like to thank Elizaveta Shabalina and Christian Schwanenberger for being good supervisors at Fermilab and Jörg Meyer and Su-Jung Park for being my supervisors in Göttingen.

Thanks to Frédéric Déliot, Slava Sharyy and Mike Kirby for helping with the dimuon selection for the Run IIb dataset. Especially Frédéric and Slava really spent a lot of time on that. And additional thanks to Frédéric for producing text files for the neutrino weighting. Also thanks to Jens-Peter Konrath for helping to get the dimuon selection for the Run IIa dataset running.

I would like to thank Yvonne Peters, Alexander Grohsjean and Björn Penning for answering questions. Furthermore I would like to thank Liang Li for patiently answering questions and Jochen Cammin for helping with Latex. For discussions outside normal work hours I would like to thank Sohrab Hossain.

I also want to thank Antje Krüger for reading this thesis so that I had an opinion of someone who is not a particle physicist, and for being a good friend all these years I spent in Göttingen. Mohsen Alizadeh for asking interesting (and sometimes stupid) questions and also for being a good friend.

I would also like to thank Bill Lee, Sehwook Lee and Emanuel Strauss for teaching me everything I needed for DAQ shifts. At this point thanks to Geoff Savage for being the best shift captain I had during all this time. It was a lot of fun being on shift with him.

And thanks to Alison and John for listening and for sight-seeing tours at Fermilab.

For some nice times in Chicago (without thinking about physics) I would like to thank Xuebing Bu, Mario Vaz, Steve Thile and his mother.

Of course I also want to thank my family. Especially my parents and my sister Dina. At this point I would also like to thank my grandaunt, Ma Klasing, for filling the role of a great grandmother, at least for me.

Thanks to most of the guys who are/were living at Dorm 4 for having fun on several occasions. They are just too many to mention individually.

And there are so many others I could name: Sonya Wright, Enrique, Barb Book, Melissa Clayton Lang, Sudhir Malik. I am sure I forgot a lot of people. So thanks to all of them.